Gottfried Wilhelm Leibniz Universität Hannover

Albert-Einstein-Institut

Max-Planck-Institut für Gravitationsphysik

Laser Power Stabilization
for the AEI 10 m Prototype

Master thesis by Jonas Junker

Hannover, May 10, 2016

1$^{\text{st}}$ Examiner: Apl. Prof. Dr. Benno Willke

2$^{\text{nd}}$ Examiner: Prof. Dr. Karsten Danzmann

Supervisor: Patrick Oppermann

Abstract

In gravitational wave detectors, laser power noise can mask potential gravitational wave signals, making them impossible to detect. The solution is a laser power stabilization. In general, noise can be grouped into two categories: technical noise and quantum noise. Technical noise sources can originate e.g. from fluctuations of the pump current of a laser or from changes in temperature in the laser crystal. In contrast, quantum noise is a fundamental effect due to the quantum behavior of elementary particles like electrons or photons.

Currently a 10 m long Michelson interferometer is set up at the Albert Einstein Institute in Hannover that is designed to reach the standard quantum limit (SQL) of interferometry. The SQL is a limit of measurement accuracy in an interferometer consisting of two quantum noise sources, the photon shot noise and the radiation pressure noise. The experiment is located in a vacuum system to provide an undisturbed environment. 35 W of laser light at a wavelength of 1064 nm are coupled into the system via a photonic crystal fiber.

Within the scope of this thesis, a shot noise limited laser power stabilization was developed in a preparation experiment and then implemented in the AEI 10 m Prototype. The realization was executed with an active feedback control loop that suppresses all technical noise sources below the quantum noise in a frequency band between 200 Hz and 1 kHz. The actuation on the light field is realized with an acousto-optic modulator to compensate the power noise. The sensor consists of a photodiode array comprising four in-loop and four out-of-loop photodiodes. This configuration allows the detection of several hundred milliwatt of light power without introducing thermal coupling to power noise. To monitor the pointing of the laser beam, two quadrant photodiodes are installed.

In a table top experiment, a power of 159 mW was detected on the in-loop sensor and 141 mW was measured on the out-of-loop sensor. The relative power noise was shot noise limited between 600 Hz and 1.5 kHz, and accounts to $2.7 \times 10^{-9}\,\mathrm{Hz}^{-1/2}$. At the AEI 10 m Prototype the power on the in-loop sensor was 146 mW, and on the out-of-loop it was 163 mW. From 200 Hz to 1 kHz the relative power noise was shot noise limited at a level of $2.6 \times 10^{-9}\,\mathrm{Hz}^{-1/2}$.

Key words: laser power stabilization, shot noise, standard quantum limit

Kurzfassung

In Gravitationswellendetektoren kann Laserleistungsrauschen mögliche Signale von Gravitationswellen verbergen, sodass diese nicht detektiert werden können. Die Lösung dieses Problems ist eine Stabilisierung der Laserleistung. Im Allgemeinen kann Rauschen in zwei Kategorien unterteilt werden: technisches Rauschen und Quantenrauschen. Technische Rauschquellen können zum Beispiel von Schwankungen des Diodenstroms oder von Temperaturveränderungen im Laserkristall stammen. Im Vergleich dazu ist Quantenrauschen ein grundsätzlich auftretendes Phänomen. Es entsteht aufgrund des Quantencharakters von Elementarteilchen wie Elektronen oder Photonen.

Zurzeit wird am Albert-Einstein-Institut in Hannover ein 10 m langes Michelson-Interferometer aufgebaut, um das Standard-Quantenlimit (SQL) der Interferometrie zu erreichen. Das SQL ist eine Grenze der Messgenauigkeit in einem Interferometer, welche sich aus dem Quantenrauschen und dem Strahlungsdruckrauschen zusammensetzt. Das Experiment befindet sich in einem Vakuumsystem, um eine ungestörte Umgebung zu erzeugen. Das Laserlicht hat eine Leistung von 35 W und eine Wellenlänge von 1064 nm. Es wird mit einer photonischen Kristallfaser in das Vakuumsystem eingekoppelt.

Im Rahmen dieser Arbeit wurde in einem Vorbereitungsexperiment eine Laserleistungsstabilisierung entwickelt, die nur durch Quantenrauschen limitiert ist. Anschließend wurde diese in den AEI 10 m Prototypen implementiert. Die Realisierung wurde mit einem aktiven Regelkreis erreicht, der alle technischen Rauschquellen in einem Frequenzband von 200 Hz bis 1 kHz unter das Quantenrauschen reduziert. Um das Rauschen zu kompensieren, wird das Lichtfeld mit einem akustooptischen Modulator reguliert. Ein Photodioden-Array mit vier in-loop und vier out-of-loop Photodioden bildet den Sensor. Mit dieser Konfiguration ist es möglich, mehrere hundert Milliwatt an Strahlungsleistung zu detektieren, ohne zusätzliches Leistungsrauschen durch thermische Kopplung zu bekommen. Um das Pointing des Laserstrahls zu beobachten sind zwei Quadrantenphotodioden installiert.

In einem Vorbereitungsexperiment wurde eine Leistung von 159 mW auf dem in-loop Sensor detektiert und auf dem out-of-loop Sensor wurden 141 mW gemessen. In den Frequenzen zwischen 600 Hz und 1,5 kHz war das relative Leistungsrauschen durch Quantenrauschen limitiert und ergibt sich zu $2{,}7 \cdot 10^{-9}\,\mathrm{Hz}^{-1/2}$. Beim AEI 10 m Prototypen betrug die Leistung auf dem in-loop Sensor 146 mW und auf dem out-of-loop Sensor 163 mW. Dort war das relative Leistungsrauschen auf einem Frequenzband von 200 Hz bis 1 kHz durch Quantenrauschen limitiert und hatte einen Wert von $2{,}6 \cdot 10^{-9}\,\mathrm{Hz}^{-1/2}$.

Schlagwörter: Laserleistungsstabilisierung, Schrotrauschen, Standard-Quantenlimit

Contents

Acronyms

ADC	analog-to-digital conversion
AEI	Albert Einstein Institute
aLIGO	Advanced LIGO
AOM	acousto-optic modulator
BS	beam splitter
CDS	control and data system
DAC	digital-to-analog conversion
DCC	Document Control Center
EOAM	electro-optic amplitude modulator
EOM	electro-optic modulator
EPICS	Experimental Physics and Industrial Control System
ET	Einstein Telescope
FCS	feedback control system
GAS	geometric anti-spring
GPS	Global Positioning System
il	in-loop
InGaAs	indium gallium arsenide
IP	inverted pendulum
LIGO	Laser Interferometer Gravitational-Wave Observatory
LISA	Laser Interferometer Space Antenna
NPRO	nonplanar ring oscillator
ool	out-of-loop

PBS	polarizing beam splitter
PCF	photonic crystal fiber
PD	photodiode
PDH	Pound–Drever–Hall
PI controller	proportional-integral controller
PMC	pre-mode cleaner
PSD	power spectral density
QPD	quadrant photodiode
RF	radio frequency
RIN	relative intensity noise
RPN	relative power noise
SAS	seismic attenuation system
SOA	semiconductor optical amplifier
SPI	suspension platform interferometer
SQL	standard quantum limit
TIA	transimpedance amplifier

CHAPTER 1

Introduction

In the end of the 19th century, it was assumed that light requires a medium for propagation. This medium was called the luminiferous ether [Bre77]. To consider the effect of this ether, Albert A. Michelson built an experiment containing an interferometer in 1881, which was later known as the Michelson interferometer [Mic81]. He split light into two directions that were perpendicular to each other, and after a constant distance the light was reflected back. Then he let both beams interfere and observed the resulting pattern. He stated that if the theory of the ether was valid, the light that was propagating in parallel to the direction of the earth motion should be influenced in its velocity. By rotating the whole setup the interference pattern should change. Since the results of this measurement were prone to experimental error, he decided to set up an improved experiment with a significantly increased accuracy with Edward W. Morley six years later: the so-called Michelson–Morley experiment [Mic87]. The outcome was as unambiguous as it was surprising: The experiment failed to validate the existence of the ether. However, the two physicists had shown experimentally that the speed of light is constant independent of the motion of the source or the observer. Furthermore, they had developed a very precise instrument to measure tiny length changes that is still used today.

In the beginning of the next century, in 1905, Albert Einstein published the results of his first theoretical considerations on the special theory of relativity [Ein05b]. This work did not only contradict the theory of the ether, but also postulated two principles: the principle of relativity and the constant speed of light in all inertial frames with uniform motion. Furthermore, this work implied the equivalence of mass and energy [Ein05a]. Eleven years later, Einstein formulated the first version of the general theory of relativity [Ein16], which can be understood as an extension of the special theory of relativity. For instance, in this new work he postulated ripples in the metric of space-time that are traveling with the speed of light, called gravitational waves. This was a fundamental difference to the previous understanding of gravitation, which was expected as an instantaneous interaction based on Isaac Newton's law of universal gravitation [New87]. According to Einstein, gravitational waves do not have any interaction with matter, they only change the metric of space-time periodically and locally. Gravitational waves arise from accelerated masses, like two neutron stars orbiting each other. In fact, the amplitude of these quadrupole waves

is very small corresponding to a relative change in length that is about a thousandth of the diameter of a proton on the earth. Thus, Einstein himself believed that their detection was practically impossible.

Einstein also postulated the stimulated emission of light by an atomic transition [Ein17], and thereby laid the theoretical foundation of a laser. In 1927 Hans Kopfermann and Rudolf Ladenburg succeeded in the first experimental verification of stimulated emission [Kop28]. More than a quarter of a century later, in 1960, the first ruby laser was developed by Theodore H. Maiman [Mai60], which revolutionized metrology. Laser light is characterized by a monochromatic collimated light beam that allows measurements with unprecedented accuracy. With this new innovation, the idea to detect gravitational waves with the aid of a laser source was quickly born. The concept of gravitational wave detectors based on laser interferometry was first suggested by Mikhail Gertsenshtein and Vladislav Pustovoit in 1962 [Ger62] and by Graham E. Moss, Lawrence R. Miller, and Robert L. Forward in 1971 [Mos71].

In 1983 one of the first prototype interferometers with an arm length of 30 m was set up in Garching. In this experiment the origin, action and magnitude of possible noise sources were considered [Sho88]. Furthermore, initial techniques of "recycling" the light to increase the available light power were realized [Mai87]. During this time, it was proposed to build up larger scale gravitational wave detectors. It took around twenty years until a set of the first initial ground-based gravitational wave detectors based on the technique of Michelson and Morley were finished by a large network of institutions and researchers. This network includes the detectors TAMA 300 in Japan [And01], GEO 600 in Germany [Wil02], Laser Interferometer Gravitational-Wave Observatory (LIGO) [Abr92] in the United States and Virgo in Italy [Ace08]. Their first observation cycle ran from 2002 to 2011. During this time, these so-called first generation gravitational wave detectors could mostly achieve their design sensitivity. Nevertheless, a gravitational wave was not detected until that point and so the construction of second generation gravitational wave detectors with improved sensitivity began. These are using new techniques to generate a ten times higher sensitivity than before. Notably, one of the key technologies is the usage of a new laser system with higher light power to decrease the effect of shot noise and to reach a high signal-to-noise ratio. Furthermore, these laser systems have to run very stably in almost all beam parameters, for example in the laser's amplitude. If the amplitude fluctuates on a significant scale, this noise can mask potential gravitational wave signals, which is the reason for a necessary power stabilization.

Over the intervening years, several prototype interferometers were employed to test and to develop further techniques. One of these is the AEI 10 m Prototype that is currently being set up at the Max Planck Institute for Gravitational Physics (Albert Einstein Institute) [Wes12]. This experiment primarily focuses on reaching the standard quantum limit of interferometry, a limit of measurement accuracy in an interferometer due to quantum noise effects.

In 2015 the second generation gravitational-wave detector Advanced LIGO [The15] began its observations and finally detected gravitational waves originating from a binary black hole merger for the first time in September 2015 [Abb16]. This can be seen as a milestone in the history of gravitational waves, around 100 years after their prediction in Einstein's general

theory of relativity. The operating detector uses a stabilized laser system [Kwe12] with a high power output. This measurement probably marks only the beginning of numerous detection events in the future, for instance by the planned third generation gravitational wave detectors like the Einstein Telescope (ET) [Pun10].

This thesis describes the development of a laser power stabilization experiment that is needed for the AEI 10 m Prototype, as well as the implementation and the characterization in this environment.

Outline of the Thesis

Chapter 2 gives a general overview of the theoretical background that is needed for this thesis. Here the focus lies on different sorts of noise and on the standard quantum limit of interferometry. The principle of a feedback control loop in terms of laser power stabilization is worked out.

In Chapter 3 the development and realization of the preparation experiment for the power stabilization in the laboratory are described in detail. Possible limitations are depicted and the achieved performance results are discussed.

Chapter 4 presents the experimental setup at the AEI 10 m Prototype with its subsystems and characteristics. Then the focus lies on the implementation of the power stabilization experiment into this new environment.

In Chapter 5 the main conclusions are summarized and an outlook for the future is given.

CHAPTER 2

Theoretical Background

The following chapter explains the theoretical background needed for this thesis. Several aspects need to be addressed here: It starts with a short overview of optics including the Gaussian beam. Then different types of noise as disturbance to signals will be discussed. Here the focus lies on quantum noise as shot noise on a photodiode (PD). In this thesis both terms, shot noise and quantum noise, are used interchangeably. Furthermore, the propagation of light through a beam splitter (BS) needs to be understood. Following this the standard quantum limit (SQL) is explained in context of a Michelson interferometer. Finally, the control loop concept used for this thesis is first illustrated in general and then presented specifically for an active power stabilization. The limitations for a classical laser power stabilization will be carved out, which is important for the experiment.

2.1 Optics

The fundamentals of optics are the behavior of propagating light and the interaction of light and matter. There are two approaches to describe optics: ray optics and wave optics. Phenomena like interference, diffraction and polarization are explained by wave optics [Ufi14]. Ray optics, also called geometrical optics, describes light by ideal linearized beams and only geometric methods are needed [Haf08]. This section starts with the fundamental Maxwell equations of optics that are leading to the Wave equation. In wave optics every wave can be described by a solution of this equation. The Gaussian beam as a result of the Maxwell equations, finally gives a description for the propagation of light in a simplified ray optics formalism.

2.1.1 Maxwell Equations

The Maxwell equations are some of the most important equations in optics. In fact they describe the wave character of propagating light.
Electromagnetic fields are defined by the two following vector fields: the electric field $\mathbf{E}$ and the magnetic field $\mathbf{B}$. In general, electric charges and currents form the sources of

these fields. This relation is given by the four Maxwell equations [Moe07]

$$\text{div}\,\mathbf{E} = \frac{\varrho}{\epsilon_0}, \qquad \text{rot}\,\mathbf{E} = -\frac{\partial}{\partial t}\mathbf{B},$$
$$\text{div}\,\mathbf{B} = 0, \qquad \text{rot}\,\mathbf{B} = \mu_0\mathbf{j} + \frac{1}{c^2}\frac{\partial}{\partial t}\mathbf{E}, \tag{2.1}$$

where $\mathbf{j}$ is the current density, ϱ is the charge density, $\epsilon_0 = 8.854 \times 10^{-12}\,\text{As/Vm}$ is the vacuum permittivity, $\mu_0 = 1.257 \times 10^{-6}\,\text{N/A}^2$ is the vacuum permeability, and $c = 299\,792\,458\,\text{m/s}$ is the speed of light [Dem14]. This set of coupled differential equations is simplified to a large extent when light propagates in vacuum. Since there are no free currents ($\mathbf{j} = 0$) nor free charges ($\varrho = 0$), the Maxwell equations simplify to

$$\text{div}\,\mathbf{E} = 0, \qquad \text{rot}\,\mathbf{E} = -\frac{\partial}{\partial t}\mathbf{B},$$
$$\text{div}\,\mathbf{B} = 0, \qquad \text{rot}\,\mathbf{B} = \frac{1}{c^2}\frac{\partial}{\partial t}\mathbf{E}. \tag{2.2}$$

These equations are characterized by high symmetry in the electric and the magnetic fields. In addition with the Lorentz force $\mathbf{F}_\mathrm{L} = q(\mathbf{E} + \mathbf{v} \times \mathbf{B})$ and Newton's second law of motion $\mathbf{F} = \frac{d}{dt}\mathbf{p}$ they explain all electromagnetic phenomena in vacuum [Dem14].

2.1.2   Wave Equation

To deduce the Wave equation, the Maxwell equation for rot $\mathbf{E}$ (Eq. 2.2) has to be taken and multiplied with the curl vector operator. After commutating the time and the position operator and inserting the Maxwell equation for rot $\mathbf{B}$ (Eq. 2.2) it follows:

$$\text{rot}\,\text{rot}\,\mathbf{E} = \text{rot}\left(-\frac{\partial}{\partial t}\mathbf{B}\right) = -\frac{\partial}{\partial t}(\text{rot}\,\mathbf{B}) = -\frac{1}{c^2}\frac{\partial^2}{\partial t^2}\mathbf{E}. \tag{2.3}$$

With keeping in mind that rot rot $\mathbf{E} = \mathbf{grad}(\text{div}\,\mathbf{E}) - \Delta\mathbf{E}$ and that div $\mathbf{E} = 0$ (Eq. 2.2) the resulting equation looks like this: [Moe07]

$$\Delta\mathbf{E} = \frac{1}{c^2}\frac{\partial^2}{\partial t^2}\mathbf{E}. \tag{2.4}$$

Similar considerations when calculating rot rot $\mathbf{B}$ create an analogous equation with the magnetic field:

$$\Delta\mathbf{B} = \frac{1}{c^2}\frac{\partial^2}{\partial t^2}\mathbf{B}. \tag{2.5}$$

These two equations are Wave equations in electromagnetism for the electric and magnetic fields.
The Wave equation can be simplified if the focus lies on monochromatic waves having a harmonic time evolution. An electric field $\mathbf{E}(\mathbf{r},t)$ having these properties can be described

by using complex numbers: [Mes08]

$$\mathbf{E}(\mathbf{r},t) = \text{Re}(\mathbf{E}(\mathbf{r})e^{-i\omega t}). \tag{2.6}$$

The parameter ω gives the frequency of the light field. Now the following advantage is given: By using the identity $\omega^2 = c^2\mathbf{k}^2$ with the wave vector $\mathbf{k}$ and the Wave equation (Eq. 2.4), the Helmholtz equation succeeds: [Mes08]

$$(\Delta + \mathbf{k}^2)\mathbf{E}(\mathbf{r}) = 0. \tag{2.7}$$

This equation is position dependent and forms the basis for the following investigations.

2.1.3 Gaussian Beams

A rather simple solution of the Helmholtz equation (Eq. 2.7) is the plane wave, which has an overall constant amplitude. However, this accords inadequately to a real laser beam that is spatially varying. Thus a laser beam can be described more sufficiently by the Gaussian beam. It is a solution of the Helmholtz equation after doing the slowly varying envelope approximation (paraxial Helmholtz equation) [Rog07]. The Gaussian beam is an electromagnetic wave, that is rotational symmetric with respect to the propagation direction. The intensity distribution depends on the propagation range z and the radius r and is given by: [Löf11]

$$I(z,r) = I_0 \left(\frac{w_0}{w(z)} \right)^2 \exp \left(-2\frac{r^2}{w(z)^2} \right). \tag{2.8}$$

The size of the beam is defined by the radius where the maximal intensity is dropped to $1/e^2 \, (\approx 13{,}5\%)$. The minimal radius of a Gaussian beam is the beam waist w_0 and is located in the focus of the beam at $z = 0$. The general beam size can be calculated by

$$w(z) = w_0 \sqrt{1 + \left(\frac{z}{z_{\text{R}}} \right)^2}. \tag{2.9}$$

This function is important for mode matching considerations or to achieve the desired radius at a specific position. In addition to that, the Rayleigh length

$$z_{\text{R}} = \frac{\pi w_0^2}{\lambda} \tag{2.10}$$

characterizes the length where the beam size increases to $\sqrt{2}w_0$. In this formula, λ is the wavelength of the propagating light. For a Gaussian beam the wavefronts are only parallel at w_0. By moving further on in z-direction the wavefronts are curved by the radius of curvature:

$$R(z) = z \left(1 + \left(\frac{z_{\text{R}}}{z} \right)^2 \right). \tag{2.11}$$

This value is at its maximum at the Rayleigh length z_R. Finally, another important beam parameter value is the Gouy phase:

$$\psi(z) = \arctan\left(\frac{z}{z_\mathrm{R}}\right).\tag{2.12}$$

The Gouy phase shows how much the wavefronts of the Gaussian beam are delayed compared to a plane wave. It is important for determining the resonant frequencies of an optical cavity [Nag14]. For larger absolute values of $\psi(z)$, the detection of a Gaussian beam is more sensitive for changes in tilt and for lower values more influenceable in rotation. Additionally, the Gouy phase is larger for higher-order transverse modes.

2.2   Noise Sources

In experimental setups that execute highly precise measurements noise is always a disturbance that can limit the sensitivity. Therefore, in most cases this issue has to be minimized. It is useful to distinguish between two types of noise: random and deterministic noise [Böh13]. Random noise is e.g. shot noise of a laser or electrical noise in a resistor. It consists of absolute casual disturbances and is not repeatable in a new measurement. Deterministic noise is caused e.g. by a gravitational wave in an interferometer [Kwe03]. The description of noise will be the content of the following remarks.
In general, a measured signal is time-dependent and can be characterized by its time series $S(t)$. This could be the power of a laser in a given time interval. However, it is often more convenient to calculate the Fourier transform of the time-dependent signal. It is given by

$$\tilde{S}(\omega) = FT[S(t)] = \frac{1}{\sqrt{2\pi}} \int\limits_{-\infty}^{\infty} S(t)e^{-i\omega t}dt.\tag{2.13}$$

The longer the time series, which will be transformed, is the better the resolution of the frequencies will be. When analyzing the similarity of two different signals $S_1(t)$ and $S_2(t)$, their cross-correlation can be calculated, which compares two signals for different times: [Goo15]

$$R_{S_1 S_2}(\tau) = \langle S_1(t)S_2(t+\tau)\rangle = \lim_{T\to\infty} \frac{1}{T} \int\limits_{-T/2}^{T/2} S_1(t)S_2(t+\tau)dt.\tag{2.14}$$

Here the time shifting is given by τ. The advantage is to find periodic signals in the frequency domain by means of a correlation. If in Equation 2.14 $S_1(t) = S_2(t)$ is true, the function is called autocorrelation. While for deterministic signals the normal Fourier transform is the adequate description in the frequency domain, for random signals it is the so-called power spectral density (PSD) [Kwe03] defined by

$$P_S(\omega) = FT[\langle S(t)S(t+\tau)\rangle] = \frac{1}{\sqrt{2\pi}} \int \langle S(t)S(t+\tau)\rangle e^{-i\omega\tau}d\tau,\tag{2.15}$$

which is a result of the Wiener–Khinchin theorem [Nol11]. This is the Fourier transform of the autocorrelation. In practice the single-sided power spectral density $s^2(\omega)$ is used more often, which is given by [Kwe03]

$$s^2(\omega) = 2P_S(\omega) \tag{2.16}$$

and is only defined for real, thus positive, frequencies. Considering the square root of the single-sided power spectral density results in the single-sided linear spectral density $s(\omega)$ that is also called single-sided amplitude spectral density. If the physical quantity is a voltage, this important parameter has units of $\mathrm{V}/\sqrt{\mathrm{Hz}}$. In terms of interferometric experiments the measured quantity constitutes a length so that $s(w)$ has units $\mathrm{m}/\sqrt{\mathrm{Hz}}$. In this thesis the relative single-sided linear spectral density is usually measured. Thus, $s(\omega)$ is normalized by the DC value of the measurement. The corresponding physical unit is $1/\sqrt{\mathrm{Hz}} = \mathrm{Hz}^{-1/2}$ (see Sec. 2.2.1).

2.2.1 Power Noise

In this thesis the power noise of a laser beam is of high importance. Power noise is a form of random noise that can influence the outcome of an experiment. In a gravitational wave detector it can mask potential gravitational wave signals. Power noise can be split up into two contributions. Firstly, it can originate from technical noise, which can be resistor current noise, beam pointing in combination with spatially inhomogeneous photodiodes, bias fluctuations, scattered light, electrical ground noise, or temperature fluctuations e.g. of the laser crystal. Secondly, there is quantum noise, which originates from the uncertainty of a physical quantity. In optics it originates from the quantization of the light energy into single photons. Quantum noise can also occur in the current of a conductor. A closer look on quantum noise in quantum optics is given in Section 2.2.2.
In order to understand the power noise of a laser, it is important to describe the power output of a laser system, which is described by the time series $P(t)$. Therefore, the average value can be calculated

$$P_0 = \overline{P(t)} = \frac{1}{T} \int_T P(t) \, dt. \tag{2.17}$$

Here the parameter T denotes the time of measurement. With this the power fluctuations can be written as

$$\delta P(t) = P(t) - P_0. \tag{2.18}$$

Now the relative power fluctuations can be directly computed in the time domain by the power noise scaled with the average power $\delta P(t)/P_0$. Since this is more common in the frequency domain, one can define [Sei10]

$$\mathrm{RPN}(f) = \frac{\delta P(f)}{P_0} \quad \text{in units of} \quad \frac{1}{\sqrt{\mathrm{Hz}}}, \tag{2.19}$$

where $\delta P(f)$ is the single-sided linear spectral density of power fluctuations. Equation 2.19 calculates the relative power noise (RPN) or the relative intensity noise (RIN) as relative single-sided linear spectral densities. This parameter is one of the most decisive ones for this thesis.

2.2.2   Quantum Noise

To see the bare quantum noise, the technical noise has to be suppressed below the quantum noise limit. This limit can be calculated by a shot noise formula. In this section this formula will be deduced as it is one of the most important formulas for the shot noise limited power stabilization.

In quantum optics a laser, which is in the state $|\Psi\rangle$, can be described by the photon number operator $\hat{n}$, which measures the number of photons in the light field. The expectation value $\langle\hat{n}\rangle = \langle\Psi|\hat{n}|\Psi\rangle$ directly counts the average photon number. With the standard deviation $\langle\hat{n}^2\rangle = \langle\Psi|\hat{n}^2|\Psi\rangle$ the variance Δn can be calculated by

$$\Delta n = \sqrt{\langle\hat{n}^2\rangle - \langle\hat{n}\rangle^2}. \tag{2.20}$$

The number operator has its own eigenstates called Fock states $|n\rangle$. This means that a light field, which is described by this state, has a discrete number of photons n. In particular the vacuum state contains only the vacuum fluctuations and no photons. This is written as $|0\rangle$. To change between states in the Fock space, there are two operators required that are called the annihilation operator $\hat{a}$ and the creation operator $\hat{a}^\dagger$. In combination they generate the number operator

$$\hat{n} = \hat{a}^\dagger\hat{a} \tag{2.21}$$

and satisfy the commutation relation

$$[\hat{a},\hat{a}^\dagger] = 1. \tag{2.22}$$

They transform the Fock states as follows: [Ger05]

$$\hat{a}|n\rangle = \sqrt{n}|n-1\rangle \quad \text{and} \quad \hat{a}^\dagger|n\rangle = \sqrt{n+1}|n+1\rangle. \tag{2.23}$$

Another special state is the so-called coherent state $|\alpha\rangle$ that is almost classic and it is a good description for a laser field. It not only predicts the correct field expectation values but it also contains the pure vacuum fluctuations. This state is built up by a superposition of Fock states: [Fox06]

$$|\alpha\rangle = \exp\left(-\frac{1}{2}|\alpha|^2\right)\sum_{n=0}^{\infty}\frac{\alpha^n}{\sqrt{n!}}|n\rangle. \tag{2.24}$$

Special about this is, that these states are eigenstates of the annihilation operator which means that

$$\hat{a}\,|\alpha\rangle = \alpha\,|\alpha\rangle, \tag{2.25}$$

where $|\alpha|^2 = \overline{n} = \langle\hat{n}\rangle$ is the average photon number of the field. In general, α is a complex number and represents the classic steady state component of the electric field [Lam98].
In practice, the laser fields often have a large amplitude and small fluctuations, particularly for laser power stabilization applications. Therefore, the annihilation and creation operators can be linearized by [Fra04]

$$\hat{a}(t) \approx \alpha + \delta\hat{a}(t) \quad \text{and} \quad \hat{a}^\dagger(t) \approx \alpha^* + \delta\hat{a}^\dagger(t). \tag{2.26}$$

Here all terms greater than the first order of the expansion are neglected. In Equation 2.26 α stands for the carrier light amplitude and $\delta\hat{a}(t)$ for small fluctuations, satisfying the following two characteristics:

$$\langle\delta\hat{a}\rangle = \langle\delta\hat{a}^\dagger\rangle = 0, \tag{2.27}$$

$$|\delta\hat{a}| \ll |\alpha| \quad \text{and} \quad |\delta\hat{a}^\dagger| \ll |\alpha|. \tag{2.28}$$

This means that on average the small fluctuation terms do not contribute to the field amplitude. However, they directly correspond to the Hermitian amplitude quadrature operator $\delta\hat{X}_1 = \delta\hat{a}(t) + \delta\hat{a}^\dagger(t)$ [Fra04]. Now the new number operator in the linearized model acting on an electric field can be calculated: [Lam98]

$$\begin{aligned}
\hat{n} &= \hat{a}^\dagger(t)\hat{a}(t) \\
&= (\alpha^* + \delta\hat{a}^\dagger(t))(\alpha + \delta\hat{a}(t)) \\
&= |\alpha|^2 + \alpha\,\delta\hat{a}^\dagger(t) + \alpha^*\delta\hat{a}(t) + \delta\hat{a}^\dagger(t)\delta\hat{a}(t).
\end{aligned} \tag{2.29}$$

Assuming that α is a real number, thus $\alpha = \alpha^*$, a simplified approximation where the last term in Equation 2.29 is neglected looks like:

$$\hat{n} \approx \alpha^2 + \alpha\,\delta\hat{X}_1. \tag{2.30}$$

Now the expectation value and the variance of the new number operator in the linearized model can be calculated:

$$\overline{n} := \langle\Psi|\,\hat{n}\,|\Psi\rangle \approx \alpha^2 + \alpha\,\langle\Psi|\,\delta\hat{X}_1\,|\Psi\rangle = \alpha^2 + \alpha\,\langle\Psi|\,(\delta\hat{a} + \delta\hat{a}^\dagger)\,|\Psi\rangle = \alpha^2, \tag{2.31}$$

$$\mathrm{Var}(\hat{n}) := \langle\Psi|\,\hat{n}^2\,|\Psi\rangle - \langle\Psi|\,\hat{n}\,|\Psi\rangle^2 \approx \alpha^2\,\mathrm{Var}(\delta\hat{X}_1). \tag{2.32}$$

After transforming this into the Fourier space, the power spectral density S of the power noise can be identified as the variance of the number operator [Kwe10]. Then all operators

are frequency dependent, to wit $\hat{n}(t) \to \hat{n}(\omega)$ and $\delta \hat{X}_1(t) \to \delta \hat{X}_1(\omega)$. It follows:

$$S = \mathrm{Var}(\hat{n}(\omega)) = \alpha^2 \, \mathrm{Var}(\delta \hat{X}_1(\omega)). \tag{2.33}$$

To consider the relative power spectral density, the spectrum has to be normalized with $\overline{n}^2 = \alpha^4$, which results in [Kwe10]

$$S_\mathrm{q} = \frac{\mathrm{Var}(\delta \hat{X}_1(\omega))}{\alpha^2}. \tag{2.34}$$

Now a laser beam that is described by a coherent state $|\alpha\rangle$, which only contains quantum noise is considered. The fluctuations are the same as for a vacuum state $|0\rangle$. The relative power noise can be written down after calculating the variance of the amplitude quadrature $\hat{X}_1$:

$$\mathrm{Var}(\delta \hat{X}_1) = \langle 0| \, (\delta \hat{X}_1)^2 \, |0\rangle - \langle 0| \, \delta \hat{X}_1 \, |0\rangle^2 = 1 \tag{2.35}$$

$$\Rightarrow S_\mathrm{q} = \frac{1}{\alpha^2}. \tag{2.36}$$

Considering a laser beam with average power P_0 and photon energy hc/λ with the Planck constant $h = 6.626 \times 10^{-34}$ the average photon flow is given by

$$\overline{n} = \alpha^2 = \frac{P_0 \lambda}{hc}. \tag{2.37}$$

This means that for such a beam the relative power noise can be calculated by inserting Equation 2.37 in Equation 2.36 as a relative power spectral density:

$$S_\mathrm{q} = \frac{hc}{P_0 \lambda}. \tag{2.38}$$

In practice, it is often useful to declare the relative power noise as a relative single-sided linear spectral density. This parameter can be calculated by (see Seq. 2.2)

$$s = \sqrt{2S} \tag{2.39}$$

and can generate the shot noise formula for the relative shot noise limit s_q as a relative single-sided linear spectral density: [Sau94]

$$s_\mathrm{q} = \sqrt{\frac{2hc}{P_0 \lambda}} \quad \text{in units of} \quad \frac{1}{\sqrt{\mathrm{Hz}}}. \tag{2.40}$$

This value is suitable for comparisons of relative power noise spectra. The noise of a coherent beam cannot fall below this limit, unless with squeezed-states of light (see [Fra04; Hag04] for further reading).

2.2.3 Noise in a Beam Splitter

Noise can also appear in a beam splitter (BS). To understand this component it is advisable to start with the less complex optical element of a mirror. Every mirror has a reflectance r and a transmittance t predicting what happens to incoming laser light. This means that for an incoming beam two output beams are generated; one is generated in transmission and the other one in reflection. Often only the reflected light is used, which means that most mirrors are highly reflective. In general, a beam splitter shows exactly the same behavior as a mirror. As the name suggests this component purposely splits the beam into two parts. It is necessary to distinguish between a power beam splitter with reflectance r and a polarizing beam splitter (PBS), which splits the light into two polarization shares. In the following, a quantum optical characterization of the beam splitter is made with coherent states. Afterwards, the more demonstrative side band model is described.

Quantum Optics of Beam Splitters

If a laser beam propagates into an optical medium without any disturbances the relative shot noise can be calculated by the shot noise formula from Equation 2.40. When the light travels through a beam splitter, one part of the intensity is transmitted and the other one is reflected. Here, this case will be calculated to obtain how the relative shot noise is changing. The notation is the same as in [Ger05]. A coherent beam with power P_0 written as coherent state $|\alpha\rangle$ travels onto a 50:50 beam splitter in port 1. The vacuum state $|0\rangle$ that contains vacuum fluctuations always enters the beam splitter at the open port 2.
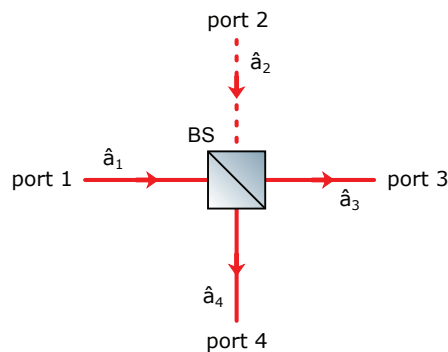

Figure 2.1: The beam splitter in the quantum-mechanical model. All modes $\hat{a}$ that are required for the description of a beam splitter are drawn.

To transform the input modes into the output ones, the new annihilation operators can be distinguished by (see Fig. 2.1)

$$\hat{a}_3 = \frac{1}{\sqrt{2}}(\hat{a}_1 + i\hat{a}_2) \quad \text{and} \quad \hat{a}_4 = \frac{1}{\sqrt{2}}(i\hat{a}_1 + \hat{a}_2). \tag{2.41}$$

The imaginary unit in front of the reflected terms is explained by a produced phase shift of $180°$ for the reflected light according to the Fresnel equations [Pea10]. The incoming

product state in the optical component may be written as:

$$|\text{in}\rangle = |\alpha\rangle_1 |0\rangle_2. \tag{2.42}$$

In terms of the displacement operator $\hat{D}(\alpha) = \exp(\alpha\hat{a}^\dagger - \alpha^*\hat{a})$ this product state can be replaced by: [Ger05]

$$|\text{in}\rangle = |\alpha\rangle_1 |0\rangle_2 = \hat{D}(\alpha) |0\rangle_1 |0\rangle_2. \tag{2.43}$$

With the knowledge of the conservation of two vacuum states in a beam splitter, which means that $|0\rangle_1 |0\rangle_2 \xrightarrow{\text{BS}} |0\rangle_3 |0\rangle_4$ and the relation $|\alpha\rangle_1 |0\rangle_2 = \hat{D}_1(\alpha) |0\rangle_1 |0\rangle_2$, the whole beam splitter can be calculated: [Ger05]

$$\text{Eq. 2.41} \quad \Rightarrow \quad \hat{a}_1 = \frac{1}{\sqrt{2}}(\hat{a}_3 - i\hat{a}_4) \quad \text{and} \quad \hat{a}_1^\dagger = \frac{1}{\sqrt{2}}(\hat{a}_3^\dagger + i\hat{a}_4^\dagger) \tag{2.44}$$

$$
\begin{aligned}
|\alpha\rangle_1 |0\rangle_2 \xrightarrow{\text{BS}} & \exp(\alpha\hat{a}_1^\dagger - \alpha^*\hat{a}_1) |0\rangle_3 |0\rangle_4 \\
= & \exp\left(\frac{\alpha}{\sqrt{2}}(\hat{a}_3^\dagger + i\hat{a}_4^\dagger) - \frac{\alpha^*}{\sqrt{2}}(\hat{a}_3 - i\hat{a}_4)\right) |0\rangle_3 |0\rangle_4 \\
\overset{\text{BCH}}{=} & \left(\exp\left(\frac{1}{\sqrt{2}}(\alpha\hat{a}_3^\dagger - \alpha^*\hat{a}_3)\right)\exp\left(\frac{i}{\sqrt{2}}(\alpha\hat{a}_4^\dagger + \alpha^*\hat{a}_4)\right)\right) |0\rangle_3 |0\rangle_4 \\
= & \hat{D}_3\left(\frac{\alpha}{\sqrt{2}}\right)\hat{D}_4\left(\frac{i\alpha}{\sqrt{2}}\right) |0\rangle_3 |0\rangle_4 \\
= & \left|\frac{\alpha}{\sqrt{2}}\right\rangle_3 \left|\frac{i\alpha}{\sqrt{2}}\right\rangle_4.
\end{aligned}
\tag{2.45}
$$

In the calculation, BCH stands for the Baker–Campbell–Hausdorff formula [Sak93]. This result implies that for a 50:50 BS coherent states are created in both output ports. Now the variances of the quadrature operators $\hat{X}_1$ and $\hat{X}_2$ of the incoming and of the two outgoing beams have to be compared for the beam splitter. For a coherent state $|\alpha\rangle$ is always

$$\text{Var}(\hat{X}_{1,2}) = \langle\alpha| \hat{X}_{1,2}^2 |\alpha\rangle - \langle\alpha| \hat{X}_{1,2} |\alpha\rangle^2 = 1. \tag{2.46}$$

In particular, this is valid for the new states:

$$\text{Var}(\hat{X}_{1,2})_{\text{port 3}} = \left\langle\frac{\alpha}{\sqrt{2}}\right| \hat{X}_{1,2}^2 \left|\frac{\alpha}{\sqrt{2}}\right\rangle - \left\langle\frac{\alpha}{\sqrt{2}}\right| \hat{X}_{1,2} \left|\frac{\alpha}{\sqrt{2}}\right\rangle^2 = 1, \tag{2.47}$$

$$\text{Var}(\hat{X}_{1,2})_{\text{port 4}} = \left\langle\frac{i\alpha}{\sqrt{2}}\right| \hat{X}_{1,2}^2 \left|\frac{i\alpha}{\sqrt{2}}\right\rangle - \left\langle\frac{i\alpha}{\sqrt{2}}\right| \hat{X}_{1,2} \left|\frac{i\alpha}{\sqrt{2}}\right\rangle^2 = 1. \tag{2.48}$$

In summary, the uncertainty of the quadrature operators does not change for the transmitted and reflected light. This means that the absolute quantum fluctuations will remain on the light when passing a beam splitter.

Noise Sideband Model of Beam Splitters

By using the sideband model the beam splitter (BS) can be explained in a very intuitive and simple way, see Figure 2.2 [Bac04]. The situation of laser light traveling through a beam splitter is depicted in a sideband model. In the four diagrams the laser amplitude is plotted against the laser frequency. With the aid of this model, the three acting components can be described efficiently. The laser carrier amplitude at frequency ν, the vacuum fluctuations at all frequencies shown by the gray band, and the modulation sidebands at $\nu - \Omega$ and at $\nu + \Omega$ are representatives for technical noise.
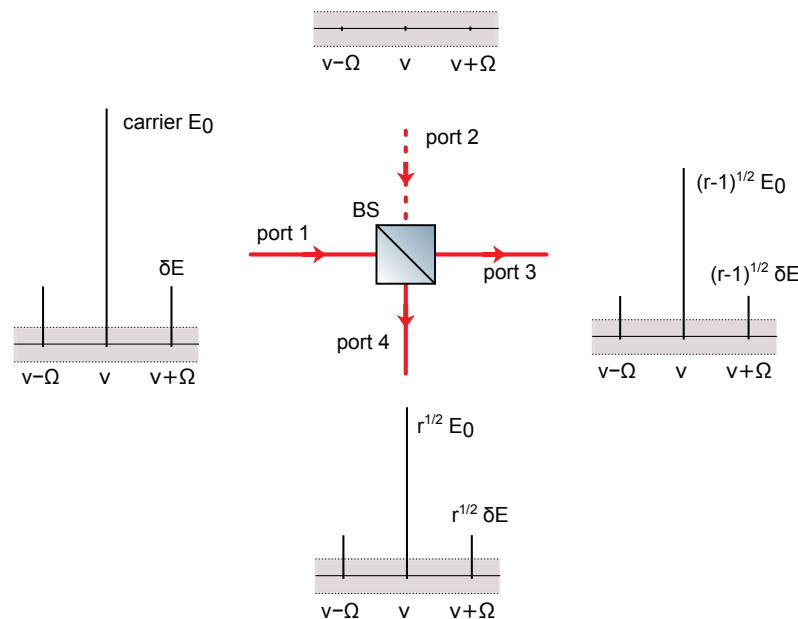

Figure 2.2: The beam splitter in the sideband model. A beam with carrier E_0 and imprinted modulation sidebands δE is divided into two parts. The electric fields are reduced by the amplitude reflectance factor $\sqrt{r}$. The quantum noise drawn with the gray region remain unchanged due to vacuum fluctuations entering the open port of the beam splitter.

In the picture the main beam propagates from the left while vacuum fluctuations enter the open port of the beam splitter from the top. When considering the electric field in the two output ports, it shows that the intensity of the carrier and the size of the modulation sidebands all decrease in the same way. This means that the magnitude of the RPN is conserved when the laser beam is still limited by technical noise behind the beam splitter. Furthermore, it has to be noted that the vacuum fluctuations remain unchanged because the same amount couples into the beam splitter through the open port (compare Sec. 2.2.3). This is valid for all reflectances r. From this it follows, that for a shot noise limited laser beam propagating through a 50:50 beam splitter ($r = 0.5$) the RPN increases by a factor of $\sqrt{2}$ for the outgoing beams.

The discussed approach is consistent with the relative shot noise formula from Equation 2.40. It gives the relative ratio between carrier power and vacuum fluctuations.

2.2.4   Standard Quantum Limit

The sensitivity limit of an interferometer can be analyzed by calculating the standard quantum limit (SQL) of interferometry. Quantum noise itself manifests in two ways in an interferometer. On the one hand there is shot noise and on the other hand radiation pressure noise occurs [Grä13]. Shot noise, also referred to as photon counting noise, originates from their unequal appearing in time. More precisely, the photons follow a Poisson statistic that can be seen by calculating the photon number distribution for a coherent state [Tay16]. The phase distribution of a coherent state is also a Poisson statistic [Ger05] according to its phase uncertainty, which was already calculated in Section 2.2.3. Since an interferometer measures interference in respect to phase shifts in the arms, this noise in the phase quadrature of the light is read out as power noise that limits the sensitivity of the measurement. The following formulas are valid for a simple Michelson interferometer without arm cavities or recycling techniques. The amplitude spectral density of shot noise is given by [Bas14]

$$h_{\text{sno}} = \frac{1}{L}\sqrt{\frac{\hbar c \lambda}{2\pi P}},$$
(2.49)

where L is the arm length of the interferometer. In contrast, radiation pressure noise originates from fluctuations in the amplitude quadrature of the laser light affecting the position of the mirrors by a radiation pressure. This is also referred to as quantum back-action noise [Mat15]. It can be explained by the already mentioned inhomogeneous photon distribution in time. Each photon carries a momentum and by reflecting on the end mirrors, which are considered as free masses, they transfer their momentum. This results in a fluctuating radiation pressure force that remains on the mirrors and thus causes them to change their position permanently. The power fluctuations in the two arms will be anti-correlated [Sau94]. The amplitude spectral density can be written as [Bas14]

$$h_{\text{rpn}} = \frac{1}{mf^2 L}\sqrt{\frac{\hbar P}{2\pi^3 c \lambda}}.$$
(2.50)

Here m is the mass of the end mirrors. When comparing these two effects it can be seen that the power dependence is different. The shot noise contribution falls off as $1/\sqrt{P}$ and the radiation pressure noise contribution increases by $\sqrt{P}$. The frequency behavior is different, too. Shot noise is white while radiation pressure noise shows a $1/f^2$ behavior. Therefore, shot noise dominates at higher frequencies and radiation pressure noise dominates at lower ones. Quantum noise in an interferometer can be defined as the uncorrelated sum of these two contributions [Bas14]. This sum cannot exceed the SQL (see Fig. 2.3). In a usual Michelson interferometer without signal or power recycling techniques the SQL is given by

$$h_{\text{SQL}} = \frac{1}{L\pi f}\sqrt{\frac{\hbar}{m}}$$
(2.51)

in units of strain sensitivity $(1/\sqrt{Hz})$. In Figure 2.3 this limit is demonstrated by the $1/f$-line which results from the total quantum noise by changing the power. Here $m = 100\,\text{g}$,

$L = 10\,\text{m}$, and $\lambda = 1064\,\text{nm}$ are the chosen parameters. The SQL cannot be surpassed in a classical interferometer. Only with methods like detuned signal recycling and quantum non-demolition configurations sensitivities below this limit can be achieved [Bas14].
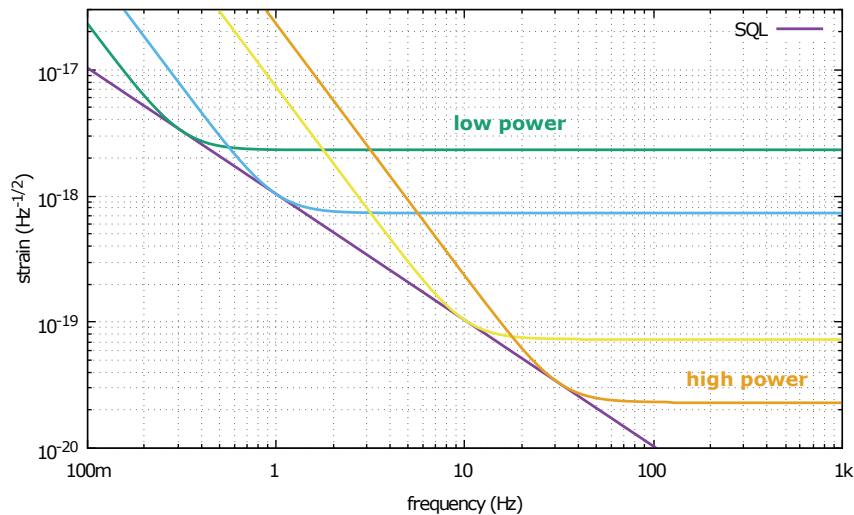

Figure 2.3: Quantum noise curves for different powers resulting in the SQL. The calculation is done for a simple Michelson interferometer without arm cavities or recycling techniques.

2.3 Control Loop Concept

In an experiment, the problem of forcing a value to be of a desired value often exists. Sometimes a measured value should be tracked to a chosen reference to a selected degree of accuracy. This can be done with the implementation of a feedback control system. A general overview of this approach is described in this section.

2.3.1 General Feedback Control Systems

Generally, in an experiment a physical parameter does not have the desired value and fluctuates. For many cases it is necessary to have a higher accuracy for these parameters. A possibility to solve this problem is by using a feedback control system (FCS) [Abr12]. The main idea of this FCS is illustrated in Figure 2.4. A physical process is described by the plant which ideally has no fluctuations. In a real experiment it changes due to environment influences like temperature fluctuations. Summing up the ideal plant with a term representing all environmental noise sources produces the real plant. This signal without an FCS is called *free running*. In practice, this parameter is measured in an experiment.

By means of the block diagram in Figure 2.4 the single blocks will be explained: starting on the right bottom corner with the output, which can be detected by a sensor. It mostly generates a voltage, which, in the best case, behaves linearly to the output. This signal is inverted and is summed on a reference value to generate the error signal. This summation point is called error point. The reference signal can be specified from the outside.
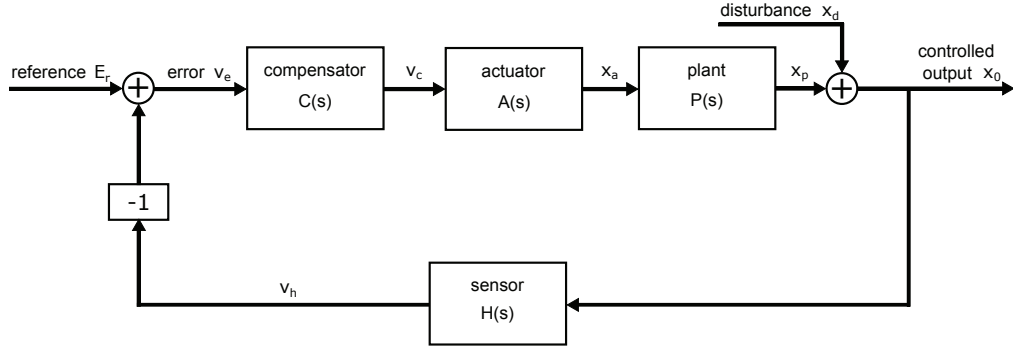
Figure 2.4: Block diagram of a feedback control system to examine the plant output. All blocks representing the sensor, the compensator, the actuator, and the plant can be characterized by the transfer functions $H(s), C(s), A(s), P(s)$. The individual signals between the blocks are written as small letters. On the leftmost summing point, a constant reference value is added onto the inverse sensor output resulting into the error signal.

The compensator (second block) is also called controller or servo. It is used for signal conditioning. The signal is control shaped in such a way that the overall loop becomes stable. The actuator acts as a correction device and should induce negative disturbance on the output. With this closed loop a controlled output can be created. This concept of feedback control systems can be used to suppress disturbances in the desired variable or to control a parameter to a desired size. Block diagrams like this have the advantage of showing the path of a signal directly. Each block represents a signal processing function that can be described by a differential equation respectively.

Another way of characterizing a system is by using the impulse response defined in the time domain. Here the system output is given by the convolution product between the input signal and the impulse response of the system [Abr12]. When not working with very simple systems these two possibilities describing a signal processing function are not very functional [Abr12]. The most popular method to characterize the blocks individually when all components of the feedback system are linear-time-invariant is with a transfer function [Yan13] (see Sec. 2.3.2). The transfer function of a system turns out to be the Laplace transform of the system impulse response [Shm07]. The whole transfer function of a system can be calculated, by multiplying all the single transfer functions of the signal path.

In Figure 2.4 the transfer functions of single systems are written in capital letters. The corresponding signals are represented by small v- and x-letters. The reference value does not have a frequency dependence and is described by E_r. Now the signal v_c behind the compensator can be calculated by

$$v_c = C(s)v_e = C(s)(E_r - H(s)x_0). \tag{2.52}$$

The behavior for the process variable, that has to be controlled, can be computed in steady state

$$x_0 = v_c A(s)P(s) + x_d = x_d - P(s)A(s)C(s)H(s)x_0 + P(s)A(s)C(s)E_r. \tag{2.53}$$

Solving this equation for x_0 results in

$$x_0 = \frac{x_\mathrm{d}}{1 + P(s)A(s)C(s)H(s)} + \frac{P(s)A(s)C(s)H(s)}{1 + P(s)A(s)C(s)H(s)} \frac{E_\mathrm{r}}{H(s)}. \tag{2.54}$$

With the open loop transfer function $G(s) = P(s)A(s)C(s)H(s)$ it follows: [Wil15]

$$x_0 = \frac{x_\mathrm{d}}{1 + G(s)} + \frac{G(s)}{1 + G(s)} \frac{E_\mathrm{r}}{H(s)}. \tag{2.55}$$

This means that the disturbance x_d is suppressed by a factor of $1 + G(s)$. For high open loop gain values $G(x) >> 0$ the size of disturbances changes with $G(s)^{-1}$. The last term $E_\mathrm{r}/H(s) = x_\mathrm{t}$ describes the target value for the process variable. Finally, when designing an FCS, a large open loop transfer function is always desirable. In summary, an FCS takes the free-running process variable including the steady state output and the disturbances, and generates a stabilized output where the fluctuations are reduced by a factor of $1 + G(s)$. The mean value of the output is determined by the reference value.

2.3.2   Stability Criteria

The Nyquist criterion generally states if a system is stable. It can be explained with Nyquist diagrams or often and more comfortably in Bode plots, which is done in the following. An example for a traditional Bode plot can be found in Figure 2.5.
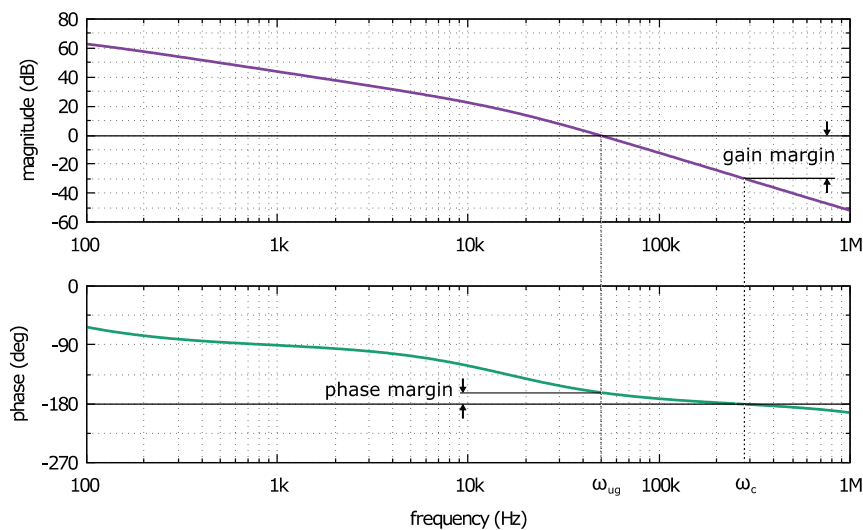

Figure 2.5: Example of a traditional Bode plot. Here the magnitude (gain) $|G(s)|$ and the phase $\phi(s)$ are drawn against the frequency. The unity gain frequency is at $\omega_\mathrm{ug} = 50\,\mathrm{kHz}$ and the critical frequency lies at $\omega_\mathrm{c} = 280\,\mathrm{kHz}$. There the phase margin has a value of $19\,°$. The gain margin can be found where the phase passes $-180\,°$ and is $30\,\mathrm{dB}$ in the magnitude diagram.

It shows the transfer function of a system and usually is a log-log plot of the magnitude or absolute open loop gain $|G(s)|$ and a log plot of the phase $\phi(s)$ versus the frequency.

The magnitude tells how much a system amplifies an incoming oscillation, and the phase calculates how much this oscillation will be shifted over time. Often, the magnitude is calculated in decibel (dB) and the phase is summed by $360\,°$ each time it reaches $-180\,°$ for better presentation. The main advantage of this illustration is that for a constant slope of the log-log magnitude the phase lag is proportional to the slope [Abr12].

Coming back to the Nyquist criterion it can be formulated in a simple way in terms of Bode plots:

> *A control loop is stable, when at the frequencies where*
> $|G(s)| = 1$ *is valid,* $\phi(G(s)) > -180\,°$ *is also fulfilled.*

In Figure 2.5 this condition is fulfilled resulting in a stable control loop. Furthermore, in Bode plots two important frequencies can be found: The unity gain frequency ω_{ug}, where the magnitude passes $0\,\mathrm{dB}$, and the critical frequency ω_{c}, where the phase is at $-180\,°$. The phase margin is the absolute phase distance to $-180\,°$ at the unity gain frequency. In the Figure 2.5 it is $19\,°$ and corresponds to a phase loss of $161\,°$. The gain margin is the absolute magnitude distance from $0\,\mathrm{dB}$ at the critical frequency and accounts to $30\,\mathrm{dB}$ in the diagram. The bigger the margins are the more robust the system becomes. For a simple design the open-loop transfer function $|G(s)|$ should be designed so that at the position where $|G(s)| = 1 = 0\,\mathrm{dB}$, $|G(s)|$ has a slope of $1/\omega$. Small margins would mean a risk of hurting the Nyquist criterion due to fluctuations in the parameters e.g. changes in temperature resulting in instability. For systems with low margins, the transient oscillation time observable in the time domain can be much longer than for systems with higher margins. This could be a risk for ringing, which makes the system instable. In practice, it is recommended to set the phase margin to at least $30\,°$. In detail it depends on each individual application and the requirements.

2.4   Active Power Stabilization

When building up an experiment where a laser beam is used to measure lengths, e.g. in an interferometer, it is essential to have a low noise laser. Different noise sources were already discussed in Section 2.2. The technical noise can be reduced by optimizing the experiment or by building up a stabilization controller. Here a control loop that contains an active power stabilization, which is also used in the experiment for this thesis, will be described. At this point it has to be mentioned that passive stabilization methods also exist. In a passive laser power stabilization, the filter effect of an optical component, e.g. a resonator, is used to suppress power noise. Since these methods are not content of this thesis and have already been discussed in dissertations like e.g. in [Kwe10] or in [Pöl14] they are omitted here. A traditional active power stabilization is illustrated in Figure 2.6.

In the picture a laser that radiates coherent light is depicted. The laser beam propagates through a power actuator and is then split up into two paths. The transmitted beam goes towards the experiment and is called out-of-loop (ool), while the reflected light is detected with an independent photodetector, called in-loop (il), which is comparative to the sensor in Figure 2.4 and transforms the power into a voltage. A feedback control filter is the compensator and uses this voltage for sending a feedback signal to the power actuator. In principle, the power actuator should induce the negative fluctuations on the
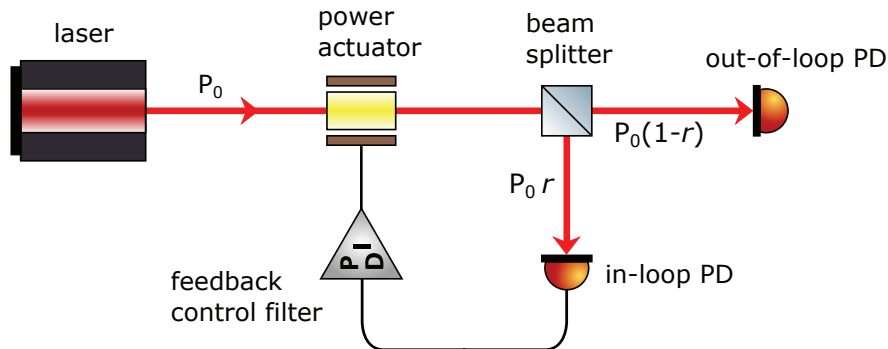
Figure 2.6: Traditional setup of an active power stabilization. A beam splitter with reflectance r splits the laser beam in two parts, which are sent onto the out-of-loop and the in-loop photodiode. A feedback control filter takes in the in-loop signal and influences the power actuator so that the power noise is suppressed. Often the stabilized laser power on the out-of-loop sensor is needed for an experiment.

light resulting in a stabilized laser going to the experiment. This concept has been applied in many publications before. But in detail they differ, which is discussed in the following. The pump power of the laser system can be used as an actuator, which was done in many publications before [Abb01; Bar05; Har94; Mio07; Mus14; Noc04; Ott00; Rol04; Row94; Tsu92; Zaw02]. The advantage of this method is that by using less power the reduction of power fluctuations increases. Furthermore, cross couplings into other laser parameters can be produced with an internal actuator. An external actuator couples less in changes of laser dynamics. In some experiments, e.g. in [Kim07; Sei06; Tak08], acousto-optic modulators (AOMs), in other ones, e.g. in [Iva09; Kwe09b; Nag98], electro-optic amplitude modulators (EOAMs) were used. An AOM uses acoustic waves in a crystal to diffract light under an angle and to split it from the main beam. By varying the amplitude of the radio frequency (RF) the power remaining in the zeroth diffraction order is actuated. The diffraction efficiency is linear to the drive power. An EOAM works with the Faraday effect to rotate the polarization of a beam. Together with a PBS the power in the beam can be actuated.

The noise which is measured at the il and ool ports has ideally the same level, which is given by the quantum noise limit. In many experiments it has been observed that sometimes unexplained differences between the ool and the il sensor are measured. Often the noise at the ool photodetector is higher than at the il sensor. This is the case especially at lower frequencies in the region around 10 Hz where they are not quantum noise limited anymore. Many different noise sources cause this discrepancy. It could be photodiode internal low-frequency noise, resistor current noise, beam pointing in combination with spatially inhomogeneous photodiodes, dust particles passing the beam, temperature fluctuations e.g. in the laser crystal, scattered light, bias fluctuations, electronic ground noise, or polarization fluctuations [Bar05; Kwe10; Kwe09b; Rol04; Sei10; Sei06]. By optimizing the experiment like using vacuum tanks or noise suppressing mode-cleaning resonators or optical fibers, these different noise sources can be reduced. The concept of a vacuum tank

was used before in works like [Bar05; Kwe10; Kwe09b; Mio07; Rol04; Sei06; Tak08].

2.4.1   Limit of a Traditional Laser Power Stabilization

The main question is by how much the power noise can be reduced in the beam that is going to the experiment (out-of-loop) for a traditional laser power stabilization as mentioned in Section 2.4. For convenience, it is assumed that the photo detectors of the in-loop and the out-of-loop beam paths do not have electronic noise and the optics are lossless. Furthermore, the loop gain is sufficiently high to suppress all technical noise. As illustrated in Figure 2.6 the il signal is used to stabilize the laser beam with a feedback control loop. Unfortunately, the quantum noise measured with the il sensor is imprinted on the ool beam by the control loop. Additionally, the vacuum fluctuations reflected on the beam splitter contribute to the noise on the ool beam. Now the total power noise on the ool detector achievable in a traditional power stabilization experiment consists of these two contributions:

$$\mathrm{RPN}_{\mathrm{TPS}} = \sqrt{s_{\mathrm{q,ool}}^2 + s_{\mathrm{q,il}}^2} = \sqrt{\frac{2hc}{rP_0\lambda} + \frac{2hc}{(1-r)P_0\lambda}} = s_{\mathrm{q}} = \sqrt{\frac{1}{r(1-r)}}\sqrt{\frac{2hc}{P_0\lambda}}. \quad (2.56)$$

Here P_0 is still the original power of the laser system before the beam splitter (see Fig. 2.6). By making the reflectance r smaller ($r < 0.5$) this performance limit is dominated by the in-loop quantum noise and by making r greater ($r > 0.5$) it is dominated by the out-of-loop quantum noise. When the power in transmission and reflection has the same value ($r = 0.5$) both contributions add equally to the total power noise. The function $\mathrm{RPN}_{\mathrm{TPS}}$ has a minimum, which means that the lowest power noise that can be achieved with a traditional power stabilization experiment, requires a 50:50 beam splitter [Kwe10]. With the 50:50 beam splitter Equation 2.56 can be simplified to

$$\mathrm{RPN}_{\mathrm{TPS}}^{r=0.5} = 2\sqrt{\frac{2hc}{P_0\lambda}}. \quad (2.57)$$

In practice, losses of optical components and the quantum efficiency η of the photodiodes have to be respected. Therefore, it can be easier to consider the electrical photocurrents I_{il} and I_{ool}. η gives the rate of photons that are converted into electrons. For an ideal photodiode with $\eta = 1$ every detected photon is converted into an electron contributing to the photocurrent. For a real photodiode the quantum efficiency is always $\eta < 1$ which means that the process of photon detection generates extra noise [Sei10]. Thus it is often easier to use the electrical photocurrents I_{il} and I_{oof} of the in-loop and out-of-loop detector [Kwe10]. The average photon flow is replaced by the average electron flow. Then the noise contributions written in Equation 2.56 can be then calculated as

$$s_{\mathrm{q,il}}' = \sqrt{\frac{2e}{I_{\mathrm{il}}}}, \quad (2.58)$$

$$s_{\mathrm{q,ool}}' = \sqrt{\frac{2e}{I_{\mathrm{ool}}}}, \quad (2.59)$$

and the relative shot noise limit of a traditional power stabilization experiment in terms of photocurrents now reads as

$$\text{RPN}'_{\text{TPS}} = \sqrt{\frac{2e}{I_{\text{ool}}} + \frac{2e}{I_{\text{il}}}}.$$
(2.60)

In this thesis Equation 2.60 is used when calculating the shot noise level of a traditional power stabilization experiment.

CHAPTER 3

Power Stabilization Preparation Experiment

The aim of this thesis is to develop a power stabilization experiment for the Albert Einstein Institute (AEI) 10 m Prototype. As the working conditions in the prototype's vacuum tank are difficult, the experiment was set up in a separate laboratory before. The conceptual setup was assembled there, and it was further developed and improved as much as possible. When the desired performance was achieved, the experiment was moved to the vacuum tank and was implemented there. The design demanded the relative power noise (measured with an out-of-loop sensor) to be shot noise limited for frequencies around 200 Hz. To achieve a relative shot noise level of about $2 \times 10^{-9} \, \mathrm{Hz}^{-1/2}$ on the out-of-loop sensor, a power of at least 187 mW needs to be detected on the in-loop sensor (see Eq. 2.56). When detecting the light with a photodiode with quantum efficiency of about $\eta = 0.92$, the power detection requirement increases to 203 mW (see Eq. 2.60) due to the shot noise of the electric current.

In this chapter, the preparation experiment set up in the laboratory will be described and characterized. The conceptual setup will be discussed first, before the individual optical components like the photodiode array are explained in more detail. Then the readout and the control electronics are described. Considerations about the reduction of pointing noise are explained next, before finally the achieved results are shown and discussed.

3.1 Conceptual Setup

In setting up the stabilization experiment, the remarks from Section 2.4 are taken as a basis. A similar concept was already presented in publications like [Kwe12; Kwe11b; Kwe09b; Sei06; Wil08]. A schematic overview of the experimental setup in the laboratory is shown in Figure 3.1.

A fiber-coupled nonplanar ring oscillator (NPRO) [Innolight, Mephisto 500 NE FC] is used as the laser source, emitting a power of up to 400 mW. The 1 m long polarization maintaining fiber [Schäfter + Kirchhoff, PMC-980-6,6-NA012-3-APC-100-P] ends with a collimator [Schäfter + Kirchhoff, 60SMS-1-4-A4.5S-03] where the light is coupled out. The wavelength of the light is 1063.83 nm ± 0.05 nm. The laser radiation is almost entirely contained in the TEM_{00} (transverse electromagnetic) Gaussian mode. A complete characterization of the laser can be found in Section 3.1.1. The light is sent to an attenuation stage consisting of a half-wave plate and a PBS to control the power entering the experiment without changing
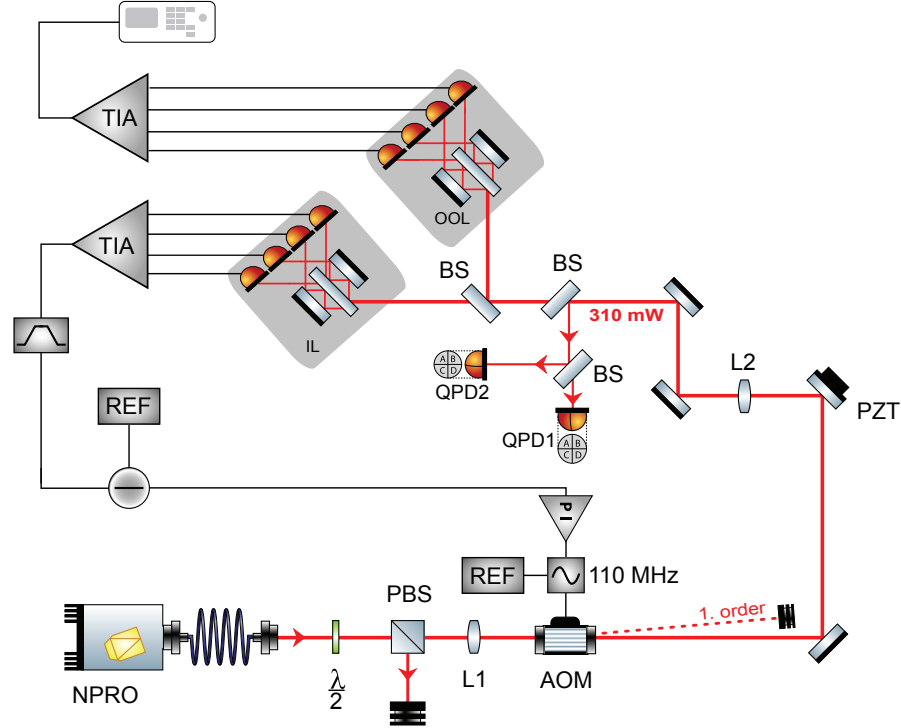
Figure 3.1: The experimental setup in the laboratory. A fiber-coupled NPRO serves as the laser source, and an AOM is used to actuate the power. Furthermore, a deflecting mirror mounted on a piezoelectric element is placed in the beam path in order to actuate and correct the beam pointing error. During the test-run the incoming power into the photodiode array was about $310\,\text{mW} \pm 2\,\text{mW}$. All deflecting mirrors are $45\,°$ mirrors for $1064\,\text{nm}$ light and have a transmittance of $0.02\,\%$.

the diode current. The lens L1, with a focal length of $f_1 = 200\,\text{mm}$, is placed in front of an AOM [Crystal Technology Inc., AOMO 3110-125] to focus the beam into the crystal. At this point the beam diameter has a size of $80\,\text{µm} \pm 10\,\text{µm}$. The best diffraction efficiencies were observed with this geometric beam size. With the full power of $400\,\text{mW}$, the maximal intensity in the crystal is a factor of at least 2000 less than the damage threshold of the AOM. The modulator allows controlling the power in the zeroth diffraction order. The excess light is diffracted into the first diffraction order under an angle of $27.8\,\text{mrad}$ and is sent to a beam dump. The AOM serves as an actuator for the feedback control system and is driven by an external driver unit [NEOS Technologies, 21080-2AM] with frequency of $110\,\text{MHz}$. The bandwidth of the AOM was measured with a transfer function to be around $500\,\text{kHz}$. In the experiment, a maximal diffraction efficiency into the first diffraction order of about $30\,\%$ was achieved. The beam is then deflected by a mirror which is mounted on a biaxial piezoelectric element [Piezosystem Jena, PSH 4], which allows the beam pointing to be modulated (see Sec. 3.2). The second lens L2 has a focal length of $f_2 = 200\,\text{mm}$ and is needed to achieve the correct beam radius on the photodiodes (see 3.1.2). The two deflecting mirrors placed behind the lens assist in aligning the beam into the complex

sensor: the photodiode array (compare Fig. 3.2). This element consists of four in-loop and four out-of-loop photodiodes and two quadrant photodiodes (QPDs), which transform the incident light into a photocurrent. A full description of the photodiode array can be found in Section 3.1.2, including a more detailed description of the beam path. Transimpedance amplifiers (TIAs) convert the currents of the photodiodes into eight voltages, the in-loop and the out-of-loop currents are summed up respectively. The out-of-loop signal can be observed on an oscilloscope. The in-loop voltage first passes a band-pass filter and is then summed with a constant reference voltage, generating the error signal of the control loop. It is sent to a proportional-integral controller (PI controller), which produces a signal that is fed back to the AOM via the driver unit, which then modulates the light. The loop is closed at this point. Now the AOM will actuate the laser beam so that the noise is suppressed. A more detailed description of the electrical path is given in Section 3.1.3.
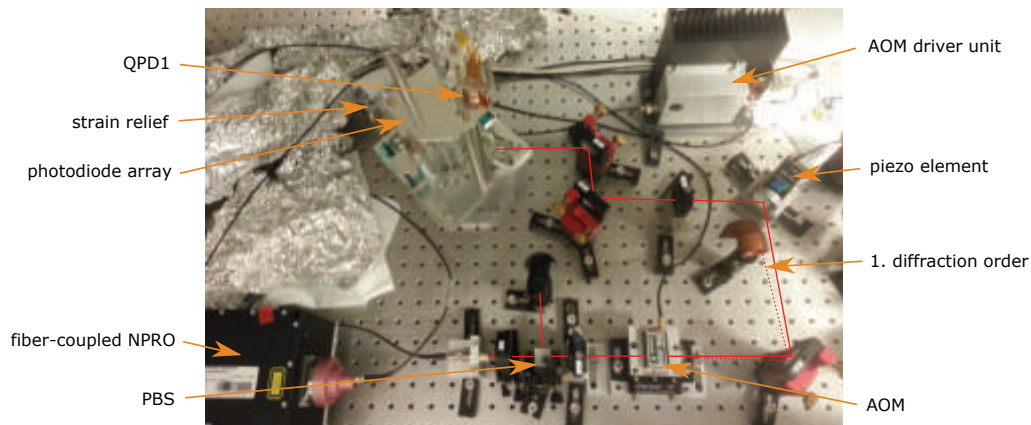

Figure 3.2: A picture of the experimental realization. All components are mounted on a breadboard. The laser beam is depicted by the red line and propagates in anticlockwise direction starting on the left bottom corner behind the fiber-coupled NPRO. The second quadrant photodiode (QPD2) was not included in the array when this picture was taken. The electronics are placed in a rack next to the setup (not visible).

3.1.1   Characterization of the NPRO Laser

An NPRO laser was used for the test run in the laboratory. This solid-state laser is very stable, compact and rugged. A monolithic Nd:YAG (neodymium-doped yttrium aluminum garnet) crystal serves as both the active medium and the resonator. The light is traveling and being amplified in circular direction. The front face has a partially reflective dielectric mirror coating, which serves as a highly reflective surface for the circulating light while simultaneously serving as an output coupler. On the other surfaces, the light is totally internally reflected.

The laser system has the possibility to change the temperatures of the laser crystal and the laser diode to determine laser parameters like output power and wavelength. The laser output can be controlled by the pump current in a range of up to $1234\,\mathrm{mA}$, see Figure 3.3. The highest power of $399\,\mathrm{mW} \pm 1\,\mathrm{mW}$ was measured at a current of $1234\,\mathrm{mA} \pm 0.5\,\mathrm{mA}$

and at a laser diode temperature of about $25\,°C \pm 0.01\,°C$. The temperature should not be set much higher due to considerable reductions in durability. No changes in the output power have been observed by modifying the crystal temperature in a range of a few degrees Celsius. Finally, a crystal temperature of $25.5\,°C$ was chosen.
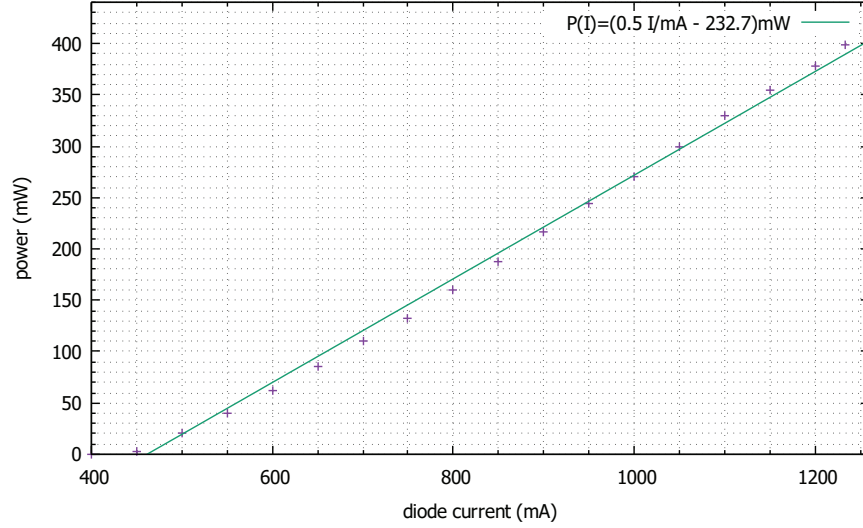

Figure 3.3: Measurement of the output power of the fiber-coupled NPRO, drawn against the diode current. The laser threshold lies at a current of about $445\,mA$. The measurement uncertainties are $\Delta P = \pm 1\,mW$ and $\Delta I = \pm 0.5\,mA$ - too small for a meaningful illustration in the graph.

The laser's power noise can be characterized by measuring the relative power noise (RPN) which was introduced in Section 2.2.1. The measurement (like all measurements in this thesis showing an RPN) was taken with a dynamic signal analyzer [Stanford Research Systems, SR785] and can be found in Figure 3.4. The RPN has a value of about $(1.5 \pm 0.3) \times 10^{-3}\,Hz^{-1/2}$ at $100\,mHz$, and then decreases with $1/f$ to a value of about $(7.6 \pm 0.5) \times 10^{-6}\,Hz^{-1/2}$ for a frequency of $100\,Hz$. At $800\,Hz$ it is minimal with an RPN of $(3 \pm 0.2) \times 10^{-7}\,Hz^{-1/2}$ and afterwards it again increases by a factor of 3 up to $100\,kHz$. This increasing behavior for higher frequencies is not typical for NPRO lasers, but is due to the fiber coupler. The laser has an integrated noise eater option to suppress the relaxation oscillation, which originates from the resonant coupling between the laser medium and the resonator. Every laser system has this strong source of laser noise, usually at a frequency between a few ten kilohertz and a few megahertz. The relaxation oscillation peak for the fiber-coupled NPRO has a frequency of about $465\,kHz \pm 1\,kHz$, and can be completely suppressed by activating the noise eater. This frequency region is however not very relevant for the power stabilization experiment.

The goal of this preparation experiment in a laboratory environment is to establish a shot noise level for a high amount of power. This means, by looking at Figure 3.4 again, that the RPN has to be suppressed to a level of several $10^{-9}\,Hz^{-1/2}$ for laser powers of at least a few ten milliwatt per photodiode.
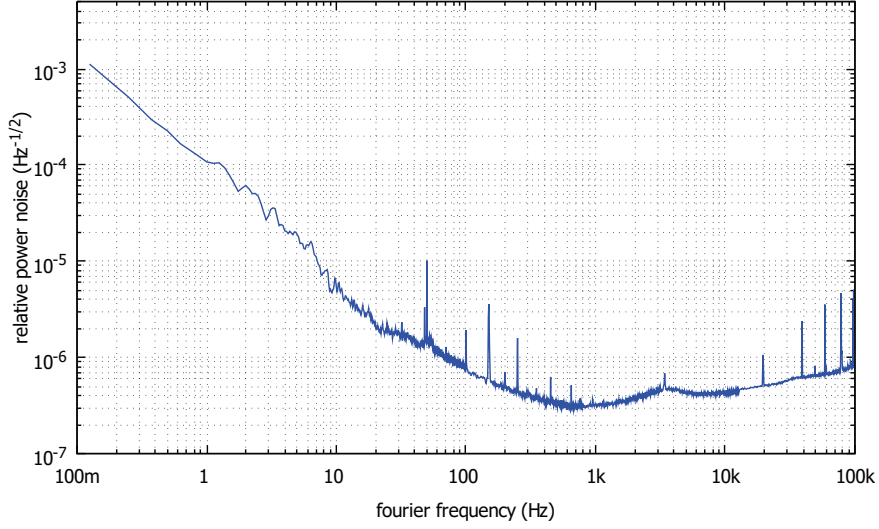
Figure 3.4: Measurement of the free-running relative power noise of the NPRO laser with the AC band-pass filtered signal of a single photodiode of the photodiode array (see Section 3.1.3.1). The detected power on the photodiode has a value of $45\,\text{mW} \pm 1\,\text{mW}$. Note the peaks at the current supply frequency of 50 Hz, and multiples of it. Peaks at frequencies of about 19.5 kHz and multiples of it are dominant. They originate from electronic issues in the band-passed AC path and disappear while measuring the RPN with the DC-channel, or behind the summation point. Measurements with the other seven photodiodes yield largely identical results.

3.1.2   High-Sensitivity Photodiode Array

The photodiode array (see again Fig. 3.2) was developed to detect high power light in order to achieve the $10^{-9}\,\text{Hz}^{-1/2}$ stability range, and to be able to reach the sensitivity required for Advanced LIGO (aLIGO). The design of this requirement has already been described in some works like in [Kwe10; Sei10], and is not restated here. Some experiments [Kwe10; Kwe09b; Põl14] have already used the photodiode array as a sensor and characterized it - hence only the most important details are shown here.

At the AEI 10 m Prototype, the RPN has to be reduced to a level of $2 \times 10^{-9}\,\text{Hz}^{-1/2}$ for frequencies in the detection band around 200 Hz. To achieve this low limit of noise, a laser power of at least 203 mW has to be detected on the in-loop and on the out-of-loop sensor, respectively (see Eq. 2.60 for a photodiode quantum efficiency of $\eta = 0.92$). Such a high amount of power on one single photodiode would cause temperature problems only solvable with complicated cooling mechanisms, like it was done in publications by F. Seifert et al. [Sei06] (thermoelectrically cooled) or by F. Cleva et al. [Cle12] (thermoelectrically and water cooled). Additionally, the readout electronics for this single photodiode have to be very low-noise. For these reasons, a high-sensitivity photodiode array consisting of eight photodiodes is used as sensor rather than a single photodiode. Each photodiode has its own readout electronics, and has to detect a power of at least 51 mW to fulfill the AEI 10 m Prototype requirements.

The optical design of the array can be easily understood by looking at the pictures in

Figure 3.2 and in Figure 3.5. The whole array is manufactured from aluminum to allow a vacuum compatible yet robust design. The incoming laser beam is split by two beam splitters into one beam with small power ($\approx 1\,\%$) going to the top of the array, and two beams with equal power propagating onto a wedge shaped beam splitter. They are only vertically separated, and will occasionally be referred to as bot-stage and top-stage. Later these two stages are used as in-loop and out-of-loop sensor. The transmitted and reflected beams resulting from each stage are reflected multiple times by two mirrors and the wedge shaped beam splitter, resulting in four beams of equal power hitting four indium gallium arsenide (InGaAs) photodiodes [Perkin Elmer, C30642] for each stage. They have a theoretical spectral responsivity of about $0.78\,\mathrm{A/W}$ for $1064\,\mathrm{nm}$ light [Elm00]. Previously, this value was measured to $0.79\,\mathrm{A/W} \pm 0.08\,\mathrm{A/W}$ [Kwe10], with a respective quantum efficiency of about $\eta = 0.92$. In this case, a spectral responsivity of $0.79\,\mathrm{A/W}$ was used to calculate the conversion from power to photocurrent. The photodiodes have a bandwidth of up to $75\,\mathrm{MHz}$. The incidence angle is $45\,°$, reducing scattered light and back reflections and allowing easy absorption of residual reflections with blue glass filters [Schott, BG39]. The uncoated glass windows covering the photodiodes were removed for the same reason. The eight photodiodes have an active diameter of $2\,\mathrm{mm}$, and the beam radius was about $250\,\mu\mathrm{m} \pm 80\,\mu\mathrm{m}$ in the experiment, depending on the position of the photodiodes and on the sagittal or tangential direction. However, in a prior experiment no performance differences for beam radii from $60\,\mu\mathrm{m}$ to $720\,\mu\mathrm{m}$ were observed [Kwe09b]. The diodes are glued into small aluminum cases and can be mounted on the wall of the array. At the same time, they are isolated electrically from the aluminum array with Kapton tape to avoid couplings and electrical ground loops.
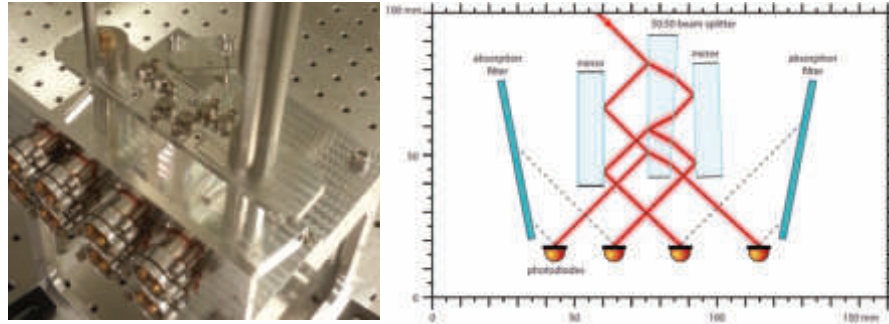

Figure 3.5: On the left, a photograph of the photodiode array is shown. The light enters the photodiode array on the top of the picture and is split up onto eight photodiodes.
On the right, the optical layout including the beam paths is drawn with the help of OptoCAD [Sch05] (taken from [Kwe10]). The layout is the same for the top and the bottom stage.

The beam with low power traveling to the top of the array propagates to another 50:50 beam splitter, from which the split beam continues onto two InGaAs quadrant photodiodes [OSI Optolectronics, Q3000] with an active diameter of $3\,\mathrm{mm}$ and a small gap with a size of $45\,\mu\mathrm{m}$ between the quadrant elements. The uncoated glass cover of the QPDs was also removed. One of the quadrant photodiodes can be seen in Figure 3.2 on the top of the

array, the other one was mounted on the side below the cover later. This modification was done to read out the now uncoupled beam parameters independently. This can be achieved by placing the beam waist between the two quadrant photodiodes, and by having a Gouy phase difference of $90°$. On the top quadrant photodiode, also referred to as QPD1, the beam radius is about $250\,\mu m \pm 40\,\mu m$, and on the other one at the side (QPD2) it is about $100\,\mu m \pm 20\,\mu m$. The respective Gouy phases are about $65°$ for QPD1 and $-25°$ for QPD2. The two quadrant photodiodes can be orientated by shifting (QPD1), or aligned with a vacuum compatible XY-adjusting-mounting-plate [Owis, OH 40] (QPD2). A photograph of the improved photodiode array design containing the second quadrant photodiode can be found in Figure A.2 in the appendix.

All components of the photodiode array, such as Macor coated fused silica and glass components, glues and Kapton foils are vacuum compatible. The photodiodes and quadrant photodiodes are connected by female SMP connectors crimped on vacuum compatible shielded twisted pair cables. These cables are held by a custom made strain relief to protect the sensitive SMP-cable connection from mechanical forces. The aluminum plate, where the mirrors and the beam splitters are fixed onto, is held by a self-designed octagonal base plate via four cylindrical bases.

3.1.2.1   Calibration of the Quadrant Photodiodes

The position and the beam parameters of the two quadrant photodiodes have already been described in Section 3.1.2. The photocurrents of the four quadrants are read out, and the difference voltages of the half planes are calculated by analog devices. The position of the beam is described by the four differential signals of the two quadrant photodiodes. To investigate potential influences of beam pointing, the coupling factors (relation between voltage and beam displacement) of the two quadrant photodiodes are relevant, and were investigated as follows.

To achieve a high accuracy, a beam displacement was induced using the piezoelectric element at a constant voltage at different magnitudes. After inducing the beam displacement the differential voltages of the two quadrant photodiodes were measured. Additionally the constant coordinates of the beam at the two fixed positions ($55.5\,cm \pm 0.3\,cm$ for QPD1 and $60.5\,cm \pm 0.3\,cm$ for QPD2 behind the piezoelectric element) were assessed with a laser beam profiling camera after the photodiode array was removed. This allowed connecting the beam displacement to the change in the differential voltages. Since a voltage applied only on the x tilt of the piezoelectric element usually couples in both pointing directions x and y, the displacement measured with the laser beam profiling camera was translated into a radial tilt. Furthermore, the quadrant photodiodes were randomly rotated, noting the uncoupled behavior of x and y tilt of the piezoelectric element. Thus the known radial displacement was transformed back into the x and y pointing tilt. By this method, problems with coupled piezoelectric element axes could be avoided.

The measured beam waists are about $280\,nm \pm 4\,nm$ with a small ellipticity ($\varepsilon = 0.84$) for QPD1 and $90\,nm \pm 3\,nm$ for QPD2. The beam on QPD2 was nearly Gaussian. The total detected power on each photodiode was estimated to be $300\,\mu W \pm 50\,\mu W$. The resulting coupling factors from the measurements are given by $\zeta_1 = 1.2\,mV/\mu m$ for QPD1 and $\zeta_2 = 91\,mV/\mu m$ for QPD2, respectively. Both values are calculated averages for the x and

y displacements on the quadrant photodiodes. The coupling factors are a mere estimation, and not very precise due to numerous uncertainties. For example, the different voltages are constantly fluctuating mainly due to pointing jitter of the beam itself, and therefore an average value was taken during the measurement. The hysteretic behavior of the piezoelectric element was considered and averaged, which produced an error especially for small voltages. The position of the laser beam profiling camera had an error of at least a few millimeters, as the beam propagation lengths in the array are unknown and only estimated. Possible inhomogeneities in the sensitivity of the individual quadrants can disturb the measurement, too.

The great discrepancy between the two coupling factors for the two quadrant photodiodes cannot be explained by the small difference in beam size. To investigate this strange behavior, an algebraic simulation was written with the software Mathematica [Res10], which calculated the coupling factors based on the measured beam radii, the gap of the quadrant photodiodes and the incoming power. A perfect Gaussian beam with intensity distribution which was already shown in Equation 2.8 was assumed. Furthermore, a quantum efficiency of $\eta = 0.92$ was estimated, and the TIAs were assumed to work ideally. The resulting simulation agrees well with the coupling factor of QPD2; however, for QPD1 the simulated coupling factor was quite different from the measured one. This could be explained by issues with the TIA for QPD1, which had to be rebuilt a short time after the first measurements due to electrical disturbances. The electronics likely did not achieve their full performance during the measurements. As a result, the measured results for QPD1 are not really plausible and credible. Finally, the resulting coupling or calibration factors are roughly given by the ones from the simulation:

$$\zeta_1 = 39\frac{\text{mV}}{\text{µm}} \quad \text{for QPD1 and} \tag{3.1}$$

$$\zeta_2 = 91\frac{\text{mV}}{\text{µm}} \quad \text{for QPD2.} \tag{3.2}$$

The errors in both values are estimated to be more than $20\,\%$. Furthermore, the calibration factors are only valid in the linear region for displacements from the origin of $\pm\,70\,\text{µm}$.

3.1.3   Electronics

In this section, the electric components of the experiment will be discussed. In general, power stabilization experiments require low noise electronics that do not limit the sensitivity. The TIAs for the two quadrant photodiodes are slightly modified standard devices developed at the Albert Einstein Institute. In the following section, the focus lies on the TIA for the eight photodiodes, which has an integrated band-pass filter. Additionally, the feedback control filter will be considered and illustrated in a block diagram.

3.1.3.1   Transimpedance Amplifier

The TIA used for the readout of the photodiode signals in this experiment is a strongly modified version from P. King from LIGO with Document Control Center (DCC) name "D1300639-v1". Each photodiode is connected by a vacuum compatible shielded twisted pair cable. The two channels are for the anode and the cathode. The shielding is set on the
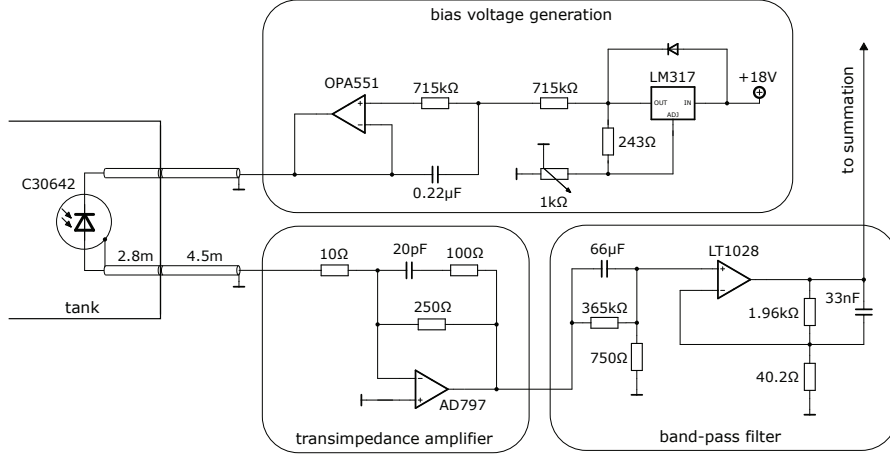
Figure 3.6: Schematic drawing of the readout electronics for one photodiode, including the bias voltage generation. The vacuum tank drawn here is not present at the experiment in the laboratory.

ground contacts of the photodiodes and is isolated from the photodiode array. The 2.8 m long, shielded twisted pair cables are connected to a D-Sub-37 to later reach the flange in the vacuum tank of the AEI 10 m Prototype, which interfaces vacuum and laboratory. To reach the location where the TIAs will be placed from the flange, an roughly 4.5 m long cable switching D-Sub-37 to male SMA connectors is needed. The pin assignment for this can be found in Figure A.3 of the appendix.

The complete readout electronics for the photodiodes are shown in Figure 3.6. The supply voltage for the bias generation comes from the GEO supply of the laboratory ($\pm 19\,\text{V}$), as this replicates the conditions at the AEI 10 m Prototype. A voltage transformer LM317 in combination with a potentiometer is used to generate the bias voltage, which is then applied on an OPA551 high-voltage, high-current operational amplifier. When the potentiometer is adjusted to $722\,\Omega$ the output will be the desired 5 V bias voltage to keep the dark current low, which is applied to the cathodes of the eight photodiodes. Since all TIA electronics for each stage are integrated in an individual box, the bias supply generation is separated. The photocurrents generated in the anodes of the photodiodes are then sent to the TIA element. It consists of a very low noise operational amplifier [AD797] with a typical input voltage noise of about $0.9\,\text{nV}/\sqrt{\text{Hz}}$ at 1 kHz. To aid keeping the noise as low as possible, a special resistor [Farnell, Y0785250R000T9L] with a highly precise resistance of $250\,\Omega \pm 0.01\,\%$ was used for the circuit. It has a very small temperature coefficient of about $2\,\text{ppm/°C}$, which reduces current noise originating from temperature fluctuations. The amplification of this TIA element depends only on the resistance value, and for this new design the gain is 250 or 48 dB. This means that for a desired DC value of about 10 V during operation, the photocurrent has a value of 40 mA, corresponding to a power on a single photodiode of about 50.6 mW while assuming a quantum efficiency of $\eta = 0.92$. This power is close to the desired 51 mW per photodiode. The generated voltage can be measured for every photodiode via a self-designed DC-readout channel which is a LEMO
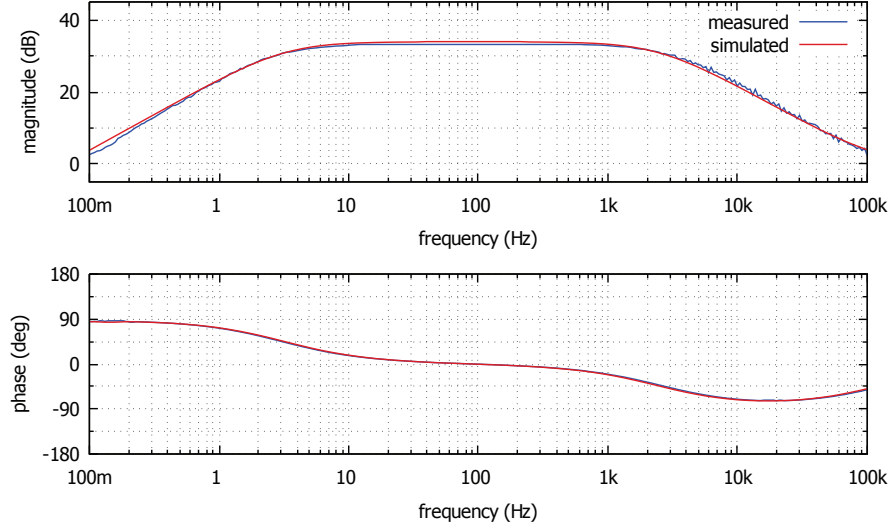
connector.

Figure 3.7: Measured and simulated transfer function of the band-pass filter. The frequency dependent magnitude behavior is shown above and the phase behavior is drawn below. The measurement was done by feeding a swept sine signal with an amplitude of about 100 mV into the LT1028. The simulation was done with the program LISO [Hei00] and conforms well with the measurement.

Furthermore, the voltage is applied on a AC path consisting of a band-pass filter that increases all frequencies between 3 Hz and 2.5 kHz by 34 dB. These are the most interesting frequencies for laser power stabilization experiments in terms of ground based gravitational-wave detectors, which are in the sensitivity band between 1 Hz and 1 kHz [Kop14; Sat09]. In contrast to that, the AEI 10 m Prototype wants to reach the SQL for frequencies around 200 Hz. The slopes of the magnitude of the band-pass filter's transfer function are characterized by an 1/f-behavior, and for lower frequencies the magnitude is reduced by 20 dB, so that the voltages can be added more easily later and do not saturate the electronics. The main device of the band-pass filter is the ultralow noise precision LT1028 operational amplifier, which has a theoretically typical input voltage noise about $0.85\,\mathrm{nV}/\sqrt{\mathrm{Hz}}$ at 1 kHz. A simulated and a measured transfer function of the band-pass filter can be found in Figure 3.7. They fit well together for phase and magnitude. While considering very low noise signals in this frequency band, this band-pass filter helps significantly to not reach the dark noise limit of the signal analyzer [the SR785 again]. The AC filtered signals of one stage (four photodiodes) can be measured with a D-Sub-9 connector and they are also sent to a summation point with a gain of 7.1 dB, consisting of an OP27 operational amplifier. The gain is chosen accordingly so that for a desired DC operating point of 10 V per photodiode the DC voltage behind the summation point has a value of 9.1 V and is close to it. The resulting sum signal can be measured by an SMA connector for each stage.

All connectors besides the one for the power supply are attached to the front side of the TIA-box. A similar electronic circuit was already employed in [Kwe10].
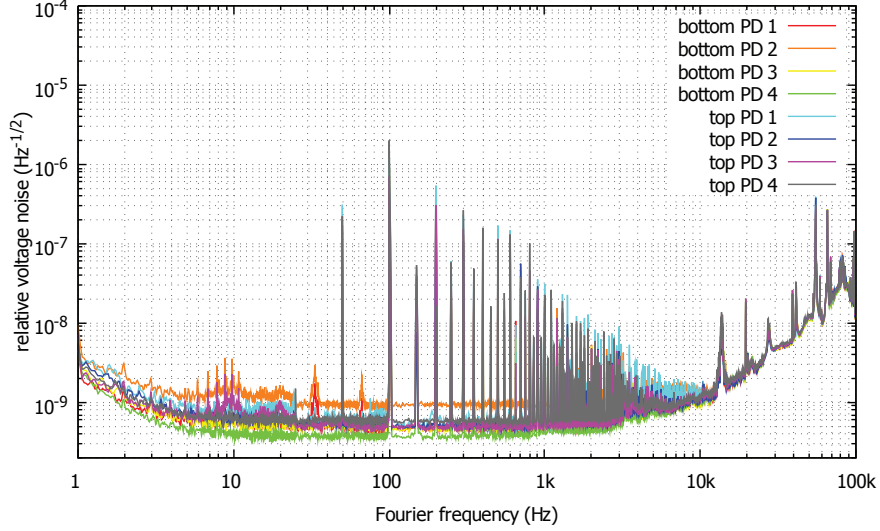
Figure 3.8: Here the measured dark noise of all eight photodiodes are shown. The curves are normalized with the desired DC voltage of $10\,\mathrm{V}$ so that they can be compared to other relative noise graphs. The dark noise of the photodiodes contains numerous additional peaks at higher orders of the supply frequency, which probably originate from the TIA-electronics. Again peaks can be observed with a frequency of about $19.5\,\mathrm{kHz}$ and multiples of them originating from couplings from the band-pass filter.

With the readout electronics, the photodiodes can be characterized further. The important measurement at this point is the comparison of the dark noise of every single photodiode. This measurement, shown in Figure 3.8, was executed with applied bias voltage and covered photodiodes. All the spectra are normalized with $10\,\mathrm{V}$, which is the desired DC operating point later. All curves have a very low noise level and thus allow a power stabilization performance which reaches the $10^{-9}\,\mathrm{Hz}^{-1/2}$ region. They look very similar to each other, so that it can be assumed that all photodiodes are working properly.

3.1.3.2 Feedback Control Filter

The feedback control filter used for this experiment is described in this section. It is a modified version of the aLIGO PSL ISS control filter (device number T0900631). It contains two D-Sub-9 input connectors to control the device by applying constant voltages. They are fed into instrumentation amplifiers AD620 to generate voltages with reference to the board ground potential. The needed input offset-signals are generated by a self-made offset box (a picture of it can be found in Fig. A.1 in the appendix), and at the AEI $10\,\mathrm{m}$ Prototype they will be produced by the control and data system (CDS) (see Sec. 4.1.2). Additionally, three D-Sub-9 output connectors exist to monitor important signals later with the CDS. All other inputs and outputs are LEMO connectors. The main signal path is depicted in Figure 3.9 in a simplified block diagram. For the experiment the two voltages coming from the summation of the TIA for the top and the bottom stage have to be connected to the *Photodiode A* and *Photodiode B* inputs of the ISS board. The board

allows to pipe these signals through and to measure them behind a buffer amplifier. An electric analog switch selects the in-loop signal which is used at the summation point where a reference voltage is added. The other one is the out-of-loop signal and is needed to characterize the achieved stabilization performance. The reference voltage has to be very low-noise in order to not limit the power stabilization. Therefore, the DC voltage is sent to a low-pass filter with a cutoff frequency of 100 mHz to attenuate higher Fourier frequencies. Here other filter mechanisms can be used to reduce the noise of the important reference voltage further. One possibility is to take an active second-order Sallen-Key low-pass filter as was done in [Sei10], instead. In the experiment for this thesis, however, the reference voltage appeared to be no limitation for the power stabilization. Behind the summation point an error signal is generated. It can be measured and controlled via the *Output B* connector. This voltage clearly indicates if the power stabilization is running with good performance and is not oscillating. The reference voltage should be similar to the average value of the summation signal coming from the TIA. Otherwise range problems with the actuator could appear because the feedback control filter is always guided to the reference value and holds the average error point at 0 V.
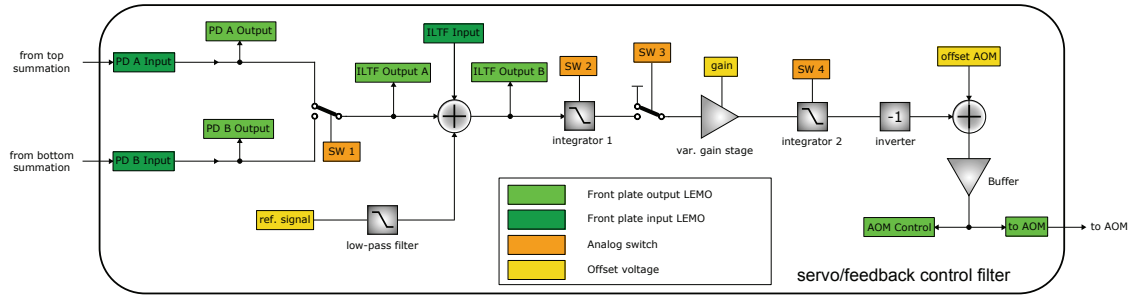

Figure 3.9: Block diagram of the feedback control filter. The integrator 1 was not used during the power stabilization in the laboratory and was bypassed.

After the summation with the reference from the TIA, the signal is sent to an active low-pass filter with a cutoff frequency of about 10 kHz. The filter can be converted to a first integrator (integrator 1) by an electric analog switch. For the setup in the laboratory, this integrator was not necessary; hence the capacitor was removed to only have an 1:1 amplifier. At the AEI 10 m Prototype, this integrator was needed because problems arose with the laser power amplification stage. This component has a larger RPN than the NPRO that is used here, and its transfer function was not as uniform as needed. (see Sec. 4 for detailed informations).

The next element in the signal path is a variable gain stage mainly consisting of an AD603 operational amplifier. It allows to manipulate the gain from -8 dB to 34 dB with a bandwidth of some ten megahertz. The magnification is controlled by another offset voltage lying between -1 V and 1 V. When this voltage is equal to 0 the gain is approximately 11.5 dB. This variable gain stage is very useful when undertaking fast gain modifications. Behind this gain stage a second low-pass filter with an integrator possibility (integrator 2) is connected to the setup. The cutoff frequency of the integrator 2 is about 16 kHz

during the experiment in the laboratory and about 160 kHz when working at the AEI 10 m Prototype in combination with the other integrator. The next element is an optional inverter, which can be bypassed by a manual switch. Behind it, the offset value for the AOM is added at a second summation point. This value determines the operation point of the AOM, which is always desired to remain on the linear slope of the diffraction efficiency curve. In this point the controller has the highest sensitivity and the best range. Finally, a high speed buffer generates the voltage applied to the *to AOM* output. This device is intended to amplify the output current and improves capacitive load drive. It protects the loop from thermal feedback problems. The voltage on the *to AOM* output is applied directly to the AOM driver unit. The intensity of the light can be modulated using the AOM, closing the control loop. The loop can be opened and closed manually by an electric analog switch. All mentioned electric analog switches are from the line DG417-DG419 and have a fast switching time of about 200 ns, thus a bandwidth of at least several megahertz. All electronic elements, like the summation points and the integrators, are built by OP27 operational amplifiers. Test points are installed on different places of the board to monitor the voltages.
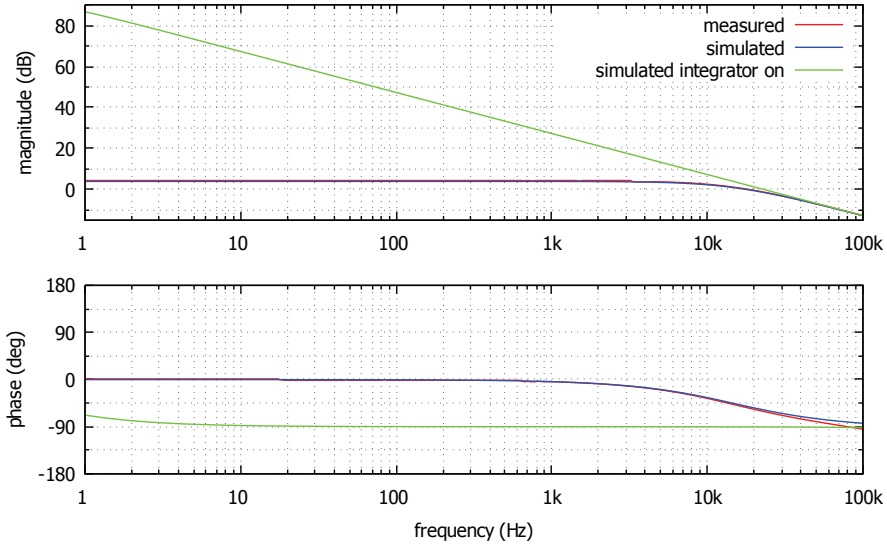

Figure 3.10: Measured and simulated transfer functions of the feedback control filter. Without integrator 2, both the red and the blue line are matching well. When activating integrator 2, the simulation predicts the green graph.

The whole feedback control filter can be characterized by measuring and simulating the transfer function which was done in Figure 3.10. At lower frequencies the transfer function is flat at a level of 4 dB until the region of the cutoff frequency at 16 kHz and then drops down. With an activated integrator, a gain up to 87 dB at 1 Hz can be achieved.

3.2   Pointing Modulations with the Piezoelectric Element

As already mentioned and shown in Figure 3.1 and in Figure 3.2, a deflecting mirror is mounted on a piezoelectric element. With the help of this, pointing fluctuations could easily be induced in two axes (x and y). The position of the piezoelectric element is about 40.5 cm in front of the entrance of the photodiode array, and about 54.5 cm to 59 cm in front of the eight photodiodes. The piezoelectric element has a resonance frequency of 2.7 kHz, so the chosen modulation frequencies are several hundred hertz. To characterize the photodiodes, a transfer function from the piezoelectric element to the AC channel of the TIA was measured. The measurement is plotted in Figure 3.11, and was done for the x and the y axes in a frequency range between 1 Hz and 2 kHz. All photodiodes show a flat behavior up to at least 2 kHz.
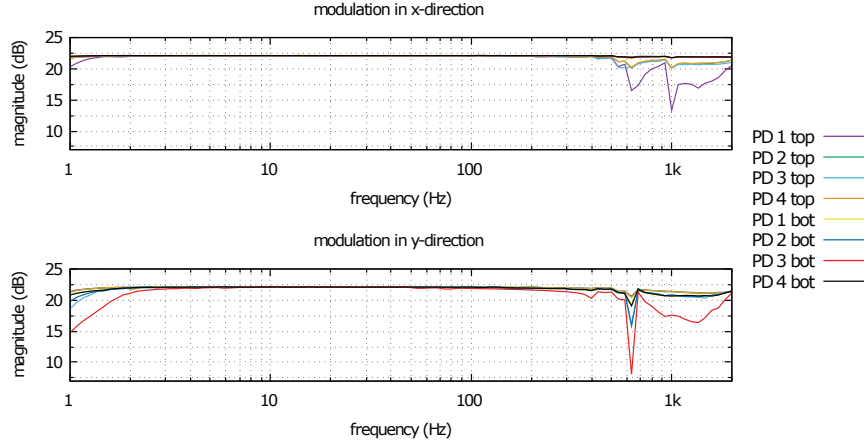
Figure 3.11: Here the transfer function from a piezoelectric element modulation to the TIA, including the band-pass filter, is plotted. All photodiodes behave very similar in respect to pointing.

All eight photodiodes show a very similar free-running RPN, equivalent to the measurement pictured in Figure 3.4. After inspecting the photodiodes and the electronics and ensuring everything was working properly, the first laser power stabilization could be set up. The simplest configuration would be to use only one photodiode as sensor, take the band-pass filtered signal of the TIA and apply the voltage into the feedback control filter. The first power stabilizations were set up without the integrators in a simple way to exclude fundamental errors. The open loop gain transfer function has an open loop gain of only 30 dB at 200 Hz. When the control loop filter works correctly, the size of the RPN is suppressed by the open loop gain, (see Sec. 2.3). The level of the free-running RPN already shown in Figure 3.4 explains why a relative shot noise of a few $10^{-9}\,\mathrm{Hz}^{-1/2}$ is not reachable: The open loop gain within this setup was too small. To achieve an RPN of $2 \times 10^{-9}\,\mathrm{Hz}^{-1/2}$ at 200 Hz, at least three orders of magnitude have to be suppressed, for lower frequencies even more. Hence at least one integrator is essential. To consider all eight photodiodes independently from each other, every photodiode is taken once as an in-loop sensor, while the other seven are observed as out-of-loop sensors. Sixty-four measurements were done

for a complete characterization. As an extract Figure 3.12 shows eight measurements in which the second photodiode from the top stage (PD 2 top) was taken as in-loop sensor. Here the RPN is plotted over the Fourier frequency. Five of the seven out-of-loop sensors approached the relative shot noise region drawn by the black line that corresponds to a level of about $5.0 \times 10^{-9}\,\mathrm{Hz}^{-1/2}$. As an estimate, this relative shot noise was calculated with Equation 2.60 by inserting an average photocurrent of about $I_{\mathrm{il}} = I_{\mathrm{ool}} = 26.1\,\mathrm{mA}$, corresponding to a power of about $33\,\mathrm{mW}$ on the out-of-loop and on the in-loop sensor. The value is only $4.2\,\%$ lower when using Equation 2.56 and inserting the powers.

During the measurement, it was observed that the first photodiode of the top stage (PD 1 top) and the third photodiode of the bottom stage (PD 3 bot) seemed to have some sort of malfunction. On average, every photodiode detected roughly $34\,\mathrm{mW}$ of power, with a deviation of at most $9\,\%$. Remarkably PD 3 bot detected only a power of about $23\,\mathrm{mW}$. This matches with the stabilization limits for this photodiode in Figure 3.12. The measurement could be reproduced by interchanging PD 2 top with another photodiode that showed no problems. When taking PD 1 top as the in-loop sensor, all other photodiodes besides PD 3 bot, which was even worse, were limited by the typical broad noisy behavior of this photodiode. Therefore the relative shot noise could only be achieved in a small frequency region around $2\,\mathrm{kHz}$. When taking PD 3 bot as in-loop sensor, the seven other photodiodes showed the RPN from PD 3 bot. They were all at least one magnitude larger than the drawn relative shot noise.
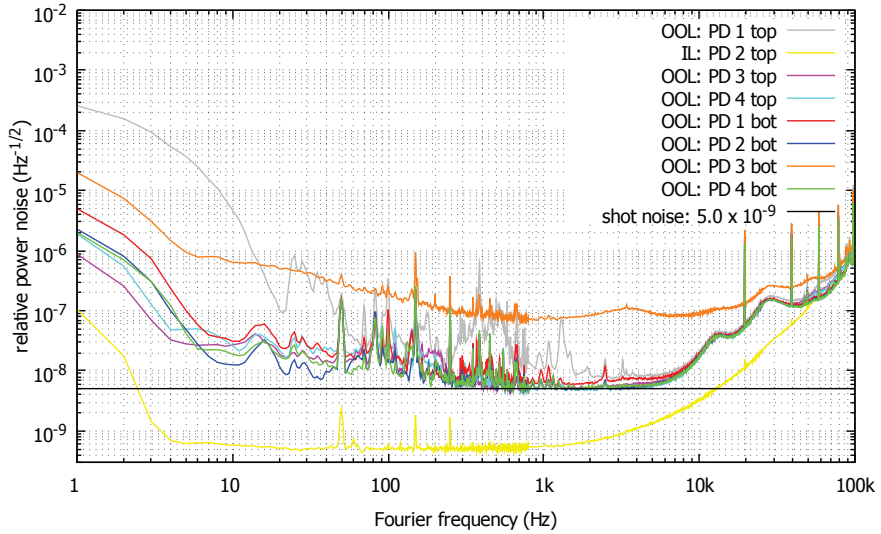

Figure 3.12: The results of the power stabilization built up with the PD 2 top (yellow graph) as in-loop sensor are shown here. While five photodiodes behave very similar and their RPN approaches the black constant relative shot noise line, two photodiodes seem to have problems. The drawn constant relative shot noise graph is at $5.0 \times 10^{-9}\,\mathrm{Hz}^{-1/2}$.

3.2.1   Improvement of the Alignment

With the limitation of the two mentioned photodiodes (PD 1 top and PD 3 bot), it was impossible to build up a stabilization by using the sum of four signals as in-loop and as out-of-loop sensors respectively. However, by taking only the six apparently working photodiodes, i.e. the sum of three at a time, a shot noise limited stabilization was built up achieving an RPN level of about $3 \times 10^{-9}\,\mathrm{Hz}^{-1/2}$. However, this was only achieved for a small frequency range above $1\,\mathrm{kHz}$. Different investigations located the limitation in misalignment of the beams hitting the photodiodes. In works like [Kwe05], misalignments led to similar problems. It became apparent that the photodiodes were not hit on their most sensitive spot by the laser beam, which then maximized pointing coupling into laser power fluctuations. Furthermore, a lot of light was clipping at the aluminum lens cases horizontally and produced a remarkable amount of stray light. To alleviate these issues as much as possible, a new alignment was set up and is described by the following listing:

1. The beam was aligned into the array using the two deflecting mirrors so that the entrance is hit centrally in x and in y direction. Besides that, the eight beams traveling to the photodiodes should be symmetric in horizontal direction, so that clipping on the aluminum lens cases is minimized. Optimally, the beams reach the center of the circle where each photodiode is attached, but they do not necessarily hit the exact center of the sensitive area.
   This approach was observed through an infrared viewer and with an infrared sensor card.

2. Every single photodiode was removed from the backside of the photodiode array and realigned. The piezoelectric element was then fed by two different modulation frequencies for x and y direction, for example by $130\,\mathrm{Hz}$ and $200\,\mathrm{Hz}$. Now, the AC and the DC content of the DC-readout channel signal of the TIA element of the photodiode could be observed and adjusted using an oscilloscope. The alignment was finished when the AC amplitude was minimized and when the double modulation frequency could be detected in both displacement directions, respectively. In the array, a photodiode is significantly more sensitive to beam pointing in x direction due to the $45\,^\circ$ incidence angle.
   After conducting these steps, the laser beam hits the photodiode on the most sensitive position. Usually, the DC value is at its maximum then, too.

With the help of this method, every photodiode was shifted and realigned. The clipping on the aluminum lens cases was still a problem, however it has been minimized. After the improvement of the alignment a laser power stabilization with one photodiode was set up again, resulting in the same sixty-four measurements as above to characterize all photodiodes. As an extract Figure 3.13 again shows the RPN when PD 2 top is taken as in-loop sensor. Now the two apparently malfunctioning photodiodes PD 1 top and PD 3 bot are measuring a similar RPN as the other five photodiodes. The graphs are shot noise limited between several hundred hertz and a few kilohertz. The total light detection of all photodiodes is increased by $10\,\%$ after the realignment. The power going into the photodiode array was unchanged. Now, on average each photodiode detects a power of
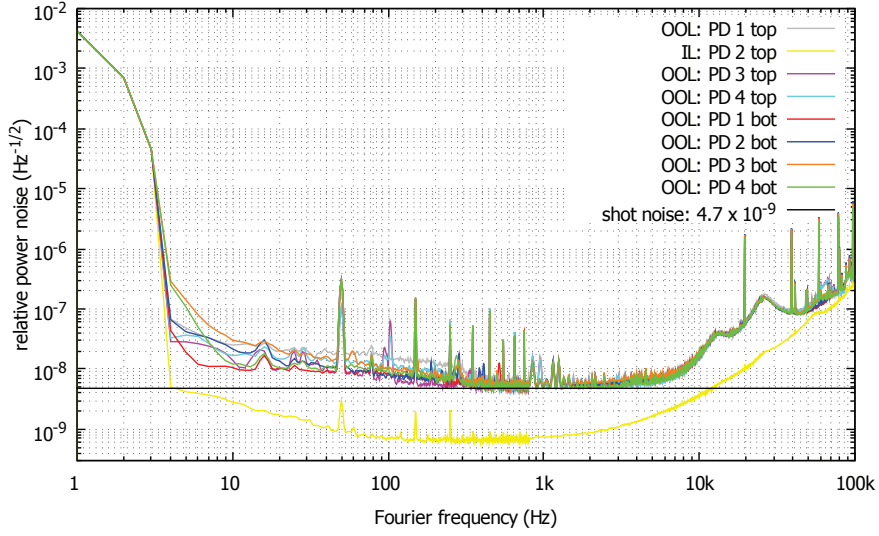
Figure 3.13: Results of the laser power stabilization after the improvement of the alignment. Here PD 2 top is taken as in-loop sensor again. The constant relative shot noise lies at $4.7 \times 10^{-9} \, \mathrm{Hz}^{-1/2}$ and corresponds to a detected power of about $37.5 \, \mathrm{mW}$ on the in-loop and out-of-loop sensor respectively.

about $37.5 \, \mathrm{mW}$.

Finally, the coupling from beam pointing into additional power noise could be reduced to a minimum. This could be confirmed by comparing the stabilization performance between this assumed optimal alignment and an induced permanent displacement (see Sec. 3.3). Now a laser power stabilization with significantly more total detected power could be set up. This is described in the following section.

3.3   Performance of the Power Stabilization in the Laboratory

Finally, a laser power stabilization using all eight photodiodes was established. The sum of four photodiodes for each stage is taken as in-loop and as out-of-loop signal, respectively. First, the open loop transfer function of the closed control loop can be observed in Figure 3.14. This function characterizes the magnitude of a potential noise suppression by showing the open loop gain. If there are no other limitations the RPN measured by the in-loop detector is suppressed by exactly this gain value. The open loop gain is given by $92 \, \mathrm{dB} \pm 5 \, \mathrm{dB}$ at $10 \, \mathrm{Hz}$ and decreases for higher frequencies. At $100 \, \mathrm{Hz}$ this value is $83 \, \mathrm{dB} \pm 5 \, \mathrm{dB}$ and at $1 \, \mathrm{kHz}$ the open loop gain contributes to $72 \, \mathrm{dB} \pm 4 \, \mathrm{dB}$.

It can be estimated that the unity gain frequency, which was already mentioned in Section 2.3.2, is $150 \, \mathrm{kHz} \pm 10 \, \mathrm{kHz}$. The phase margin can be estimated to be $11° \pm 3°$, which means that the stabilization is barely convergent. The control loop becomes instable when acoustic disturbances get too large in the laboratory; however, a long term stability (tested up to $24 \, \mathrm{h}$) is given when the system is held quiet. Therefore, this low phase margin is not seen as a problem, especially as the vacuum tank the setup will be placed into will isolate it acoustically. However, the actual performance of the power stabilization can only be
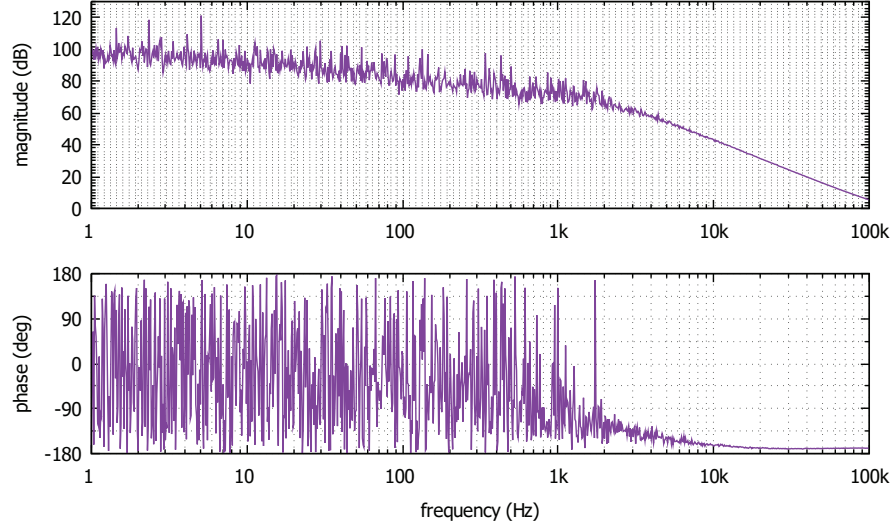
Figure 3.14: Measured open loop transfer function during the laser power stabilization while the sum of four photodiodes is used as in-loop sensor. The measurement was done with a swept sine signal that had an amplitude of 1 V. The high gain values for lower frequencies originates from the integrator 2. The phase is very noisy for frequencies up to 1 kHz, although there is no obvious explanation for this.

considered by measuring the RPN on the out-of-loop sensor. Figure 3.15 shows a complete plot of all relevant graphs. In this evaluation, the sum of the four top photodiodes is taken as in-loop sensor and the bottom stage is used as out-of-loop sensor. When interchanging the two stages, the measurements look very similar. The DC values and the corresponding optical powers on the photodiodes are written down in Table 3.1.

Overall, a total power of 140.8 mW $\pm$ 1 mW is detected by the in-loop sensor and 158.6 mW $\pm$ 1 mW is detected by the out-of-loop sensor. The total power going into the photodiode array is 299.4 mW $\pm$ 2 mW. In a steady state configuration, the measurement uncertainties for these values are only a few milliwatt mainly due to drifts in the offset value of the AOM. The corresponding photocurrents are 111.2 mA $\pm$ 1 mA for the in-loop sensor and

Table 3.1: Summary of the DC values of the eight photodiodes. While the voltages are measured with an oscilloscope, the powers are calculated assuming ideal electronics and a quantum efficiency of $\eta = 0.92$ of the photodiodes.

top	PD 1	PD 2	PD 3	PD 4	sum	mean
voltage [V]	-7.95	-7.31	-7.56	-8.50	31.32	7.83
power [mW]	40.3	37.0	38.3	43.0	158.6	39.65

bot	PD 1	PD 2	PD 3	PD 4	sum	mean
voltage [V]	-7.06	-6.50	-6.94	-7.32	27.83	6.96
power [mW]	35.7	32.9	35.1	37.1	140.8	35.22

$125.3\,\text{mA} \pm 1\,\text{mA}$ for the out-of-loop sensor. This results in a relative shot noise limit which is defined by Equation 2.60 and has a value of $2.33 \times 10^{-9}\,\text{Hz}^{-1/2}$, represented by the black constant line in Figure 3.15. Again, the free-running laser noise is plotted for the two sum signals, which are very similar. This was done to compare the power noise before and after the stabilization, and to see by how many orders of the magnitude the RPN is suppressed. This curve is similar to the one already shown in Figure 3.4, but does not contain the high electronic resonances at $19.5\,\text{kHz}$ and multiples of it.
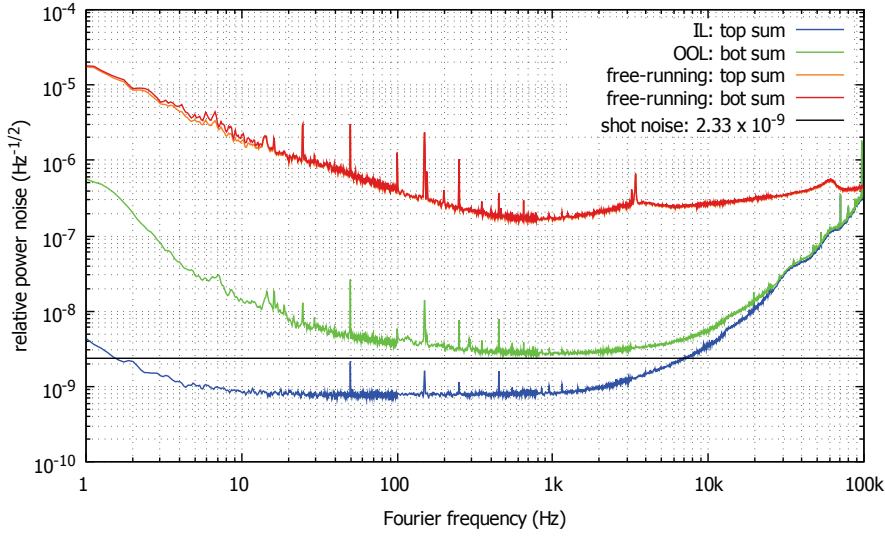
Figure 3.15: Final results of the power stabilization experiment in the laboratory. Here the RPN for different measurements is plotted. The red and the orange graphs show the free-running laser noise, which is measured by the sum of the top and the bottom stage. The green graph characterizes the out-of-loop power noise and converges to the constant black relative shot noise line for frequencies between several hundred hertz and $2\,\text{kHz}$. The in-loop power noise is represented by the blue graph, falling below the relative shot noise level for frequencies between about $1.5\,\text{Hz}$ and $7.2\,\text{kHz}$. It falls to a constant level of about $7.5 \times 10^{-10}\,\text{Hz}^{-1/2}$ for frequencies larger than $10\,\text{Hz}$ over two decades.

To achieve the best performance, it should be ensured that some obvious issues are avoided. One main trouble was the misalignment of the photodiodes, which was described in Section 3.2.1. The cabling of all electronics has to be done carefully to reduce possible ground loops and electric resonances as these would generate numerous peaks in the RPN spectrum in the hundreds of hertz regime. The flowbox on the breadboard as well as the light of the ceiling lamps have to be shut down during the measurements. Otherwise these influences would generate several issues and limit the power stabilization at low frequencies smaller than about $200\,\text{Hz}$. There the RPN would be up to a factor of four worse than the presented one in Figure 3.15. It should be ensured that the laser works in a steady state, which means that it is in a long term operation cycle to avoid drifts during the measurements. This also applies to the electronic devices to achieve a thermal equilibrium.

3.3.1   Limitations

In Section 2.4 several limitations coming from different sources are already mentioned. With the presented laser power stabilization an RPN of $(2.7 \pm 0.1) \times 10^{-9}\,\mathrm{Hz}^{-1/2}$ was achieved for frequencies between about $600\,\mathrm{Hz}$ and $1.5\,\mathrm{kHz}$. This value lies about $1.3\,\mathrm{dB}$ above the corresponding relative shot noise level for the amount of power used.

For frequencies between $2\,\mathrm{kHz}$ and several ten kilohertz, where the in-loop and the out-of-loop graph in Figure 3.15 are not matching, additional noise is seen on the out-of-loop sensor. The origin of this effect is unknown. For smaller frequencies below $700\,\mathrm{Hz}$, the RPN on the out-of-loop sensor deviates further from the relative shot noise. In this frequency region, different problems may limit the power stabilization.

Fluctuations of the laser polarization could couple in power noise due to polarization-dependent behavior of optical components. Furthermore, the responsivity of the photodiodes could be changed by polarization fluctuations causing power noise. For this experiment however, it is not probable that this is the limiting noise source at low frequencies.

Another factor can be scattered light of different origins. It could arise from the already mentioned clipping that definitely exists due to the light clipping on the aluminum lens cases. Other scattered light could originate from reflecting light on e.g. lens or aluminum surfaces in the array. Light which is reflected multiple times in optical components, like in beam splitters, could interfere with the original laser beam and produce laser power noise, too. All these effects occur at lower frequencies, particularly due to mechanical resonances, which could be amplified by acoustic waves and influence the components. Furthermore, in the laboratory environment dust particles in the air passing through the laser beam prevent an RPN suppression in the desired region for frequencies lower than a few hertz. The main problem though probably arises from pointing jitter that couples into power noise and thus limits the stabilization performance. In combination with an inhomogeneous responsivity of the photodiodes, it can produce additional noise directly on the out-of-loop sensor. This effect of an inhomogeneous responsivity of photodiodes was already more precisely observed in other experiments, as documented in [Kwe05] or [Wei15]. When the in-loop sensor detects this power noise induced by pointing jitter, it is imprinted on the laser beam by the control loop resulting in extra noise. With aligned and calibrated quadrant photodiodes, a displacement fluctuation on the order of $\pm 1\,\mathrm{\mu m}$ was observed. Mechanical resonances may amplify these effects further.

When stabilizing the laser power in a vacuum tank, it is assumed that less noise is coming from the potential noise sources. The amount of dust particles is strongly reduced, and problems originating from acoustic waves are avoided. However, the power noise on the out-of-loop sensor could be shot noise limited for a frequency around $200\,\mathrm{Hz}$, or even lower when running the experiment in the vacuum tank. In that case it could be attainable to achieve an RPN of $2 \times 10^{-9}\,\mathrm{Hz}^{-1/2}$ at this frequency, which is the goal of this experiment. The existence of the peaks at multiples of power supply frequencies that appear in the out-of-loop spectrum arise from electrical issues. Ground loops could increase this effect, so care was taken to avoid these loops by connecting and isolating the electronics properly. The usage of low noise battery packs for the power supply of all electrical devices could reduce these peaks further.

The speed of the control loop can be characterized by the unity gain frequency, which has a value of about 150 kHz in this experiment. The speed is sufficient for the requirements at the AEI 10 m Prototype. This value can be increased by enhancing the gain with faster electrical gain stages. However, this would lead to the speed of the control loop being limited by the AOM in the first instance. This device has a transfer function with a flat magnitude up to about 400 kHz, decreasing at higher frequencies. At these frequencies, the phase loss would be a problem which cannot be compensated.

3.4 Preparation for the Transfer and Summary of the Experiment

In the context of this thesis, a laser power stabilization preparation experiment was built up in a separate laboratory. All required components, like optics and electronics, were tested and optimized in order to be able to at least replicate the performance in the vacuum tank at the AEI 10 m Prototype. Due to the fact that piezoelectric elements on deflecting mirrors are not placed in the tank, the well aligned beam has to be copied from the laboratory. This needs to be done in order to reduce the coupling from beam pointing jitter into laser power noise, and is monitored by observing the differential voltage values on the two quadrant photodiodes. Essentially the beam should enter the photodiode array very centrally. Later, when the laser beam with all its parameters is reproduced successfully, the relation in the eight DC voltages for the photodiodes would be the same as in the laboratory. In the end of this chapter, a very short summary by means of Table 3.2 shows the most important parameters.

Table 3.2: Summary of the most important parameters characterizing the laser power stabilization in the laboratory.

Parameter	Value
power on the il sensor	$158.6 \,\mathrm{mW} \pm 1 \,\mathrm{mW}$
power on the ool sensor	$140.8 \,\mathrm{mW} \pm 1 \,\mathrm{mW}$
corresponding relative shot noise	$2.33 \times 10^{-9} \,\mathrm{Hz}^{-1/2}$
RPN @200 Hz on the ool sensor	$(3.2 \pm 0.2) \times 10^{-9} \,\mathrm{Hz}^{-1/2}$
RPN @1 kHz on the ool sensor	$(2.7 \pm 0.1) \times 10^{-9} \,\mathrm{Hz}^{-1/2}$
unity gain frequency	$150 \,\mathrm{kHz} \pm 10 \,\mathrm{kHz}$

The outstanding feature of the presented experiment is that it achieved the RPN of about $2.7 \times 10^{-9} \,\mathrm{Hz}^{-1/2}$ in normal laboratory conditions outside a vacuum. For better comparison to other experiments, the value at 100 Hz is important, which is approximately $3.7 \times 10^{-8} \,\mathrm{Hz}^{-1/2}$.

There are only a few experiments that reached a similar performance for a laser power stabilization in this frequency range. Most of them are operating in a vacuum tank, and they are compared in Section 4.3. In non-vacuum environments B. Barr, K. Strain and C. Killow achieved an RPN of about $2 \times 10^{-8} \,\mathrm{Hz}^{-1/2}$ at 100 Hz [Bar05] as well as F. Nocera [Noc04], C. Bogan [Bog13] or J. Põld [Põl14]. J. Rollins et al. reached a performance of about $3.5 \times 10^{-9} \,\mathrm{Hz}^{-1/2}$ [Rol04] at 100 Hz.

Implementation in the AEI 10 m Prototype

In this chapter, the experimental realization of the power stabilization at the AEI 10 m Prototype will be presented. The AEI 10 m Prototype is an outstanding experiment currently being set up at the Max Planck Institute for Gravitational Physics (AEI). It will be used to test and develop further techniques for gravitational wave interferometers. This experiment is described and characterized here in general. The characteristics of individual subsystems will be shown as well. The specific setup developed in the context of laser stabilization set up at the AEI 10 m Prototype is described and explained in this chapter in detail. In comparison to the preparation experiment in the laboratory depicted in Chapter 3, some differences occurred, which will be discussed here. These discrepancies resulted in some additional problems in the experiment, e.g. originating from the new laser source. Eventually, these problems were solved and a power stabilization scheme was implemented that is shot noise limited for frequencies at around 200 Hz and 1 kHz. In this chapter, the results are illustrated and remaining possible limitations at lower frequencies are pointed out. Finally, the most important resulting parameters are summarized and the result is put into context with other current experiments.

4.1 The AEI 10 m Prototype

The AEI 10 m Prototype consists of a Michelson interferometer which is set up in a vacuum tank. With its arm length of 10 m it belongs to the smaller scale interferometer prototypes. These experiments played a very important role to the successful construction of the first generation gravitational wave detectors. Furthermore, second generation observatories like Advanced LIGO (aLIGO) [Har10], which began observations in 2015, could increase their sensitivity. This was possible because of the knowledge that was obtained on the small scale interferometers. The corresponding upgrading process at a large scale interferometer like GEO 600 is e.g. described in publication [Lüc10]. The usage of second generation gravitational wave detectors led to the first detection of gravitational waves with earth-bound detectors [Abb16] in September 2015. In the future, third generation observatories like the ET [Pun10] will be developed to improve the sensitivity further on. The first goal of this experiment was to achieve the SQL of interferometry (see Sec. 2.2.4). The sensitivity level is intended to be limited by photon shot noise and by radiation pressure noise around 200 Hz. Furthermore, the experiment proposes to develop techniques that are aiming

for quantum noise reduction, for example with squeezed light injection. Therefore, the interferometer is also referred to as a sub-SQL interferometer. Another goal is to measure quantum radiation pressure noise directly related to the generation of ponderomotive squeezing [Cor06]. In addition, when achieving the sensitivity level below the SQL the interferometer mirrors can be described by quantum states, resulting in macroscopically entangled test masses.
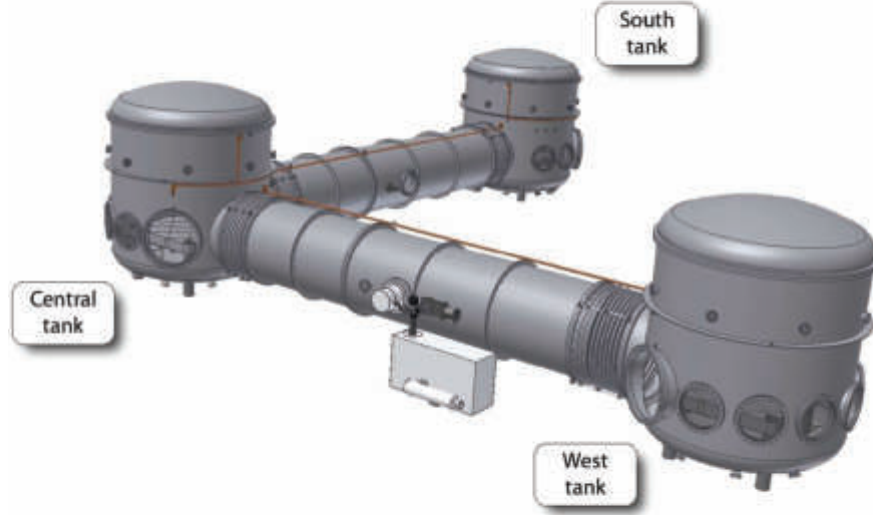

Figure 4.1: Technical drawing of the AEI 10 m Prototype vacuum system. Adapted from [Grä13].

The AEI 10 m Prototype experiment is located in a laboratory hall associated with the Albert Einstein Institute, Hannover. A technical drawing of the vacuum tank is shown in Figure 4.1. It can be seen that the three main tanks, built of stainless steel, have a geometric diameter of 3 m, and a height of 3.4 m. The central tank is connected to the south and the west tank with two 1.5 m diameter tubes. The installation of the system was completed in February 2009. Overall, the volume of the tank is about $100 \, \text{m}^3$ and the total weight is approximately 22 t.

To generate the desired vacuum, an array of pumps is used to achieve a pressure of $(2\pm0.2)\times10^{-2}$ mbar after two hours of pumping. This value decreases to $(1\pm0.1)\times10^{-6}$ mbar after three days and to $(8 \pm 0.1) \times 10^{-7}$ mbar after one week of pumping.

When working with high-precision laser interferometric experiments the limiting noise source at low frequencies below 10 Hz is seismic noise [Grä13]. This kind of noise originates mainly from plate tectonics shaking the ground permanently; this tectonic motion couples into optical elements if they are not sufficiently isolated. At the AEI 10 m Prototype a seismic isolation system is used that is based on the LIGO seismic attenuation system (SAS) [Wan12] and is now called AEI-SAS. It combines two passive isolation techniques, the geometric anti-spring (GAS) filters [Ber99] and the inverted pendulum (IP) legs [Tak07]. Due to the isolation techniques, the optical bench with a size of 1.75 m × 1.75 m is isolated

in all six degrees of freedom. Each of the three tables in the connected vacuum tanks has a weight of about 950 kg and can be balanced by distributing ballast weight on the optical bench. If new payload is placed on the area, the weights are removed or redistributed as necessary. For further information about the seismic isolation of the AEI 10 m Prototype, see [Wan13].

Another feature of the AEI 10 m Prototype is the suspension platform interferometer (SPI). It actively suppresses the relative motion of the optical benches interferometrically, and thus measures the distance to the south and the west table relative to the central table. An experimental setup of the SPI can be found in the publication [Dah12b]. The desired aim of the SPI is stated as having relative changes in distance that are smaller than $10^{-10} \, \mathrm{m \, Hz^{-1/2}}$ and angular fluctuations that are less than $10^{-8} \, \mathrm{rad \, Hz^{-1/2}}$ for frequencies between 100 mHz to 100 Hz [Grä13].

In the past it was also planned as an expedient environment to test techniques for space interferometry experiments like the GRACE follow-on mission [Deh09; Fle15], which was later canceled. Further details about the SPI are summarized in [Dah12a].

To improve the frequency stability of the laser system (see Sec. 4.1.1), a frequency reference cavity is used. Two planar and one curved mirror form a cavity with a round-trip length of 21.2 m. This cavity has a calculated finesse of $\mathcal{F} = 3580$ and with the aid of this cavity higher order modes are suppressed by a factor of rougly $\gtrsim 1000$ for modes up to the sixth order [Grä13]. Each mirror has a weight of 850 g and is suspended to reduce the coupling of seismic noise. Horizontal isolation can be achieved by multiple cascaded steel wire pendulum stages that are attenuated at their resonance frequencies. Vertical isolation is provided by the usage of blade springs.

To achieve the desired low noise in the laser's frequency, the Pound–Drever–Hall (PDH) technique [Dre83] is employed. The reference frequency required for this technique is taken from the reference cavity. Because the resonance frequency in an optical resonator only depends on the length of it, a length signal is obtained and is then used as feedback to the main laser frequency. Due to the fact that the resonance is symmetric to this frequency, an electro-optic modulator (EOM) imprints off-resonant phase modulation sidebands on the light. The signal that is reflected on the cavity is demodulated to generate an error signal for the laser frequency. The stabilization for frequencies below 1 Hz is done by a thermal actuation of the laser crystal. For the frequency band between 1 Hz and 1 kHz it is realized by mechanical actuation via a piezoelectric element, and for frequencies in the range of 10 kHz to 250 kHz an EOM corrects the phase and in this way reduces the noise of the laser frequency. The result is a desired frequency noise level of about $10^{-4} \, \mathrm{Hz \, Hz^{-1/2}}$ at 20 Hz that decreases to $6 \times 10^{-6} \, \mathrm{Hz \, Hz^{-1/2}}$ above 1 kHz [Grä13]. More details and information about the reference cavity containing explanatory pictures can be found in publications like [Kaw10; Kaw12].

In the following, the two most important subsystems relevant to this project are described. First the attention lies on the main laser system that produces the light power. Then the CDS, which is responsible for all the data acquisition at the AEI 10 m Prototype, will be described.

4.1.1   Laser System

The laser system that is used at the AEI 10 m Prototype is identical to the Enhanced LIGO (eLIGO) laser system [Rie08]. It was developed in cooperation of the Laser Zentrum Hannover (LZH) and the Albert Einstein Institute for the implementation in gravitational wave detectors. For instance, an Enhanced LIGO laser system constitutes the light source in the GEO600 detector in Sarstedt, near Hannover. It consists of the first two stages of the Advanced LIGO (aLIGO) laser system design [Wil08]. Figure 4.2 shows a schematic drawing of the whole system, which is build up in a quadratic aluminum box with a side length of 75 cm to protect the system from external influences.
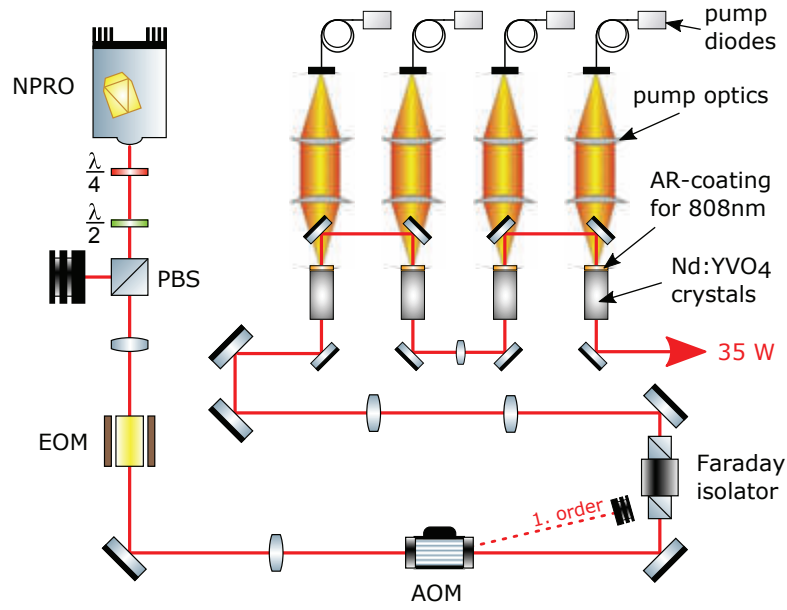
Figure 4.2: Schematic drawing of the 35 W laser system at the AEI 10 m Prototype. The first stage is formed by an NPRO acting as a master laser. After some optical components are implemented the second stage is composed of the amplification stage including four Nd:YVO$_4$ crystals pumped by laser diodes.

The first stage is formed by the master laser, which is a Nd:YAG solid-state laser [Innolight, Mephisto 2000] with an output power of 2 W and a wavelength of 1064 nm. This commercial NPRO laser is similar to the laser that was used in the experiment in Section 3.1.1, but has an approximately four times higher power.

In the beam path behind the NPRO, a $\lambda/4$ and a $\lambda/2$ plate in connection with a PBS are placed to linearize the residual elliptical polarization of the NPRO. With the aid of a first lens, the light is focused into an EOM [New Focus, 4004-M] that is needed to stabilize the mode filter by phase modulating the light. A second lens focuses the light into an AOM [Crystal Technology Inc., AOMO 3080]. This component is needed for the power stabilization experiment, modulating the intensity of the laser beam.

The second stage of the laser system consists of the amplification stage. The laser

beam has to be well aligned to fulfill the geometric requirements and reach optimal amplification. Two further lenses in combination with two deflecting mirrors aid in achieving this. The amplification stage by itself consists of four Nd:YVO$_4$ (neodymium-doped yttrium orthovanadate) crystals in an amplifier configuration. Each crystal is pumped with a 400 μm diameter fiber-coupled laser diode with a nominal power of 45 W [Fre07]. To protect the diodes and thus increase their lifetime, the power during operation is usually kept lower. These diodes are running at a wavelength of 808 nm and increase the total power of the laser system to 35 W. The diode currents can be adjusted individually by the CDS. The emitted light has a fundamental mode ratio of approximately 95 % [Fre07]. Each laser crystal is completed by a dichroic mirror coated with an anti-reflection film for the pump light wavelength to separate pump light and laser light. The wavelength matching between pump light and laser light can be realized by modifying the temperature of the NPRO.

A polarization maintaining photonic crystal fiber (PCF) with a length of 4.5 m guides approximately 10 W into the vacuum tank of the AEI 10 m Prototype. In future experiments, free space couplings of high power lasers are considered due to the limitation of Brillouin scattering inside PCFs, which limits the maximal transmission.

4.1.2 Control and Data System

At the AEI 10 m Prototype, a large amount of data has to be collected. In the vacuum tank, several sensors have to be read out and many actuators have to be controlled. The CDS was developed at LIGO [Bor09] and is implemented at the AEI 10 m Prototype to digitize and collect the produced data. It allows controlling optical components that are interfaced with electronics in a convenient way. It also serves as an acquisition system for other environmental physical parameters like the room temperature, the humidity or the air pressure. All the data is stored in the system for later analysis and is time-stamped with an accuracy of about 1 μs corresponding to a sampling frequency of 65 536 Hz [Grä13]. To achieve this desired time precision, a custom timing system that is based on a 2^{22} Hz master clock synchronized to a Global Positioning System (GPS) 1 Hz clock is employed. In the initial configuration the CDS is responsible for about 500 channels that can be grouped into different categories. For instance this system monitors the automatic beam alignment by comparing the overlap of the cavity eigenmode with the incoming laser beam. For the suspension systems, all relevant mechanical resonances are damped by local control loops. The stabilization of the whole laser system is controlled by the CDS; both the power stabilization with the experiment described here, and the frequency stabilization using the reference cavity and a so-called pre-mode cleaner (PMC) (see Sec. 4.2.1). It also controls the SPI that is read out by a Laser Interferometer Space Antenna (LISA) Pathfinder phasemeter [Ant11; Hei04]. The main interferometer is controlled in its spatial degrees of freedom by the CDS.

The 500 channels form several control loops. They are designed with the software Matlab/Simulink, and are responsible for the digital-to-analog conversion (DAC) as well as the analog-to-digital conversion (ADC) that transform the signals respectively. The software of the CDS is based on a real-time enabled Linux operating system with a specific LIGO-developed patch that is based on a Linux patch. The user interface is based on the

Experimental Physics and Industrial Control System (EPICS) architecture [Exp11]. A screenshot showing the software of the CDS can be found in Figure A.4 in the appendix, showing the window for the power stabilization experiment in the foreground. The full documentation of the CDS from LIGO can be found in [Bor09].

4.2   The Experimental Setup

The experimental realization of the power stabilization is similar to the setup referred to in Section 3.1. A drawing of the setup can be found in Figure 4.3. The laser system, including NPRO, AOM and amplification stage, was already shown in Figure 4.2, and is therefore pictured here in a simplified way. It is placed outside the vacuum tank. As already mentioned, the PCF guides about 10 W of the laser light into the vacuum tank. On the breadboard of the central tank, the light is coupled out. A PMC is placed in the beam path to suppress higher order modes. A more precise characterization of this important component is given in Section 4.2.1. The laser power needed for the power stabilization experiment is transmitted by a following beam splitter. An attenuation stage consisting of a half-wave plate and a PBS serves as a controller for the detected power. During the first experiment the power in the beam path going to the photodiode array was about 320 mW. Two lenses are used to achieve the same geometric parameters of the beam as in the experiment in Chapter 3. L1 has a focal length of $f_1 = 50$ mm and is placed at 51 cm ± 0.5 cm in front of the entrance of the photodiode array. L2 has a focal length of $f_2 = 150$ mm and is located at 20 cm ± 0.5 cm in front of the entrance. With the aid of these lenses, the laser beam from the laboratory experiment can be reproduced in the tank.
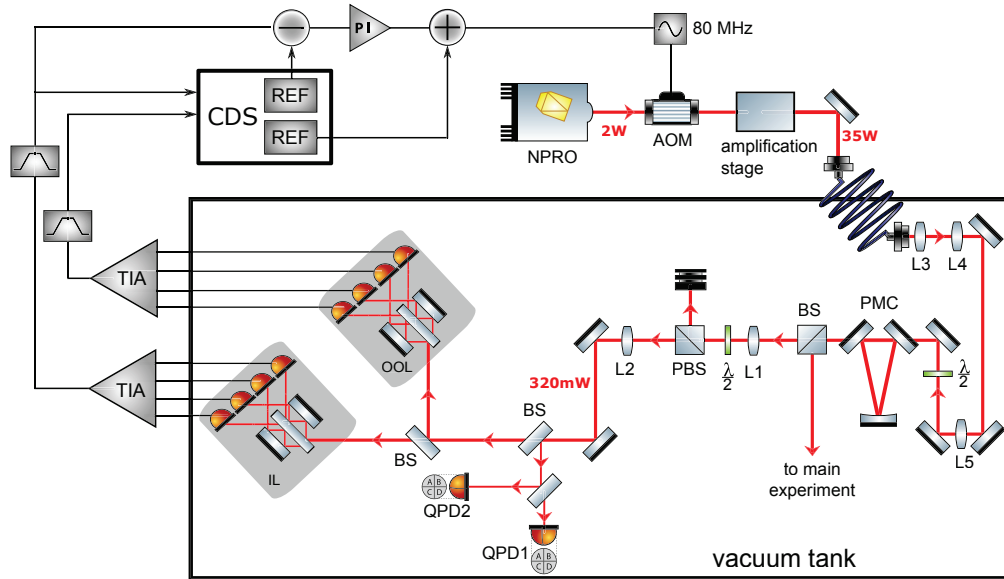
Figure 4.3: Schematic experimental setup at the AEI 10 m Prototype. The NPRO, the AOM and the amplification stage (see Fig. 4.2) are placed outside the vacuum tank. In the tank behind the PMC the setup is similar to the presented one in Section 3.1. The electrical data acquisition is done by the CDS.

As the sensor, the photodiode array is used with the same design as described in Section 3.1.2. The photodiode array has a payload of approximately $3850\,\mathrm{g}$. Due to the same geometric beam parameters as before, all beam radii and Gouy phases are nearly the same. The beam radii on the photodiodes are approximately $250\,\mu\mathrm{m} \pm 70\,\mu\mathrm{m}$. On QPD1 the beam radius has a value of $250\,\mu\mathrm{m} \pm 40\,\mu\mathrm{m}$ and on QPD2 the beam radius is $100\,\mu\mathrm{m} \pm 20\,\mu\mathrm{m}$. The readout electronics of the photodiodes are the same as already explained in Section 3.1.3. The eight photocurrents are transformed by the TIAs, their voltages are band-pass filtered and summed together resulting in the in-loop and the out-of-loop signal.
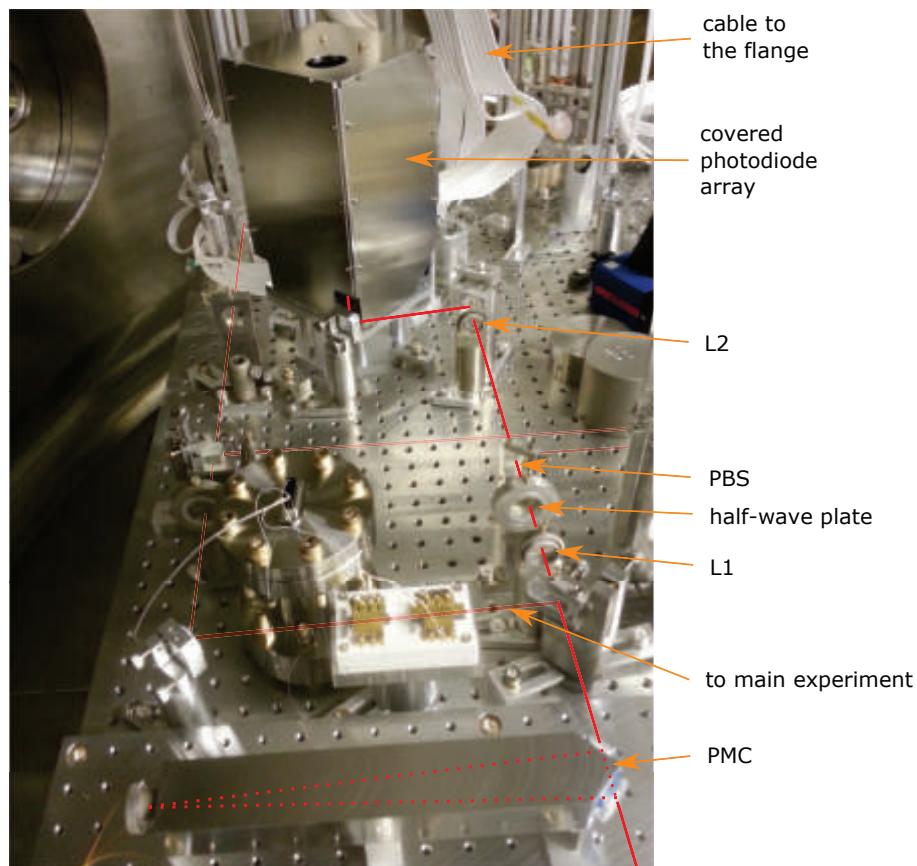
Figure 4.4: Photograph of the optical setup placed in the central tank of the AEI 10 m Prototype. The circulating light in the PMC is drawn by the red dashed line. The white vacuum compatible cable connects photodiodes with the flange of the vacuum tank.

After this identical output in the preparation experiment in the laboratory and at the AEI 10 m Prototype, the continuing data processing is fundamentally different after the in- and out-of-loop signals are detected. The voltages of the in-loop and out-of-loop signals are applied to the CDS of the AEI 10 m Prototype (see Sec. 4.1.2). The data is then digitized for further processing, which in this case is observation over time. With the CDS, reference signals are generated, which are then converted into analog voltages. These analog voltages are going to the summation point of the AOM and of the feedback control

filter, respectively. With another offset voltage, the variable gain stage is fed to modify the total gain of the control filter. Finally, the feedback control filter works with the pure error signal arising from the reference voltage and in-loop voltage. However, the filter itself has to be modified due to different issues at the AEI 10 m Prototype, which are described in Section 4.2.2. This necessary redesign is characterized and clarified in Section 4.2.3 below. The output voltage of the feedback control filter is added to a reference value and the sum is sent to the AOM via the driver unit. At the AEI 10 m Prototype this component is fed with a frequency of 80 MHz. The control loop is closed here and the light power can be regulated. The power that is not needed is diffracted into the first diffraction order of the AOM, directing the excess light into a beam dump. The separation angle is about 20.2 mrad, slightly smaller than in the laboratory due to the lower sound frequency propagating in the crystal.

The main part of the optical setup in the vacuum tank downstream of the PMC is pictured in a photograph in Figure 4.4. Here one can see the PMC on the bottom, followed by the attenuation stage and the two lenses. The light is sent onto two deflecting mirrors to align the beam into the photodiode array, which is shown in the top of the picture. A cover produced of aluminum protects the whole sensor from scattered light from other optical components placed in the vacuum tank in parts not belonging to the power stabilization beam path.

4.2.1 Pre-Mode Cleaner

The pre-mode cleaner (PMC) used at the AEI 10 m Prototype has a triangular shape and consists of two planar mirrors and one curved mirror. The curved mirror has a radius of curvature of 1 m and sits on the top corner of the equilateral triangle. The planar mirrors serve as in- and out-coupling ports. It follows a round-trip length of 53 cm $\pm$ 0.01 cm. The PMC is mounted on the same breadboard as the output coupler of the PCF that is going into the tank. It is a special construction consisting of Super Invar, an alloy that is very robust due to minimal thermal expansion at room temperatures [Hig15]. Additionally, in front of the PMC there are three more deflecting mirrors and three lenses to achieve the desired beam geometry for the resonator. A half-wave plate is located in front of the PMC; however, this is not depicted in Figure 4.3. By means of these optics, the eigenmode of the fiber can be transformed into the eigenmode of the PMC.

The PMC is responsible for suppressing higher order modes of the light, also referred to as geometric filtering. The eigenmode resonating in the cavity is defined by the geometric parameters of the resonator, for instance by the round-trip length and the radii of curvature of the mirrors. This eigenmode is described by the so-called g-factor, with a value of $g = 0.735$ in this case. The suppression of higher modes is specified by this factor and by the finesse which here is $\mathcal{F} = 1000$. The larger the finesse, the better any field amplitudes of higher order modes are suppressed. Although the finesse is desired to be as high as possible, it is limited by thermal overheating of the mirrors leading to self-destruction. For this PMC design, the field amplitudes of higher order modes are suppressed by a factor of 200.

The PMC as a three mirror resonator has further advantages over typical Fabry-Pérot cavities. It not only has a strict polarization dependence due to its odd number of mirrors

and can therefore act as a polarization selective component, but a three mirror resonator also splits the reflected light from the incoming light so that it can be used as an error signal more conveniently. To stabilize the length of the resonator the PDH technique [Dre83] is used. To match the length to the frequency of the circulating light a vacuum compatible piezoelectric element [Noliac, NAC2125-H12-C01] is mounted between the spacer and the curved mirror, thus serving as an actuator.

A more precise view on the PMC is given in [Ali13], including characterizations of the mode scan and more information about the stabilization implementation.

4.2.2 Differences and Problems

The experimental realization of the power stabilization at the AEI 10 m Prototype requires several modifications compared to the preparation setup described in Chapter 3. All components that were different to the laboratory and therefore unknown had to be characterized to set up a well-performing experiment. At the AEI 10 m Prototype, the new components are the laser system consisting of an NPRO, another AOM, the amplification stage in combination with the 4.5 m long PCF and the PMC. In the experiment in the laboratory, a fiber-coupled laser was used as a laser source. Following are several issues that were faced when implementing the experiment in the AEI 10 m Prototype.

4.2.2.1 Acousto-Optic Modulator

First, the AOM had to be realigned due to its bad diffraction efficiency of about 2 % at most. The modulation range was too small to stabilize the power of the laser system due to too high noise peaks in the time domain. After the new alignment of the component, the diffraction efficiency was about 15.5 % for an offset voltage of ± 1 V applied to the driver unit. A complete characterization of the diffraction efficiency can be found in Figure 4.5.
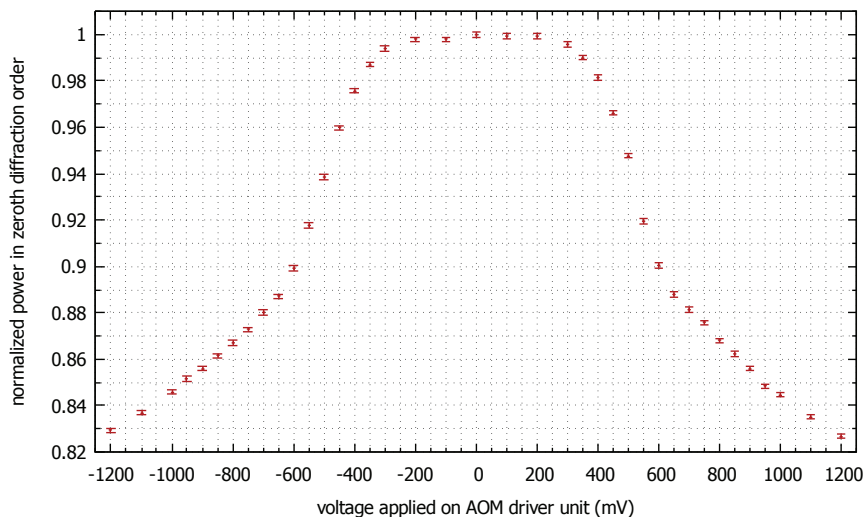
Figure 4.5: Diffraction efficiency measurement of the AOM. The power in the original beam with no applied voltage at the driver unit is about 23.1 W and the measurement is normalized by this value here. The desired offset voltage during the power stabilization experiment is about ± 500 mV so that ± 4 % of the power can be modulated on a linear slope.

The measurement was done by feeding different voltages into the driver unit and noticing the power measured by a thermal photodetector outside the tank. The sensor detected a power of about 23.1 W in the zeroth diffraction order with no applied voltage on the driver unit. The measurement accuracy is limited by a fixed error of ± 5 mW and an estimated time varying power dependent error of ± 20 mW for maximal power. The diffracted power is not entirely located in the first or negative first diffraction order, a small content can be diffracted in higher orders, too. Since the quality factor Q for the AOM is about $Q = 45$ and so $Q > 1$, the interaction regime is the Bragg regime [Nit08].

The measurement in Figure 4.5 illustrates an almost symmetric behavior for the diffracted light in the first and in the negative first diffraction order. The graph has two linear slopes that are within interesting ranges for the power stabilization experiment: On the one hand for driver unit voltages where $|U| > 700$ mV, and on the other hand for voltages where 600 mV $< |U| < 400$ mV. The desired region for the experiment is the second one with voltages around ± 500 mV. In the beginning, the slope is much higher than in the other region, corresponding to a greater total range of diffraction power of approximately ± 4 %. Secondly, the power that is lost in the beam dump is lower. When working with an offset value of ± 500 mV and sitting on the middle of the slope, only about 6 % of the original power is permanently diffracted. This voltage will be the desired one for the offset value that is summed to the signal, and is produced with the CDS. The bandwidth of the AOM is about 300 kHz as well as for the modulator that is used in Chapter 3.

4.2.2.2 Laser Source

A basic characterization of the whole optical signal path can be executed by measuring a transfer function from the AOM to the DC-readout channel of one photodiode of the photodiode array. This allows considering the whole new signal path of interest. This measurement is shown in Figure 4.6, and was done with a swept sine signal in the frequency range from 100 mHz to 100 kHz with a DC value of 500 mV, which is the desired offset value for the AOM. The signal was applied to the driver unit and had an amplitude of 50 mV.

The measurement differs fundamentally from the transfer function which was executed in the experiment in the laboratory in Chapter 3. In the preparation setup, this transfer function over the optical signal path behaves flat up to at least 100 kHz. Now the order of magnitude starts at 15 dB at 100 mHz and then smoothly drops down to 13 dB at 2 Hz. Above 2 Hz the graph stays flat up to a frequency of 400 Hz and rises over one decade to 25 dB, where it remains constant again. The phase stays zero for frequencies up to 100 Hz and increases up to 4 kHz, where it has a maximum of 37°. Then it drops down and has a zero point at 35 kHz, finally ending at -25° at 100 kHz. The phase loss is about 25° at 100 kHz.

The different behavior in the transfer function of the optical signal path is assumed to originate from the amplification stage of the laser system (see Sec. 4.1.1). This was considered by measuring a transfer function from the driver unit to a photodiode that was placed outside the vacuum tank behind the 35 W laser system. This measurement is equivalent to the one shown in Figure 4.6. Furthermore, the transfer function of the AOM was only detected by putting a photodiode directly behind this component. This graph
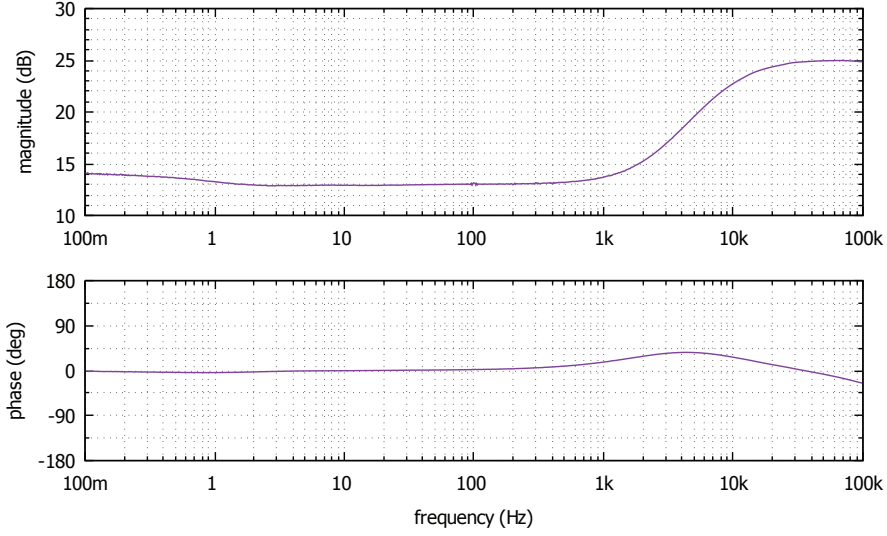
Figure 4.6: Transfer function from the AOM driver unit to the DC-readout signal of one photodiode in the photodiode array at the AEI 10 m Prototype. The magnitude increases by more than 10 dB from several hundred hertz over one decade, which is a fundamental different behavior than when measured with the NPRO in Chapter 3.

looks very similar to the frequency response that was measured for the other AOM used in the preparation experiment and was flat up to at least 100 kHz, in accordance with its expected bandwidth of roughly 300 kHz.

A high-pass behavior of an amplification stage was already observed at semiconductor optical amplifiers (SOAs) in publications like [Bou05; Yu99] before. There, this effect was measured at higher frequencies at around 1 GHz.

In principle, if the amplification stage is not saturated this effect would not occur because the input power would not be high enough to reduce the inversion level sufficiently by a constant pump power. The output power is linearly proportional to the input power, and the transfer function would look flat overall. An amplitude modulation of the input power would be increased by the gain G of the optical amplifier. However, numerous optical amplifiers are working in a saturated region since there the efficiency from pump power into output power is the highest. The population in the upper state is permanently reduced, and even more input power would increase the output power only marginally. Now the connection between input and output power does not change linearly anymore. Due to the smaller slope an amplitude modulation of the input power at lower frequencies would cause an output power oscillation amplified by a factor smaller than G. In Figure 4.6 one can find this factor to be approximately 13 dB. At higher frequencies, where the frequency response becomes flat again, the amplitude oscillation is probably too fast to stimulate all electrons during one maximum of oscillation. For these frequencies, the optical amplifier is not saturated and reinforces the amplitude modulation approximately by the gain G. At the AEI 10 m Prototype, this region has a level of about 25 dB, which equals a factor of approximately 17.8. This agrees well with the nominal output power of the NPRO with

2 W compared to the output power of the whole system of 35 W, differing by a factor of
17.5. This phenomenon was already characterized with the aid of a detailed simulation in
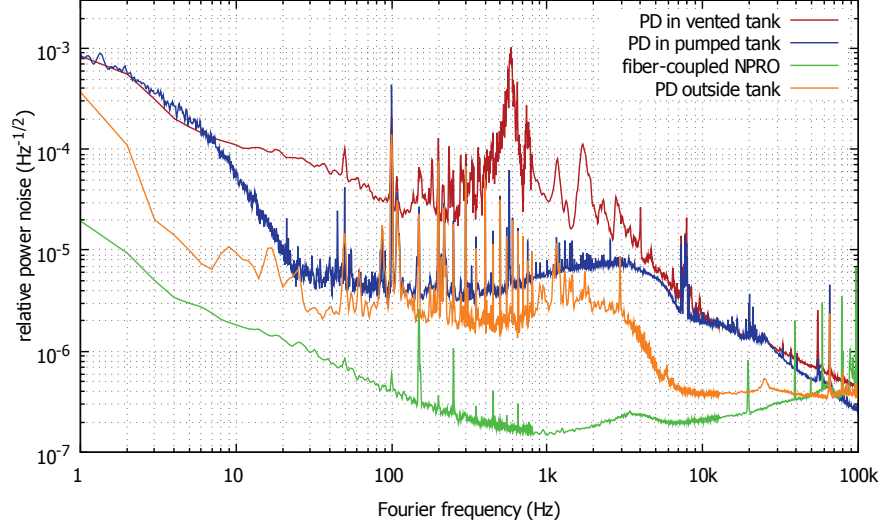the dissertation [Tün13] on fiber amplifiers.

Figure 4.7: Comparison of different RPN measurements. Drawn are the curves for the
fiber-coupled NPRO laser from the laboratory, for a photodiode standing outside the vacuum
tank and for a photodiode of the photodiode array in air as well as in vacuum.

Further essential considerations are to investigate firstly the power noise of the light directly
behind the laser system, and secondly measuring it with the photodiode array in the tank.
It is interesting to see if the optical components like the PCF or the PMC would change
this level further. A comparison of a measurement in air and in vacuum can be meaningful,
too. All these different RPN measurements can be found in Figure 4.7. The green graph of
the fiber-coupled NPRO laser was already drawn in Section 3.1.1, and has the best RPN of
all measurements. A photodiode placed outside the tank detected an RPN corresponding
to the orange curve. This graph continues almost flat from 30 Hz over two decades at a
level of approximately $(3 \pm 1.5) \times 10^{-6} \, \mathrm{Hz}^{-1/2}$, then falls down rapidly by one order of
magnitude and is nearly constant again from 800 Hz. Between 10 Hz and 10 kHz this graph
lies roughly one order of magnitude below the RPN measured with a photodiode of the
photodiode array drawn by the red graph. Remarkably this graph has a 130 Hz $\pm$ 20 Hz
broad high noise peak around 580 Hz $\pm$ 10 Hz. Higher order peaks of this frequency can be
found at 1160 Hz $\pm$ 20 Hz and 1740 Hz $\pm$ 30 Hz, too. These noise artifacts originate from
the air ventilator that is attached to the wall of the west tank of the AEI 10 m Prototype,
and disappeared after powering off this device. The most interesting measurement for this
experiment is given by the blue line, which shows the RPN of the tank in vacuum after
two days of pumping, when the air pressure was approximately $(1 \pm 0.1) \times 10^{-6} \, \mathrm{mbar}$. The
goal of this thesis is to stabilize this RPN to a value of $2 \times 10^{-9} \, \mathrm{Hz}^{-1/2}$ at 200 Hz, and to
be shot noise limited there. In comparison to the graph of the fiber-coupled NPRO, the

RPN of the laser source at the AEI 10 m Prototype is about ten times worse at frequencies of 100 Hz and 10 kHz. Between these frequencies the difference increases with a factor of 40 around 1 kHz. For frequencies from 1 Hz to 10 Hz, the RPN of the fiber-coupled NPRO laser is up to 80 times smaller. For the two measurements that are executed in the tank, a noise peak at approximately 7.8 kHz $\pm$ 100 Hz with a full width at half maximum (FWHM) of 400 Hz $\pm$ 100 Hz is notable. It has a constant height of approximately 2×10^{-5} Hz$^{-1/2}$ and could be reproduced by independent measurements at different times. This peak was already detected in the master thesis from T. Alig during an RPN measurement in transmission of the PMC [Ali13]. In general, he measured an RPN that was increased up to a factor of approximately 5; disregarding the broad air vent peak and compared to the blue curve in Figure 4.7 in the vented tank.

In comparison to an NPRO laser the additional RPN, which is imprinted on the light by the amplification stage, originates from the noise of the power supply. This is an ordinary behavior for amplification stages. For all measurements that are taken in the environment of the AEI 10 m Prototype, the spectrum contains numerous narrow peaks at multiples of the supply frequency of 50 Hz. In comparison to the out-of-loop relative power spectrum that was presented in Figure 3.15 in Section 3.3, the size of those peaks is highly amplified. The origin is assumed to be several ground loops that exist at the AEI 10 m Prototype originating from different electronics. Probably this problem can be reduced as well as in the preparation experiment in Chapter 3, by supplying all electrical components with low noise battery packs.

According to these measurements the RPN measured in the pumped tank has to be reduced by at least three orders of magnitude to reach the 10^{-9} Hz$^{-1/2}$ region at 200 Hz.

4.2.3 Electrical Modifications

The two main differences when comparing the preparation experiment in the laboratory to the one in the AEI 10 m Prototype are firstly the amplification stage of the laser system, and secondly the at least ten times larger RPN on the detector in the frequency band of interest. According to these differences, the electrical signal path has to compensate these problems. The main problem in the vacuum environment is an additional phase loss of at least 10 ° around frequencies of 100 kHz letting the control loop become instable, with the same electrical configuration as in the preparation experiment. This could be solved by decreasing the gain and reducing the unity gain frequency to 40 kHz, so that the phase loss is larger than 180 °. The problem with this configuration is the lost open loop gain over all frequencies of at least a factor of 10, resulting in a power stabilization experiment that is not shot noise limited at all due to insufficient gain.

However, the problems could be easily solved by modifying the feedback control loop. Now integrator 1, which is connected directly in front of the variable gain stage, is used with a cutoff frequency of 2.5 kHz (see again Fig. 3.9). This design has the advantage that the phase loss at the desired unity gain frequency region above 100 kHz is only approximately 5 °. In integrator 2 some resistors are changed, too, resulting in a cutoff frequency of 10 kHz and a phase loss of approximately 60 °. Together both components produce a phase loss of about 65 ° at 100 kHz and generate a gain of 44 dB at 200 Hz. In connection with the band-pass filter described in Section 3.1.3.1, the gain will be about 78 dB at 200 Hz

fulfilling the requirements of at least three orders of magnitude of noise suppression. The high-pass behavior of the amplification stage can be compensated in this way.

After these modifications, the whole feedback control filter can be characterized with a transfer function. Figure 4.8 shows this measurement and also draws simulated graphs that are done with LISO again; one for deactivated and one for activated integrators.
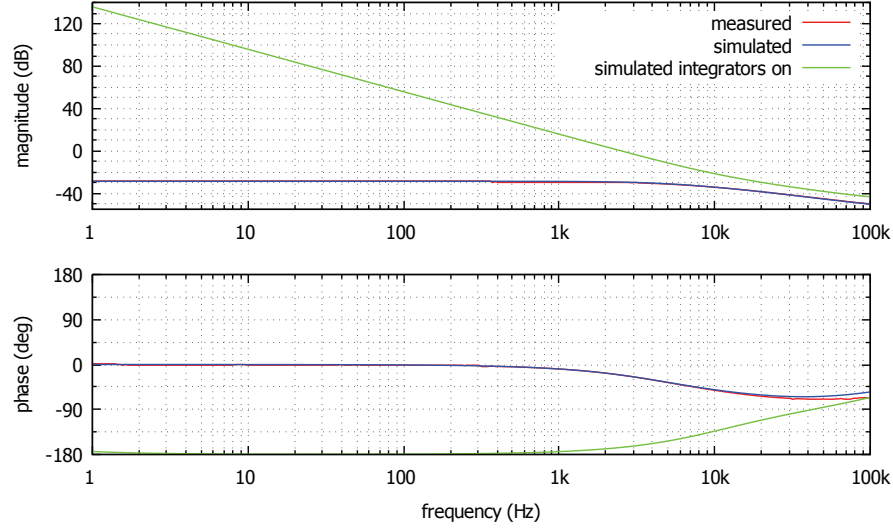

Figure 4.8: Measured and simulated transfer functions of the redesigned feedback control filter. Without integrator 2, the two graphs drawn as the red and the blue line are matching well. When activating the integrator 2 the simulation predicts the green graph. Due to the two integrators the phase of this graph lies at $-180°$ up to about 1 kHz.

The simulation including both integrators nicely depicts the already mentioned phase loss of $65°$ at 100 kHz. The blue and the red curve are almost perfectly on top of each other except for a small part at higher frequencies of the phase behavior where the measured graph lies up to $10°$ below the simulation. This can be explained by a low-pass behavior at such high frequencies originating from other components containing OP27 operational amplifiers, which are starting to produce small phase losses at 100 kHz. For instance, these components are built in the summation point or connected on the servo board for the inverter.

4.3   Characterizations and Achieved Performance

After characterizing every new component as well as possible and modifying the feedback control loop, the power stabilization experiment could be set up in the vacuum tank of the AEI 10 m Prototype. The air pressure was about $(1 \pm 0.1) \times 10^{-6}$ mbar during the time of observation. Again, the first important measurement is an open loop transfer function of the whole control loop that can be found in Figure 4.9 in the blue graph, when both integrators are activated. The magnitude is slightly fluctuating, but up to ten times greater than the red graph for frequencies smaller than 1 kHz. The red curve represents the open loop transfer function measured in connection with Section 3.3. For frequencies higher than

1 kHz both measurements are fitting well, which means that now the unity gain frequency of the power stabilization has a similar dimension as before with $140\,\text{kHz} \pm 10\,\text{kHz}$. The phase of both graphs is almost equal in the region below $100\,\text{kHz}$. The blue curve shows that the phase is smaller than $-180\,°$ for frequencies smaller than $33\,\text{kHz}$ due to the usage of two integrators that are consuming a lot of phase at low frequencies in addition with the band-pass filter behind the TIA. The phase achieves values greater than $-180\,°$ again in the frequency region of the first slope of the band-pass filter approximately between $1\,\text{mHz}$ and $100\,\text{Hz}$, however, this is not very relevant for the stabilization experiment.
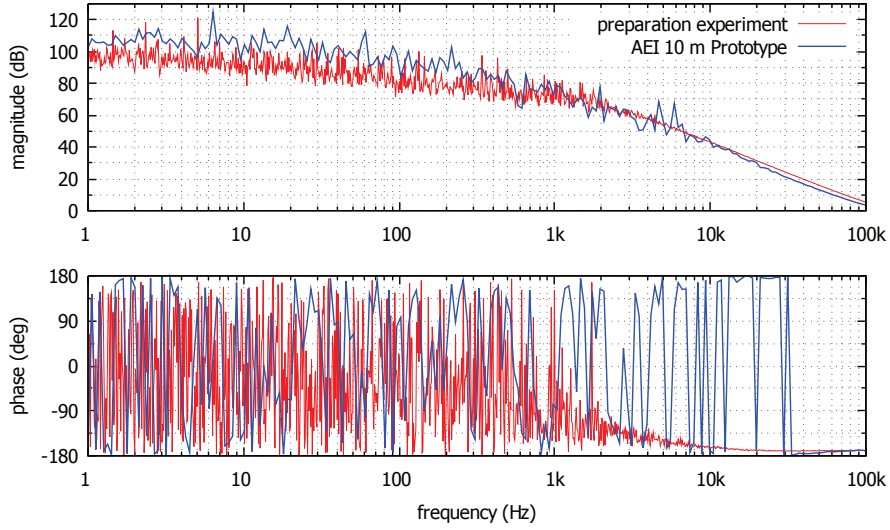
Figure 4.9: Measurement of the open loop transfer function during a stabilization performance at the AEI 10 m Prototype. For comparison the magnitude graph for the preparation experiment in the laboratory with the old electronics is drawn again.

The open loop gain curve shows that around $200\,\text{Hz}$ the gain is $90\,\text{dB} \pm 4\,\text{dB}$ fulfilling the noise suppression requirements of at least three orders of magnitude referred to in Section 4.2.2.2. So a relative shot noise level of about $2 \times 10^{-9}\,\text{Hz}^{-1/2}$ will not be limited by having not enough gain.

Again, all eight voltages are measured with the DC-readout channel of the TIA and are summarized in Table 4.1. Furthermore, the corresponding powers on each photodiode assuming a quantum efficiency of $\eta = 0.92$ are written down. The average power is about $40.8\,\text{mW}$ measured with the top stage and $36.6\,\text{mW}$ detected with the bottom stage resulting in a total average of $38.7\,\text{mW}$ for the whole photodiode array. The measurement uncertainties for the values are estimated to be $\pm 0.1\,\text{mW}$ with no running control loop. When it is activated, the fluctuations are dominated by range drifts in the diffraction of the AOM and thus increasing this error slightly. So the total power for the top stage is $163.0\,\text{mW} \pm 1\,\text{mW}$, and for the bottom stage it is $146.2\,\text{mW} \pm 1\,\text{mW}$. The corresponding photocurrent is $128.8\,\text{mA} \pm 1\,\text{mA}$ for the top stage and is $115.5\,\text{mA} \pm 1\,\text{mA}$ for the bottom stage. The power that is measured directly in front of the entrance of the photodiode

Table 4.1: Summary of the DC values of the eight photodiodes during the experiment at the AEI 10 m Prototype. The third row gives the relative changes of power from the experiment in the laboratory to the rebuild in the vacuum tank.

top	PD 1	PD 2	PD 3	PD 4	sum	mean
voltage [V]	-8.00	-7.40	-8.00	-8.79	-32.19	-8.05
power [mW]	40.5	37.5	40.5	44.5	163.0	40.8
relative shift [%]	-2.6	-2.0	2.4	0.2		

bot	PD 1	PD 2	PD 3	PD 4	sum	mean
voltage [V]	-7.00	-6.81	-7.26	-7.80	-28.87	-7.22
power [mW]	35.4	34.5	36.8	39.5	146.2	36.6
relative shift [%]	-4.1	1.5	1.3	3.1		

array is approximately $320\,\text{mW} \pm 2\,\text{mW}$, so about $97\,\%$ of the entering power is detected by the in-loop and the out-of-loop sensors. The rest of the power is mainly lost due to stray light on the aluminum cases of the photodiodes (approximately $2\,\%$); however some of the power is either detected by the two quadrant photodiodes ($\approx 3\,\text{mW} \,\widehat{=}\, 1\,\%$) or is lost due to internal losses of the optical components. By comparing the powers detected on the photodiodes to those recorded in Table 3.1 during the experiment in the laboratory, a power independent transformation matrix was calculated. This shows how the ratios between the individual powers have changed after the relocation of the photodiode array into the vacuum tank of the AEI 10 m Prototype. The values are written down in the third row of the table.

During the power stabilization experiment, the top stage and the bottom stage are used as the in-loop sensor, respectively. To characterize the achieved performance, the other stage was taken as the out-of-loop sensor. These two measurements are shown in Figure 4.10 and in Figure 4.11.

Both figures show the detected noise, with the sum of the top stage with the photodiodes as the blue curve and the sum of the bottom stage of the photodiodes as the light green curve. The achieved performances detected on the out-of-loop sensor are very similar in both measurements. There the RPN approaches the constant expected relative shot noise line that is $2.29 \times 10^{-9}\,\text{Hz}^{-1/2}$ in a frequency band from $200\,\text{Hz}$ to nearly $1\,\text{kHz}$. Due to the fact that for these frequencies the relative shot noise lies at about $1.1\,\text{dB}$ below the measurement, it is assumed that it is only limited by the shot noise of the photocurrent. There the detected sensitivity has a value of $(2.6 \pm 0.1) \times 10^{-9}\,\text{Hz}^{-1/2}$. According to theory and Equation 2.60, the quantum noise that is measured by the in-loop detector is imprinted on the laser beam by the control loop. However, at $800\,\text{Hz}$ the out-of-loop noise in Figure 4.10 slightly deviates itself from the relative shot noise level while in Figure 4.11 the out-of-loop graph is still just above the constant relative shot noise line until at least $1\,\text{kHz}$. It can be seen that the best result can be achieved when the bottom sum is taken as in-loop sensor.

However, the RPN could be reduced by a factor of approximately 1400, more than three
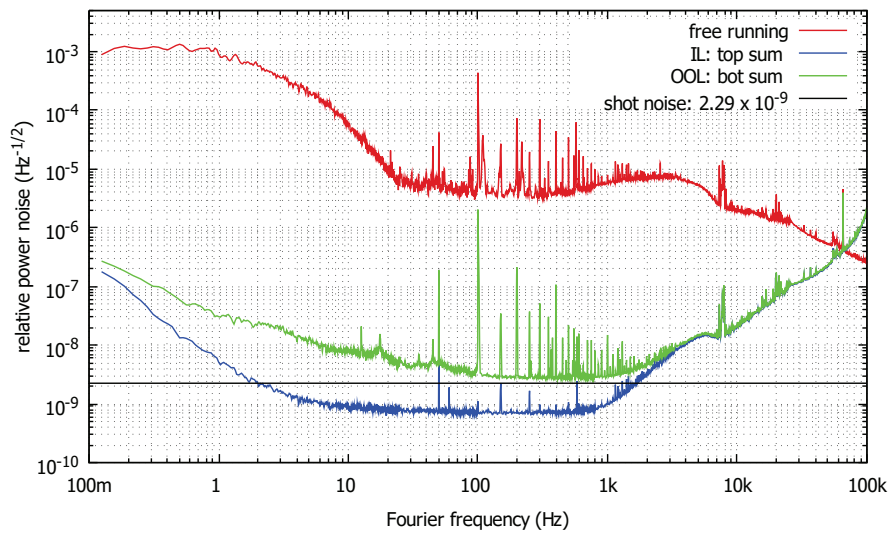
Figure 4.10: RPN for different measurements during the stabilization performance at the AEI 10 m Prototype. The in-loop curve is formed by the sum of the top stage and the out-of-loop graph is given by the sum of the bottom stage. Furthermore, the expected relative shot noise calculated with Equation 2.60 lies at $2.29 \times 10^{-9}\,\mathrm{Hz}^{-1/2}$ and is plotted as well as the free-running laser noise for comparison.

orders of magnitude, at a frequency of 200 Hz. For lower frequencies than 100 Hz, the RPN detected on the out-of-loop sensor goes up smoothly by approximately a factor of 5 per decade. This results in RPN values of $(3.1 \pm 0.2) \times 10^{-8}\,\mathrm{Hz}^{-1/2}$ 1 Hz and $(7.8 \pm 0.4) \times 10^{-9}\,\mathrm{Hz}^{-1/2}$ at 10 Hz.
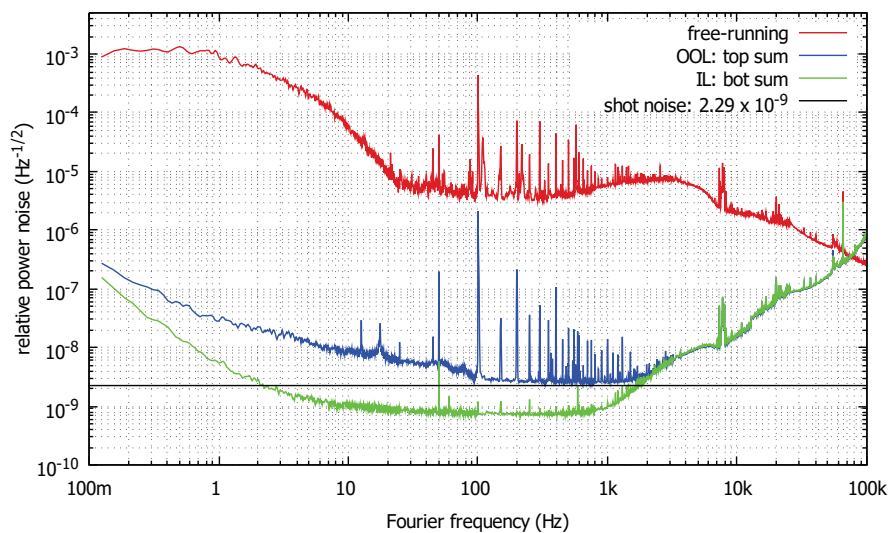
Figure 4.11: Similar diagram as in Figure 4.10, but here the sum of the bottom stage is used as the in-loop sensor.

The in-loop measurement drops to an RPN of $(7 \pm 0.5) \times 10^{-10}\,\mathrm{Hz}^{-1/2}$ and is flat there, probably originating from an electrical limitation. A similar level was achieved in Section 3.3 for the in-loop measurement. It is remarkable that several artifacts of the free-running noise, like the supply frequency peaks, the peak at about 8 kHz as well as the region around 20 kHz and the sharp oscillation at 65 kHz, remain on the light in the out-of-loop graph and partially in the in-loop measurement, too. Interestingly, only the even supply frequency peaks that are very dominant in the out-of-loop measurement are suppressed on the in-loop sensor.

Furthermore noticeable is that at roughly 70 kHz the free-running noise graph and the in-loop and out-of-loop curves are intersecting, and for greater frequencies the stabilized curves contain a higher RPN shown as the free-running graph. This effect can be explained by the servo bump that will be discussed in the following Section 4.3.1.

This comparison shows that the stages work almost in the same way, and that the achieved sensitivity does not change by substituting the in-loop and the out-of-loop sensor. This is in agreement with the expected relative shot noise calculable with Equation 2.60. The small difference in detected power on the two stages does not affect the performance level much. This means by detecting an equal amount of light on the top stage and bottom stage by the same detected total power of about 271.4 mW the relative shot noise would only be reduced by about 0.033 %.

The constant and stable physical conditions that are present in the vacuum tank allow a stable operation. So the power stabilization works with a long term stability of at least a few days. Therefore it is not an issue to have such small gain and phase margins and to work near instability. Even when the system becomes instable, the CDS has the opportunity of an auto-lock to discharge the integrators and to restart the control loop. On the other hand, when trying to run the system in the vented tank it is really prone to disturbances that are leading to instability when the integrators are activated.

4.3.1 Limitations

For the final conclusion, it is very important to also discuss several limitations as it was done in the end of Chapter 3. The desired limitation is the relative shot noise level of the light or the photocurrent respectively, that has a fundamental origin, so at all frequencies where this constant level is not approached, technical noise dominates the laser power stabilization.

The out-of-loop measurement, which was already characterized in Section 4.3, deviates increasingly from the constant relative shot noise level for frequencies lower than 100 Hz. Additional technical noise has to couple into some point of the signal path. In fact the in-loop graph in Figure 4.10 and in Figure 4.11 is still below the relative shot noise for frequencies greater than 2 Hz, so the increasing RPN in this frequency region does not originate from too little gain.

Figure 4.12 gives a precise overview of different types of noise that are present in the experiment. The out-of-loop RPN that was already drawn in Figure 4.11 is plotted by the black line. The green graph is a normalized measurement of the noise detected directly behind the band-pass filter when no current is injected in the TIA input. The measurement shown in the red graph was done at the reference point, and is normalized with a DC value
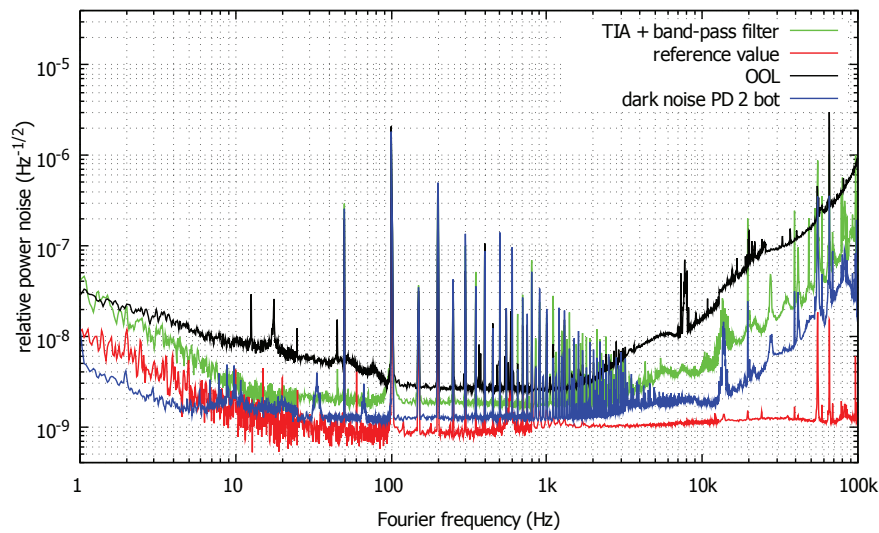
Figure 4.12: Comparison of the out-of-loop noise with the electrical noise measured behind the band-pass filter with no input current on the TIA (light green curve), and with the noise detected at the reference point (red graph) as well as to the dark noise of the worst photodiode. The electrical measurements are normalized by their desired DC value during the operation to compare them to the out-of-loop measurement in units of $\mathrm{Hz}^{-1/2}$.

of $7.5\,\mathrm{V}$. Both graphs lie below the out-of-noise measurement by at least a factor of 2, which means that electronic issues are assumed to be excluded to be the actual limiting noise source for frequencies smaller than $100\,\mathrm{Hz}$. Furthermore, in the graph the dark noise of the photodiode 2 at the bottom stage is depicted again. This measurement is already known from Figure 3.8 above. This photodiode was selected because it has the worst dark noise of all eight photodiodes. Now the graph is normalized with a DC voltage of $7.5\,\mathrm{V}$. From this it follows that the dark noise of the photodiodes is probably not relevant for the limitation of the power stabilization experiment in this low frequency region.

One limitation that can be responsible for spectral artifacts like the peaks at $12.6\,\mathrm{Hz}$ or the broader one at $17.5\,\mathrm{Hz}$ is assumed to be composed of stray light and beam pointing. The problem with stray light arising from beam clipping at the aluminum cases of the photodiode array could be reduced to a minimum, but it was not avoided entirely. The ratio of this effect can only be estimated, and was not investigated further.

Beam pointing couples into power fluctuations much more when the laser beams are not hitting the photodiodes on their most sensitive position. This was attempted to be adjusted as much as possible, but since there are no piezoelectric elements built in the beam path in the vacuum tank it is uncertain if the alignment of the eight single beams is perfect. So each small movement of the beam couples directly into power noise on the out-of-loop sensors. The absolute movement of the beam could be considered with the readout of the two quadrant photodiodes. A permanent pointing fluctuation of about $\pm 1\,\mathrm{\mu m}$ was detected. This value is also approximately valid for the beam movement on the eight individual photodiodes. This is comparable to the pointing fluctuations that could be detected during

the experiment in the laboratory before. Remarkably, there is a large constant tilt when comparing the beam position directly before and after the pump down process with an air pressure of 10^{-6} mbar. The measured beam displacement due to the pump process is about $50\,\mu\mathrm{m} \pm 10\,\mu\mathrm{m}$ located at the two quadrant photodiodes. Presumably, this occurs mainly because of large temperature differences during pumping by at least a few degrees Celsius. It was observed that the optical tables were deformed. Additionally, this tilt shifts the operation point on the sensitivity curve to a location where the slope is assumed to be even larger, and is thus increasing the coupling from pointing into power noise.

For frequencies greater than a few kilohertz, the in-loop and the out-of-loop measurements are very similar and finally overlap with the free-running laser noise. This is due to the servo bump that lies at the critical frequency ω_c of the control loop and has a value of $160\,\mathrm{kHz} \pm 10\,\mathrm{kHz}$, lying just above the unity gain frequency of $140\,\mathrm{kHz} \pm 10\,\mathrm{kHz}$. The gain margin here is only $5\,\mathrm{dB} \pm 2\,\mathrm{dB}$. It is a several tens kilohertz wide peak which stands out up to two orders of magnitude compared to the free-running laser noise. The peak does not mean that there is extra noise at these frequencies, but that at around ω_c the sensitivity to noise is enhanced [Wei11]. So the control loop impairs the RPN in this frequency region. A solution to reduce the effect of the servo bump at these frequencies is to slightly decrease the open loop gain and to increase the frequency gap between the unity gain frequency and the critical frequency. Then the gain margin will be increased, and this results in a suppressed servo bump. In the experiment, this can only be executed until a unity gain frequency of roughly $50\,\mathrm{kHz}$ is achieved. For smaller frequencies the control loop would become instable, which can be seen in Figure 4.9. Theoretically, another option is to increase the bandwidth of the control loop and shift the servo bump to higher and less relevant frequencies. Here, this is impossible due to the low-pass behavior of several components at frequencies larger than $100\,\mathrm{kHz}$, which are generating large phase losses. Furthermore, the effect of the servo bump at these frequencies does not constitute a problem at the AEI 10 m Prototype because the frequency band of interest is between $50\,\mathrm{Hz}$ and several hundred hertz.

The whole signal path can be subdivided into the electrical and the optical path. The optical distance between the actuator and the detector is approximately 10 m, and the electrical separation is about 5 m including the cable and the individual components. So the time a signal needs for the whole path assuming the speed of light is about 50 ns. From this it follows that the apparent long signal way does not affect the performance of the power stabilization experiment since the important frequencies are at most in the kilohertz region. The resulting phase loss caused by the long cables is negligible at these frequencies. When using long cables, other effects like the increase of capacitances is much more important.

Since the CDS is just an observation and reference tool for the power stabilization experiment the relatively slow sampling frequency of $65\,536\,\mathrm{Hz}$ that leads to a time accuracy of about $1\,\mu\mathrm{s}$, which then triggers the digital-to-analog converter and the analog-to-digital converter does not affect the speed of the control loop. Furthermore, no errors occur from digitizing the data.

4.3.2   Summary of the Power Stabilization Experiment for the AEI 10 m Prototype

In this chapter, the realization of the power stabilization experiment at the AEI 10 m Prototype was described and characterized. A general overview of the AEI 10 m Prototype was given including important subsystems like the 35 W laser system and the CDS. To adapt the preparation experiment to the conditions obtained at the environment of the AEI 10 m Prototype, the feedback control loop was modified. With these considerations, a laser power stabilization could be set up achieving an RPN that is shot noise limited in a frequency region between 200 Hz and at least 1 kHz. Within this range, the RPN is $(2.6\pm0.1)\times10^{-9}\,\mathrm{Hz}^{-1/2}$. The corresponding relative shot noise is to $(2.29\pm0.1)\times10^{-9}\,\mathrm{Hz}^{-1/2}$ and lies about 1.5 dB below the measurement. The power stabilization experiment runs with a long term stability of at least a few days when operating in the vacuum tank. A summary of the most important results of this chapter is given in Table 4.2.

Table 4.2: Summary of the most important results that characterize the laser power stabilization experiment at the AEI 10 m Prototype.

Parameter	Value
power on the il sensor	$146.2\,\mathrm{mW} \pm 1\,\mathrm{mW}$
power on the ool sensor	$163.0\,\mathrm{mW} \pm 1\,\mathrm{mW}$
corresponding relative shot noise	$2.29 \times 10^{-9}\,\mathrm{Hz}^{-1/2}$
RPN @200 Hz on the ool sensor	$(2.6 \pm 0.1) \times 10^{-9}\,\mathrm{Hz}^{-1/2}$
RPN @1 kHz on the ool sensor	$(2.6 \pm 0.1) \times 10^{-9}\,\mathrm{Hz}^{-1/2}$
unity gain frequency	$140\,\mathrm{kHz} \pm 0.10\,\mathrm{kHz}$

The experimental results could be achieved in a vacuum with an air pressure of about 10^{-6} mbar. For better comparison to other results, the RPN at 10 Hz and at 100 Hz is of interest. At 10 Hz a sensitivity of $(7.8\pm0.4)\times10^{-9}\,\mathrm{Hz}^{-1/2}$ could be achieved and at 100 Hz this value was $(3.1 \pm 0.1) \times 10^{-9}\,\mathrm{Hz}^{-1/2}$. To reach this low level of RPN, about several hundred milliwatt have to be detected, otherwise shot noise limits the sensitivity (compare Eq. 2.56 and Eq. 2.60). There exist not many experiments that are stabilizing a laser's amplitude to the 10^{-9} stability region. To the author's knowledge, the best RPN that was ever presented at these frequencies was from P. Kwee who reached $2.4 \times 10^{-9}\,\mathrm{Hz}^{-1/2}$ at 10 Hz and $1.8 \times 10^{-9}\,\mathrm{Hz}^{-1/2}$ at 100 Hz [Kwe09b]. F. Seifert came close to this region of stabilization performance and generated an RPN that is $5 \times 10^{-9}\,\mathrm{Hz}^{-1/2}$ at 10 Hz and $3.5 \times 10^{-9}\,\mathrm{Hz}^{-1/2}$ at 100 Hz [Sei06].

Another technique called optical AC coupling can avoid the necessity of high detected light power, and can simultaneously achieve a low noise level of $10^{-10}\,\mathrm{Hz}^{-1/2}$. It can increase the sensitivity of a photodetector by using an optical resonator. However, the optical AC coupling that was introduced in publications like [Kwe09a; Kwe08] achieves these sensitivities only at high frequencies above several hundred kilohertz. In the publication [Kwe11b] an RPN of $7\times10^{-10}\,\mathrm{Hz}^{-1/2}$ could be achieved in a small frequency region between approximately 100 kHz and 400 kHz by P. Kwee, B. Willke and K. Danzmann. Actually,

the best sensitivity by far was reached by the same three physicists as they reached an RPN of about $1.1 \times 10^{-10}\,\mathrm{Hz}^{-1/2}$ at $27\,\mathrm{MHz}$ [Kwe11a].

CHAPTER 5

Conclusion and Outlook

During the course of this thesis, a laser power stabilization experiment was first developed in a separated laboratory environment and then implemented at the AEI 10 m Prototype. The experiment was set up in a vacuum tank that will contain a Michelson interferometer with an arm length of 10 m. One goal of the AEI 10 m Prototype is to reach the standard quantum limit of interferometry in a region around 200 Hz, for which the laser source has to be shot noise limited. The corresponding relative power noise should be reduced to a level of about $2 \times 10^{-9} \, \mathrm{Hz}^{-1/2}$.

The stabilization concept consists of a feedback control loop to reduce the power noise of an Enhanced LIGO laser that is a 35 W laser system based on a commercial 2 W Nd:YAG NPRO as a laser source, and an amplification stage. The whole system is placed outside the vacuum tank, as is the actuator which is an acousto-optic modulator. A photonic crystal fiber couples the light into the vacuum tank. Inside the tank, the sensor that is formed by a high-sensitivity photodiode array is placed behind a pre-mode cleaner. This complex sensor contains eight photodiodes and allows detection of up to several hundred milliwatt overall without experiencing temperature problems. Two quadrant photodiodes improve the observation of pointing of the laser beam.

The readout electronics of the photodiodes are placed outside the tank, consisting of low noise transimpedance amplifiers connected to band-pass filters that are amplifying frequencies in the band from 3 Hz to 2.5 kHz.

During the operation in vacuum with an air pressure of about 10^{-6} mbar $\pm 10^{-7}$ mbar, a relative power noise accounting to $(2.8 \pm 0.1) \times 10^{-9} \, \mathrm{Hz}^{-1/2}$ could be achieved for Fourier frequencies between 200 Hz and at least 1 kHz. For these frequencies, the power stabilization was only limited by shot noise which can be calculated to $(2.29 \pm 0.1) \times 10^{-9} \, \mathrm{Hz}^{-1/2}$, hence lying about 1.5 dB below the measurement. During the measurement, the power on the in-loop sensor, consisting of four photodiodes that are summed together, was about $P_{\mathrm{il}} = 143.1 \, \mathrm{mW} \pm 1 \, \mathrm{mW}$, and the power on the equally built out-of-loop sensor was approximately $P_{\mathrm{ool}} = 128.3 \, \mathrm{mW} \pm 1 \, \mathrm{mW}$. The corresponding photocurrents were about $I_{\mathrm{il}} = 128.8 \, \mathrm{mA} \pm 1 \, \mathrm{mA}$ and $I_{\mathrm{ool}} = 115.5 \, \mathrm{mA} \pm 1 \, \mathrm{mA}$. The unity gain frequency of the control loop was at about $140 \, \mathrm{kHz} \pm 10 \, \mathrm{kHz}$.

The outstanding feature of this experiment is that the original design used for the power

stabilization of the aLIGO laser system [Kwe12; Põl14] was altered. The original setup shows the stabilization consisting of a first feedback control loop, which operates with the signal coming from a pre-mode cleaner and is detected with one photodiode. It furthermore consists of a second feedback control loop that uses a photodiode array as a sensor, too. However, at the original setup this sensor is placed behind a 20 m long input mode cleaner. Both error signals are summed up and applied to an acousto-optic modulator to modify the power of the laser beam. There, the actuator is located behind the last amplification stage and receives a power of about 200 W.

In the short-term future, there are some considerations that could be addressed to improve the laser power stabilization or corresponding elements of this experiment. To reduce the relative power noise at frequencies around the shot noise limited frequency region between 200 Hz and 1 kHz, more light power has to be detected on the photodiodes. However, problems of uncorrelated temperature fluctuations at the individual photodiodes could arise, causing increased power fluctuations. Furthermore, since the wedge shaped beam splitter is slightly polarization dependent, the polarization of the beam going into the photodiode array could be modified to reach a 50:50 power splitting on the in-loop and out-of-loop sensor. Then the relative shot noise would decrease by a few percent.

Furthermore, the two deflecting mirrors could be equipped with vacuum compatible piezoelectric elements for an enhanced beam alignment. With this addition, firstly all eight photodiodes could be realigned by the procedure discussed in this thesis, and secondly the laser beam position could be controlled and corrected when the tank is pumped down. An automatic beam alignment with a control loop would be useful.

When the stabilization experiment has to reach stability for a long-time operation for the relative power noise region of about $3 \times 10^{-9} \, \mathrm{Hz}^{-1/2}$ in the vented tank, one would have to reduce the phase loss around the unity gain frequency by increasing the capacity of integrator 2.

In the long-term future the design of the photodiode array should be reconsidered in general. The modification that was proposed and executed in this thesis with the implementation of a second quadrant photodiode would be a great benefit for future experiments. This modification allows to completely read out the uncoupled beam parameters independently, and to observe the position of the beam more accurately. This should be considered, as very precise beam alignment conditions are essential to avoid couplings of beam pointing into power noise due to misalignments.

In the future, the design of the used photodiode array at LIGO will be reconsidered, due to the knowledge acquired in this thesis. At the moment, the design of the attachment of the photodiodes is not solved optimally. Scattered light is almost unpreventable with this configuration due to the cone-shaped aluminium extensions in addition to photodiodes mounted too deep in the housing. Therefore these housings will be modified in the new design to avoid these issues. In addition, a strain relief will be attached to the photodiode array because of the positive experiences with strain reliefs in this project. No problems involving mechanical strains occured when using this feature. Furthermore, a second quadrant photodiode will be implemented to the photodiode array to observe the pointing of the beam with much higher accuracy. Realizing these modifications will help to build up a power stabilization experiment with a photodiode array as sensor more easily.

Bibliography

[Abb16]   Abbott, B. P. et al.: 'Observation of Gravitational Waves from a Binary Black Hole Merger'. *Phys. Rev. Lett.* (6 Feb. 2016), vol. 116: p. 061102 (cit. on pp. 2, 47).

[Abb01]   Abbott, R. S. and P. J. King: 'Diode-pumped Nd:YAG laser intensity noise suppression using a current shunt'. *Review of Scientific Instruments* (2001), vol. 72(2): pp. 1346–1349 (cit. on p. 21).

[Abr92]   Abramovici, A., W. E. Althouse, R. W. P. Drever, Y. Gürsel, S. Kawamura, F. J. Raab, D. Shoemaker, L. Sievers, R. E. Spero, K. S. Thorne, R. E. Vogt, R. Weiss, S. E. Whitcomb, and M. E. Zucker: 'LIGO: The Laser Interferometer Gravitational-Wave Observatory'. *Science* (1992), vol. 256(5055): pp. 325–333 (cit. on p. 2).

[Abr12]   Abramovici, A. and J. Chapsky: *Feedback Control Systems - A Fast-Track Guide for Scientists and Engineers*. 1st edition. Berlin Heidelberg: Springer Science & Business Media, 2012 (cit. on pp. 17, 18, 20).

[Ace08]   Acernese, F. et al.: 'The Virgo 3 km interferometer for gravitational wave detection'. *Journal of Optics A: Pure and Applied Optics* (2008), vol. 10(6): p. 064009 (cit. on p. 2).

[Ali13]   Alig, T.: *Charakterisierung und Unterdrückung der Strahlgeometriefluktuationen des fasergekoppelten 35W Lasers für das AEI 10m Prototypinterferometer*. 2013 (cit. on pp. 55, 59).

[And01]   Ando, M. et al.: 'Stable Operation of a 300-m Laser Interferometer with Sufficient Sensitivity to Detect Gravitational-Wave Events within Our Galaxy'. *Phys. Rev. Lett.* (18 Apr. 2001), vol. 86: pp. 3950–3954 (cit. on p. 2).

[Ant11]   Antonucci, F. et al.: 'LISA Pathfinder: mission and status'. *Classical and Quantum Gravity* (2011), vol. 28(9): p. 094001 (cit. on p. 51).

[Bac04]   Bachor, H.-A.: *A Guide to Experiments in Quantum Optics*. 2nd edition. New York: Wiley, 2004 (cit. on p. 15).

[Bar05]   Barr, B. W., K. A. Strain, and C. J. Killow: 'Laser amplitude stabilization for advanced interferometric gravitational wave detectors'. *Classical and Quantum Gravity* (2005), vol. 22(20): p. 4279 (cit. on pp. 21, 22, 45).

[Bas14]   Bassan, M.: *Advanced Interferometers and the Search for Gravitational Waves - Lectures from the First VESF School on Advanced Detectors for Gravitational Waves.* 2014th ed. Berlin, Heidelberg: Springer, 2014 (cit. on pp. 16, 17).

[Ber99]   Bertolini, A., G. Cella, R. DeSalvo, and V. Sannibale: 'Seismic noise filters, vertical resonance frequency reduction with geometric anti-springs: a feasibility study'. *Nucl. Instrum. Methods Phys. Res., A* (1999), vol. 435(3): pp. 475–483 (cit. on p. 48).

[Bog13]   Bogan, C.: 'Stabilized High Power Lasers and Spatial Mode Conversion'. PhD thesis. Gottfried Wilhelm Leibniz Universität Hannover, 2013 (cit. on p. 45).

[Böh13]   Böhme, J. F.: *Stochastische Signale - Eine Einführung in Modelle, Systemtheorie und Statistik.* Berlin Heidelberg New York: Springer-Verlag, 2013 (cit. on p. 8).

[Bor09]   Bork, R.: *Advanced LIGO CDS Design Overview.* Tech. rep. LIGO Document Control Center, 2009 (cit. on pp. 51, 52).

[Bou05]   Boula-Picard, R., M. Alouini, J. Lopez, N. Vodjdani, and J. C. Simon: 'Impact of the gain saturation dynamics in semiconductor optical amplifiers on the characteristics of an analog optical link'. *Journal of Lightwave Technology* (Aug. 2005), vol. 23(8): pp. 2420–2426 (cit. on p. 57).

[Bre77]   Brewer, E. C.: *A Guide to the Scientific Knowledge of Things Familiar.* Jarrold and Sons, 1877 (cit. on p. 1).

[Cle12]   Cleva, F., J.-P. Coulon, A. Brillet, and L.-W. Wei: *Laser power stabilization with a single high-power photodiode.* Tech. rep. VIRGO, 2012 (cit. on p. 29).

[Cor06]   Corbitt, T., Y. Chen, F. Khalili, D. Ottaway, S. Vyatchanin, S. Whitcomb, and N. Mavalvala: 'Squeezed-state source using radiation-pressure-induced rigidity'. *Phys. Rev. A* (2 Feb. 2006), vol. 73: p. 023801 (cit. on p. 48).

[Dah12a]   Dahl, K., G. Heinzel, B. Willke, K. A. Strain, S. Goßler, and K. Danzmann: 'Suspension platform interferometer for the AEI 10 m prototype: concept, design and optical layout'. *Classical and Quantum Gravity* (2012), vol. 29(9): p. 095024 (cit. on p. 49).

[Dah12b]   Dahl, K. et al.: 'Status of the AEI 10 m prototype'. *Classical and Quantum Gravity* (2012), vol. 29(14): p. 145005 (cit. on p. 49).

[Deh09]   Dehne, M., F. Guzmán Cervantes, B. Sheard, G. Heinzel, and K. Danzmann: 'Laser interferometer for spaceborne mapping of the Earth's gravity field'. *Journal of Physics: Conference Series* (2009), vol. 154(1): p. 012023 (cit. on p. 49).

[Dem14]   Demtröder, W.: *Experimentalphysik 2 - Elektrizität und Optik.* 6th edition. Berlin Heidelberg New York: Springer-Verlag, 2014 (cit. on p. 6).

[Dre83]   Drever, R. W. P., J. L. Hall, F. V. Kowalski, J. Hough, G. M. Ford, A. J. Munley, and H. Ward: 'Laser phase and frequency stabilization using an optical resonator'. *Applied Physics B* (1983), vol. 31(2): pp. 97–105 (cit. on pp. 49, 55).

[Ein16]   Einstein, A.: 'Die Grundlage der allgemeinen Relativitätstheorie'. *Annalen der Physik* (1916), vol. 354(7): pp. 769–822 (cit. on p. 1).

[Ein05a]   Einstein, A.: 'Ist die Trägheit eines Körpers von seinem Energieinhalt abhängig?' *Annalen der Physik* (1905), vol. 323(13): pp. 639–643 (cit. on p. 1).

[Ein05b]   Einstein, A.: 'Zur Elektrodynamik bewegter Körper'. *Annalen der Physik* (1905), vol. 322(10): pp. 891–921 (cit. on p. 1).

[Ein17]   Einstein, A.: 'Zur Quantentheorie der Strahlung'. *Physikalische Zeitschrift* (1917), vol. 18: pp. 121+ (cit. on p. 2).

[Elm00]   Elmer, Perkin: *Large-Area InGaAs Photodiodes C30619, C30641, C30642, C30665.* 2000 (cit. on p. 30).

[Exp11]   Experimental Physics and Industrial Control System (EPICS): *http://www.aps.anl.gov/epics.* 2011 (cit. on p. 52).

[Fle15]   Flechtner, F., K.-H. Neumayer, C. Dahle, H. Dobslaw, E. Fagiolini, J.-C. Raimondo, and A. Güntner: 'What Can be Expected from the GRACE-FO Laser Ranging Interferometer for Earth Science Applications?' *Surveys in Geophysics* (2015), vol. 37(2): pp. 453–470 (cit. on p. 49).

[Fox06]   Fox, M.: *Quantum Optics : An Introduction - An Introduction.* New York, London: OUP Oxford, 2006 (cit. on p. 10).

[Fra04]   Franzen, A.: *Erzeugung von gequetschtem Licht für die Gravitationswellen-Astronomie.* 2004 (cit. on pp. 11, 12).

[Fre07]   Frede, M., B. Schulz, R. Wilhelm, P. Kwee, F. Seifert, B. Willke, and D. Kracht: 'Fundamental mode, single-frequency laser amplifier for gravitational wave detectors'. *Opt. Express* (Jan. 2007), vol. 15(2): pp. 459–465 (cit. on p. 51).

[Ger05]   Gerry, C. and P. Knight: *Introductory Quantum Optics.* Cambridge: Cambridge University Press, 2005 (cit. on pp. 10, 13, 14, 16).

[Ger62]   Gertsenshtein, M. E. and V. I. Postovoit. *Soviet Physics JETP* (1962), vol. 16: p. 433 (cit. on p. 2).

[Goo15]   Goodman, J. W.: *Statistical Optics.* 2nd Edition. Berlin Heidelberg: John Wiley & Sons Inc, 2015 (cit. on p. 8).

[Grä13]   Gräf, C.: *Optical Design and Numerical Modeling of the AEI 10 M Prototype Sub-SQL Interferometer.* Freuburg i.B., 2013 (cit. on pp. 16, 48, 49, 51).

[Haf08]   Haferkorn, H.: *Optik - Physikalisch-technische Grundlagen und Anwendungen.* New York: John Wiley & Sons, 2008 (cit. on p. 5).

[Hag04]   Hage, B.: *Quantentomographische Charakterisierung gequetschter Zustände.* 2004 (cit. on p. 12).

[Har94]   Harb, C. C., M. B. Gray, H. A. Bachor, R. Schilling, P. Rottengatter, I. Freitag, and H. Welling: 'Suppression of the intensity noise in a diode-pumped neodymium:YAG nonplanar ring laser'. *IEEE Journal of Quantum Electronics* (Dec. 1994), vol. 30(12): pp. 2907–2913 (cit. on p. 21).

[Har10] Harry, G. M. and the LIGO Scientific Collaboration: 'Advanced LIGO: the next generation of gravitational wave detectors'. *Classical and Quantum Gravity* (2010), vol. 27(8): p. 084006 (cit. on p. 47).

[Hei00] Heinzel, G.: *LISO - Program for Linear Simulation and Optimization of Analog Electronic Circuits.* 2000 (cit. on p. 34).

[Hei04] Heinzel, G., V. Wand, A. García, O. Jennrich, C. Braxmaier, D. Robertson, K. Middleton, D. Hoyland, A. Rüdiger, R. Schilling, U. Johann, and K. Danzmann: 'The LTP interferometer and phasemeter'. *Classical and Quantum Gravity* (2004), vol. 21(5): S581 (cit. on p. 51).

[Hig15] High Temp Metals: *High Temp Metals an ISO:9001 AS9100C AS9120 and LCS certified company.* http://www.hightempmetals.com/techdata/hitempSuperInvardata.php. 2015. (Visited on 04/21/2016) (cit. on p. 54).

[Iva09] Ivanov, E. N.: 'Wide-band suppression of laser intensity noise'. *IEEE Transactions on Ultrasonics, Ferroelectrics, and Frequency Control* (Jan. 2009), vol. 56(1): pp. 22–26 (cit. on p. 21).

[Kaw10] Kawazoe, F. et al.: 'Designs of the frequency reference cavity for the AEI 10 m Prototype interferometer'. *Journal of Physics: Conference Series* (2010), vol. 228(1): p. 012028 (cit. on p. 49).

[Kaw12] Kawazoe, F. et al.: 'The AEI 10 m Prototype Interferometer frequency control using the reference cavity and its angular control'. *Journal of Physics: Conference Series* (2012), vol. 363(1): p. 012012 (cit. on p. 49).

[Kim07] Kim, D. I., H.-G. Rhee, J.-B. Song, and Y.-W. Lee: 'Laser output power stabilization for direct laser writing system by using an acousto-optic modulator'. *Review of Scientific Instruments* (2007), vol. 78(10), 103110 (cit. on p. 21).

[Kop14] Kopeikin, S. M., A. F., T. Fukushima, P. Teyssandier, J. Müller, N. Wex, I. Ciufolini, and G. Petit: *Frontiers in Relativistic Celestial Mechanics - Applications and Experiments.* Berlin: De Gruyter, 2014 (cit. on p. 34).

[Kop28] Kopfermann, H. and R. Ladenburg: 'Experimental Proof of Negative Dispersion'. *Nature 122* (1928), vol.: pp. 438–439 (cit. on p. 2).

[Kwe05] Kwee, P.: *Charakterisierung von Lasersystemen für Gravitationswellendetektoren.* 2005 (cit. on pp. 40, 44).

[Kwe10] Kwee, P.: *Laser Characterization and Stabilization for Precision Interferometry.* 1st edition. Göttingen: Sierke, 2010 (cit. on pp. 11, 12, 20–22, 29, 30, 34).

[Kwe12] Kwee, P., C. Bogan, K. Danzmann, M. Frede, H. Kim, P. King, J. Pöld, O. Puncken, R. L. Savage, F. Seifert, P. Wessels, L. Winkelmann, and B. Willke: 'Stabilized high-power laser system for the gravitational wave detector advanced LIGO'. *Opt. Express* (May 2012), vol. 20(10): pp. 10617–10634 (cit. on pp. 3, 25, 70).

[Kwe11a]   Kwee, P., B. Willke, and K. Danzmann: 'Laser power noise detection at the quantum-noise limit of 32A photocurrent'. *Opt. Lett.* (Sept. 2011), vol. 36(18): pp. 3563–3565 (cit. on p. 68).

[Kwe09a]   Kwee, P., B. Willke, and K. Danzmann: 'Laser power stabilization using optical ac coupling and its quantum and technical limits'. *Appl. Opt.* (Oct. 2009), vol. 48(28): pp. 5423–5431 (cit. on p. 67).

[Kwe11b]   Kwee, P., B. Willke, and K. Danzmann: 'New concepts and results in laser power stabilization'. *Applied Physics B* (2011), vol. 102(3): pp. 515–522 (cit. on pp. 25, 67).

[Kwe08]   Kwee, P., B. Willke, and K. Danzmann: 'Optical ac coupling to overcome limitations in the detection of optical power fluctuations'. *Opt. Lett.* (July 2008), vol. 33(13): pp. 1509–1511 (cit. on p. 67).

[Kwe09b]   Kwee, P., B. Willke, and K. Danzmann: 'Shot-noise-limited laser power stabilization with a high-power photodiode array'. *Opt. Lett.* (Oct. 2009), vol. 34(19): pp. 2912–2914 (cit. on pp. 21, 22, 25, 29, 30, 67).

[Kwe03]   Kwee, Patrick and Sebastian Linden: *Fortgeschrittenen Praktikum II, Interferometrische Längenmessung.* 2003 (cit. on pp. 8, 9).

[Lam98]   Lam, P. K.: 'Applications of Quantum Electro-optic Control and Squeezed Light'. PhD thesis. Australian National University, 1998 (cit. on p. 11).

[Löf11]   Löffler-Mang, M.: *Optische Sensorik - Lasertechnik, Experimente, Light Barriers.* 1st edition. Berlin Heidelberg New York: Springer-Verlag, 2011 (cit. on p. 7).

[Lüc10]   Lück, H., C. Affeldt, J. Degallaix, A. Freise, H. Grote, M. Hewitson, S. Hild, J. Leong, M. Prijatelj, K. A. Strain, B. Willke, H. Wittel, and K. Danzmann: 'The upgrade of GEO 600'. *Journal of Physics: Conference Series* (2010), vol. 228(1): p. 012012 (cit. on p. 47).

[Mai60]   Maiman, T. H.: 'Stimulated Optical Radiation in Ruby'. *Nature* (Aug. 1960), vol. 187(4736): pp. 493–494 (cit. on p. 2).

[Mai87]   Maischberger, K., A. Ruediger, R. Schilling, L. Schnupp, W. Winkler, and G. Leuchs: 'Status of the Garching 30-meter prototype for a large gravitational wave detector'. *In *Guangzhou 1987, Proceedings, Experimental gravitational physics* 316-321.* 1987 (cit. on p. 2).

[Mat15]   Matsumoto, N.: *Classical Pendulum Feels Quantum Back-Action.* Berlin, Heidelberg: Springer, 2015 (cit. on p. 16).

[Mes08]   Meschede, D.: *Optik, Licht und Laser.* 3rd edition. Berlin Heidelberg New York: Springer-Verlag, 2008 (cit. on p. 7).

[Mic81]   Michelson, A. A.: 'The relative motion of the Earth and of the Luminiferous ether'. *American Journal of Science* (1881), vol. 22 (cit. on p. 1).

[Mic87]   Michelson, A. A. and E. W. Morley: 'On the Relative Motion of the Earth and the Luminiferous Ether'. *American Journal of Science* (1887), vol. 34: pp. 333–345 (cit. on p. 1).

[Mio07]   Mio, N., T. Ozeki, K. Machida, and S. Moriwaki: 'Laser Intensity Stabilization System Using Laser-Diode-Pumped Nd:YAG Rod-Laser Amplifier'. *Japanese Journal of Applied Physics* (2007), vol. 46(8R): p. 5338 (cit. on pp. 21, 22).

[Moe07]   Moeller, K. D.: *Optics - Learning by Computing, with Examples Using Maple, MathCad®, Matlab®, Mathematica®, and Maple®*. 2nd edition. Berlin Heidelberg: Springer Science & Business Media, 2007 (cit. on p. 6).

[Mos71]   Moss, G. E., L. R. Miller, and R. L. Forward: 'Photon-Noise-Limited Laser Transducer for Gravitational Antenna'. *Appl. Opt.* (Nov. 1971), vol. 10(11): pp. 2495–2498 (cit. on p. 2).

[Mus14]   Musha, M., T. Kanaya, K. Nakagawa, and K.-I. Ueda: 'Intensity and frequency noise characteristics of two coherently-added injection-locked Nd:YAG lasers'. *Applied Physics B* (2014), vol. 73(3): pp. 209–214 (cit. on p. 21).

[Nag98]   Nagano, S., M. Musha, L. Ying, and K.-I. Ueda: 'Investigation of an injection-locked Nd : YAG laser for the gravitational wave detection'. (1998), vol. (cit. on p. 21).

[Nag14]   Nagourney, W.: *Quantum Electronics for Atomic Physics and Telecommunication*. 2nd edition. New York, London: OUP Oxford, 2014 (cit. on p. 8).

[New87]   Newton, Sir I. and E. Halley: *Philosophiae naturalis principia mathematica*. Jussu Societatis Regiae ac typis Josephi Streater, prostant venales apud Sam. Smith, 1687 (cit. on p. 1).

[Nit08]   Nittmann, M.: *Neue Konzepte und Technologien für diodengepumpte, hochrepetierende Nanosekundenlaser im Wellenlängenbereich von 213 nm bis 4,6 µm*. 1st edition. Göttingen: Cuvillier Verlag, 2008 (cit. on p. 56).

[Noc04]   Nocera, F.: 'LIGO laser intensity noise suppression'. *Classical and Quantum Gravity* (2004), vol. 21(5): S481 (cit. on pp. 21, 45).

[Nol11]   Nolte, D. D.: *Optical Interferometry for Biology and Medicine*. edition 2012. Berlin Heidelberg: Springer Science & Business Media, 2011 (cit. on p. 9).

[Ott00]   Ottaway, D.J., P.J. Veitch, C. Hollitt, D. Mudge, M.W. Hamilton, and J. Munch: 'Frequency and intensity noise of an injection-locked Nd:YAG ring laser'. *Applied Physics B* (2000), vol. 71(2): pp. 163–168 (cit. on p. 21).

[Pea10]   Peatross, J. and M. Ware: 'Physics of Light and Optics: A Free Online Textbook'. *Frontiers in Optics 2010/Laser Science XXVI*. Optical Society of America, 2010: JWA64 (cit. on p. 13).

[Põl14]   Põld, J. H.: 'Design, Implementation and Characterization of the Advanced LIGO 200 W System'. PhD thesis. Leibniz Universität Hannover, 2014 (cit. on pp. 20, 29, 45, 70).

[Pun10]   Punturo, M. et al.: 'The Einstein Telescope: a third-generation gravitational wave observatory'. *Classical and Quantum Gravity* (2010), vol. 27(19): p. 194002 (cit. on pp. 3, 47).

[Res10]   Research, Wolfram: *Mathematica 8.0*. Champaign, Illinios, 2010 (cit. on p. 32).

[Rie08]   Riesen, R. and C. Brannon: *Standard Operating Procedure: Enhanced LIGO 35-W Nd:YAG Laser for the LLO Interferometer*. Tech. rep. LIGO Science Collaboration, 2008 (cit. on p. 50).

[Rog07]   Rogers, J.W.: *Adaptive Methods for the Helmholtz Equation with Discontinuous Coefficients at an Interface*. Baylor University, 2007 (cit. on p. 7).

[Rol04]   Rollins, J., D. Ottaway, M. Zucker, R. Weiss, and R. Abbott: 'Solid-state laser intensity stabilization at the 10-8 level'. *Opt. Lett.* (Aug. 2004), vol. 29(16): pp. 1876–1878 (cit. on pp. 21, 22, 45).

[Row94]   Rowan, S., A.M. Campbell, K. Skeldon, and J. Hough: 'Broadband Intensity Stabilization of a Diode-pumped Monolithic Miniature Nd: YAG Ring Laser'. *Journal of Modern Optics* (1994), vol. 41(6): pp. 1263–1269 (cit. on p. 21).

[Sak93]   Sakurai, J. J.: *Modern Quantum Mechanics (Revised Edition)*. Revised. Addison Wesley, Sept. 1993 (cit. on p. 14).

[Sat09]   Sathyaprakash, B.S. and B. F. Schutz: 'Physics, Astrophysics and Cosmology with Gravitational Waves'. *Living Reviews in Relativity* (2009), vol. 12(2) (cit. on p. 34).

[Sau94]   Saulson, P. R.: *Fundamentals of Interferometric Gravitational Wave Detectors*. Singapur: World Scientific, 1994 (cit. on pp. 12, 16).

[Sch05]   Schilling, R.: *OptoCad - A Fortran 95 module for tracing Gaussian beams through an optical set-up*. http://www.rzg.mpg.de/ ros/OptoCad/. 2005 (cit. on p. 30).

[Sei10]   Seifert, F.: 'Power Stabilization of High Power Lasers for Second Generation Gravitational Wave Detectors'. PhD thesis. Leibniz Universität Hannover, 2010 (cit. on pp. 9, 21, 22, 29, 36).

[Sei06]   Seifert, F., P. Kwee, M. Heurs, B. Willke, and K. Danzmann: 'Laser power stabilization for second-generation gravitational wave detectors'. *Opt. Lett.* (July 2006), vol. 31(13): pp. 2000–2002 (cit. on pp. 21, 22, 25, 29, 67).

[Shm07]   Shmaliy, Y.: *Continuous-Time Systems*. Berlin Heidelberg: Springer Science & Business Media, 2007 (cit. on p. 18).

[Sho88]   Shoemaker, D., R. Schilling, L. Schnupp, W. Winkler, K. Maischberger, and A. Rüdiger: 'Noise behavior of the Garching 30-meter prototype gravitational-wave detector'. *Phys. Rev. D* (2 July 1988), vol. 38: pp. 423–432 (cit. on p. 2).

[Tak08]   Takahashi, K., M. Ando, and K. Tsubono: 'Stabilization of laser intensity and frequency using optical fiber'. *Journal of Physics: Conference Series* (2008), vol. 122(1): p. 012016 (cit. on pp. 21, 22).

[Tak07]   Takamori, A. et al.: 'Inverted pendulum as low-frequency pre-isolation for advanced gravitational wave detectors'. *Nucl. Instrum. Meth.* (2007), vol. A582: pp. 683–692 (cit. on p. 48).

[Tay16]   Taylor, Michael A. and Warwick P. Bowen: 'Quantum metrology and its appli-
            cation in biology'. *Physics Reports* (2016), vol. 615. Quantum metrology and
            its application in biology: pp. 1–59 (cit. on p. 16).

[The15]   The LIGO Scientific Collaboration et al.: 'Advanced LIGO'. *Classical and
            Quantum Gravity* (2015), vol. 32(7): p. 074001 (cit. on p. 2).

[Tsu92]   Tsubono, K. and S. Moriwaki: 'Shot-Noise Limited Low-Frequency Intensity
            Noise of a Nd:YAG Laser'. *Japanese Journal of Applied Physics* (1992), vol.
            31(4R): p. 1241 (cit. on p. 21).

[Tün13]   Tünnermann, H.: 'Fiber Amplifiers for Gravitational Wave Detectors: Temporal
            Dynamics and Coherent Beam Combining'. PhD thesis. Gottfried Wilhelm
            Leibniz Universität Hannover, 2013 (cit. on p. 58).

[Ufi14]   Ufimtsev, P. Y.: *Fundamentals of the Physical Theory of Diffraction.* New York:
            John Wiley & Sons, 2014 (cit. on p. 5).

[Wan13]   Wanner, A.: 'Design, Seismic Attenuation System for the AEI 10m Prototype'.
            PhD thesis. Leibniz Universität Hannover, 2013 (cit. on p. 49).

[Wan12]   Wanner, A., G. Bergmann, A. Bertolini, T. Fricke, H. Lück, C. M. Mow-Lowry,
            K. A. Strain, S. Goßler, and K. Danzmann: 'Seismic attenuation system for the
            AEI 10 meter Prototype'. *Classical and Quantum Gravity* (2012), vol. 29(24):
            p. 245007 (cit. on p. 48).

[Wei15]   Wei, L.-W.: 'High-power laser system for Advanced Virgo gravitational wave
            detector : coherently combined master oscillator fiber power amplifers'. PhD
            thesis. Université Nice Sophia Antipolis, 2015 (cit. on p. 44).

[Wei11]   Weidemüller, M. and C. Zimmermann: *Interactions in Ultracold Gases - From
            Atoms to Molecules.* New York: John Wiley & Sons, 2011 (cit. on p. 66).

[Wes12]   Westphal, T. et al.: 'Design of the 10 m AEI prototype facility for interferometry
            studies'. *Applied Physics B* (2012), vol. 106(3): pp. 551–557 (cit. on p. 2).

[Wil15]   Willke, B.: *Laserstabilisierung und Kontrolle optischer Experimente.* Univer-
            sitätsvorlesung. 2015 (cit. on p. 19).

[Wil08]   Willke, B., K. Danzmann, M. Frede, P. King, D. Kracht, P. Kwee, O. Puncken,
            R. L. Savage Jr., B. Schulz, F. Seifert, C. Veltkamp, S. Wagner, P. Weßels, and
            L. Winkelmann: 'Stabilized lasers for advanced gravitational wave detectors'.
            Classical and Quantum Gravity (2008), vol. 25(11): p. 114040 (cit. on pp. 25,
            50).

[Wil02]   Willke, B. et al.: 'The GEO 600 gravitational wave detector'. *Classical and
            Quantum Gravity* (2002), vol. 19(7): p. 1377 (cit. on p. 2).

[Yan13]   Yaniv, O.: *Quantitative Feedback Design of Linear and Nonlinear Control
            Systems.* 1st edition. Berlin Heidelberg: Springer Science & Business Media,
            2013 (cit. on p. 18).

[Yu99]   Yu, H.-Y., D. Mahgerefteh, P. S. Cho, and J. Goldhar: 'Optimization of the
            Frequency Response of a Semiconductor Optical Amplifier Wavelength Con-
            verter Using a Fiber Bragg Grating'. *J. Lightwave Technol.* (Feb. 1999), vol.
            17(2): p. 308 (cit. on p. 57).

[Zaw02]   Zawischa, I., M. Brendel, K. Danzmann, C. Fallnich, M. Heurs, S. Nagano,
            V. Quetschke, H. Welling, and B. Willke: 'The GEO 600 laser system'. *Classical
            and Quantum Gravity* (2002), vol. 19(7): p. 1775 (cit. on p. 21).

List of Figures

List of Tables

Appendix

Figure A.1: Photograph of the self-made offset box. Furthermore, it was used for the first electronic readout for the first quadrant photodiode.
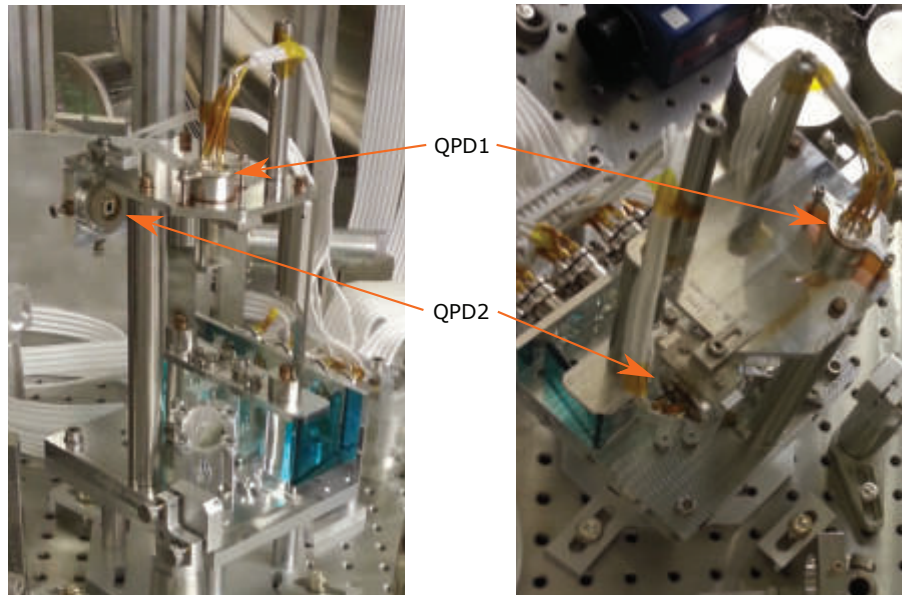
Figure A.2: Photograph of the modified photodiode array, which is placed in the tank of the AEI 10 m Prototype.

Figure A.3: Pin assignment for the D-Sub-37 cable connection photodiodes with the readout electronics.
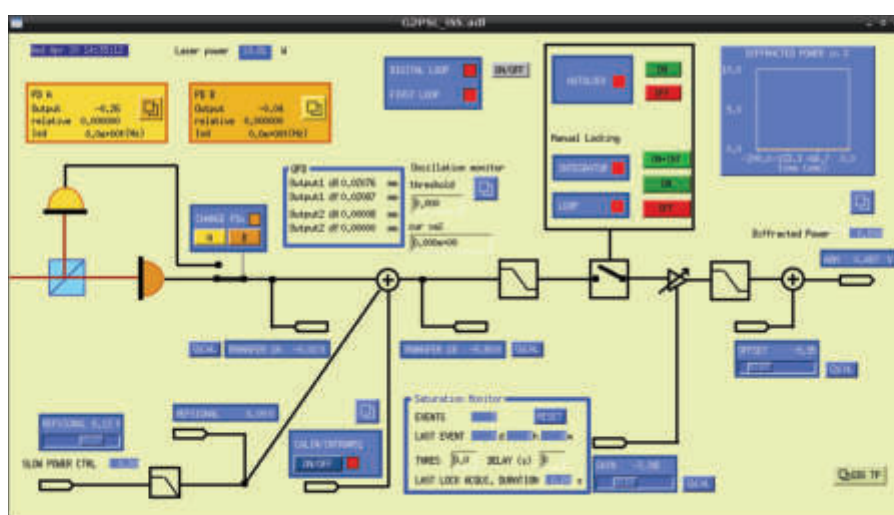
Figure A.4: Screenshot of the controlling of the power stabilization experiment with the control and data system.

Acknowledgments

At the end of my thesis I would like to thank all those people who made this thesis possible and an unforgettable experience for me.

First of all I would like to express my gratitude to Prof. Benno Willke and Prof. Karsten Danzmann who gave me the opportunity to work at the AEI and to write my master thesis here. Thanks for great research conditions that I could benefit from at the institute.
I am thankful for my advisor Patrick Oppermann who offered his continuous advice and was always available for me. He provided assistance when problems with the experiment occurred or whenever I had any questions.

Furthermore, I would like to thank all members of the institute in particular those of the laser group. Thanks for the friendly welcome and helpful cooperation. I had a good time with all of them. Additionally, it was an interesting experience to take part in the weekly group discussions and to gain insight into the work of my colleagues. A special thanks goes to Prof. Benno Willke who always had an open door for my questions and gave me further suggestions.

I am especially grateful to Patrick Oppermann, Justus Schmidt, Steffen Kaufer and Janis Wöhler for the proofreading of my thesis. Thanks for the corrections in language and for new ideas for the structure.

I enjoyed the years of my studies very much which is to a great extend because of my friends and companions. Thanks for the wonderful time and the help that I always got from them whenever I was in trouble.

Finally, I take this opportunity to express the profound gratitude to my beloved parents, for their boundless support not only emotionally but also materially. I acknowledge my gratitude to my girlfriend Lina who permanently supported and encouraged me. A special thanks goes to her patient support with the English language, which helped me a lot while writing this thesis.

Declaration

I hereby declare that this thesis is my own work and effort and that it has not been submitted anywhere for any award. Where other sources of information have been used, they have been acknowledged.

Hannover, May 10, 2016   Jonas Junker